Quantum non-Demolition Readout of Superconducting Artificial Atoms

Zur Erlangung des akademischen Grades einer
DOKTORIN DER NATURWISSENSCHAFTEN (Dr. rer. nat.)
von der KIT-Fakultät für Physik des
Karlsruher Instituts für Technologie (KIT)

genehmigte
Dissertation
von

M. Sc. Daria Gusenkova

Tag der mündlichen Prüfung:	05. November 2021
Referent:	Prof. Dr. Wolfgang Wernsdorfer
Korreferent:	Prof. Dr. David DiVincenzo
Korreferent:	Dr. Ioan M. Pop

Contents

1 Introduction

Quantum technologies are evolving from fundamental scientific concepts into industrial applications which have significant potential to affect our economy and society. They exploit the principles of quantum mechanics such as superposition, entanglement, and tunneling, to develop new generation of sensors [DRC17], communication networks [GT07; Lon+07], simulators [BN09; GAN14] and computers [DiV95; EJ96; NC10]. The quantum superposition principle states that the quantum object, unlike the classical one, can occupy two or more states simultaneously. Interaction between quantum objects leads to entanglement: states of the objects remain correlated even if they were spatially separated after interaction. Finally, quantum tunneling allows classically forbidden transitions: for example, a particle can pass through an energy barrier higher than its kinetic energy due to the wave nature of the particle.

Quantum sensors exploiting squeezed light and quantum non-demolition measurements can detect signals with ultimate precision, even beating the fundamental limits imposed by the uncertainty principle [GLM04; Her+10]. They can be used for medical imaging and non-invasive diagnosis, gravity measurements, navigation, and detecting defects in materials.

Quantum communication protocols are based on the entanglement between interacting quantum systems. The quantum correlations and impossibility to create identical copies of the quantum state allow secure storage and encryption of data. The quantum communication channels are immune to interception even by quantum devices.

Quantum simulators operate on the principle of quantum tunneling and are effective for some particular problems solved by optimization methods. Such simulators are application-specific: the system under examination has to be mapped on the Hamiltonian of the well-controlled simulator [AW12; HTK12; Tra12]. They can be used to design new materials with tailored properties and to simulate chemical reactions for medicine and energy applications.

The universal quantum computers which require control and manipulation of single quantum bits are the most challenging application of quantum technologies. Unlike classical bits, which can take only two values, 0 and 1, quantum bits (qubits) can be in a superposition of these states. It means that one qubit can store two values simultaneously, both $|0\rangle$ and $|1\rangle$. The number of stored values grows exponentially with number of qubits. Therefore, in theory quantum computers outperform classical ones, which have a linear scaling of the computational power with number of bits on the chip. Superposition and entanglement allow "parallel" computations: an operation on the quantum register gives result for all the initial states in the superposition simultaneously. However, these states can not be read out individually. During readout the system is projected into one of them.

There are several platforms for quantum electronics: superconducting circuits [DS13; Wen17], quantum dots [BEL00], trapped ions [HRB08], defects in diamond [Dut+07; Yao+12], and atoms in microwave resonators [RBH01a]. Superconducting circuits can have macroscopic dimensions, yet they operate in the quantum regime. Direct currents flow in superconductors without dissipation, and using superconducting devices is expected to tackle the problem of heating which currently limits the speed of conventional semiconductor processors. The circuits can be engineered to have specific energy spectrum and coupling to the control and readout microwave fields. Circuits with anharmonic energy spectrum play the role of artificial atoms and spins. Propagating microwave signals can entangle distant atoms enabling implementation of quantum communication protocols and distributed quantum computing. In addition, the superconducting circuit fabrication is compatible with existing industrial scale-up and integration techniques, which made them one of the most advanced platforms for quantum applications.

The quantum states are very fragile: interaction with the environment leads to leakage of information and destruction of entanglement. Quantum chips are shielded from the background electric and magnetic fields, and cooled down to millikelvin temperatures to reduce thermal excitations. Still, macroscopic superconducting circuits are particularly sensitive to environmental fields due to their large dipole moments. They easily couple to neighboring circuits and defects in the materials. Decoherence of superconducting atoms is still a major problem on the way to practical implementations. The existing prototypes of superconducting quan-

tum computers can not operate without error correction [Ofe+16]. Continuous error correction algorithms require repeated measurement of the single quantum object without destroying its state. Such measurements are called quantum non-demolition (QND).

The interaction of superconducting atoms with microwave fields is described with the circuit electrodynamics (cQED) theory [Bla+04; Wal+04; Bla+20]. The cQED theory suggests that QND measurements of superconducting artificial atoms can be realized with different types of interaction with the readout resonator: dispersive, longitudinal, and cross-Kerr. The dispersive interaction is perturbative and approximately QND. However, error correction algorithms require a certain threshold for the QND measurement fidelity [FSG09; Bar+14; Ter15]. In theory, the fidelity of the QND dispersive readout can be improved by increasing the readout power. In practice however increase of the readout power also leads to various non-QND processes, and superconducting atoms are usually operated at the single photon regime, with the interesting exception of Andreev qubits, which appear to be completely immune to the readout drive [Hay+20; Jan+15]. We constructed a superconducting atom which is resilient to readout power corresponding to hundred photons in the readout resonator, which allows state-of-the-art QND fidelity $\gtrsim 96.7\%$ and state discrimination time of $\tau = 175\,\mathrm{ns}$. In contrast to dispersive interaction, longitudinal and cross-Kerr interactions are truly QND, but their practical implementation is challenging (see Section 3 and [Das+20]).

This thesis is organized as follows: we start by giving a definition of the QND measurements, and provide basics of the superconducting quantum circuits. We also introduce the two superconducting artificial atoms: the transmon and fluxonium and discuss the fluxonium implementation. The second section is devoted to the dispersive readout in cQED, and its realization with the fluxonium atom. First, we present the high power QND dispersive readout of the fluxonium atom based on the results published in Ref. [Gus+21]. Secondly, we demonstrate implementation of the gradiometric fluxonium atom. In the third section we address the possible implementation of the longitudinal interaction between the transmon qubit and the resonator based on the nonlinear coupling scheme proposed in Ref. [**Richer2016longitudinal**]. We share unpublished results demonstrating the practical challenges of achieving the longitudinal regime. The fourth section contains a description of methods used for fabrication, simulation, and measurements of the superconducting circuits.

1.1 Quantum non-demolition measurements

Development of quantum non-demolition measurement techniques was motivated by a demand for high-precision detection of weak signals, such as gravitational waves. The first attempts to measure gravitational waves were made with macroscopic mechanical oscillators, multi-ton bars driven by propagating waves [Web68]. The experiments required repeated measurements of the oscillator displacement with accuracy of $\lesssim 10^{-19}$cm [BVT80]. The accuracy of repeated measurements on a single quantum system is, in general, limited by the Heisenberg's uncertainty principle. Precise projective measurement of the observable collapses the system eigenfunction into one of the observable's eigenstates [HR06]. The immediate subsequent measurement should give the same result precisely. However, due to the uncertainty principle, the measurement disturbs any non-commuting observables in a completely unpredictable way. The delocalization of the non-commuting observable can be fed back into the measured one by a free evolution of the system. This feedback, called measurement back action, affects precision of subsequent measurements of the observable.

Only a special class of measurements, called quantum non-demolition (QND), allow circumventing the effect of the uncertainty principle. The QND measurement should fulfill several criteria, established by Caves *et al.* in 1980 [Cav+80; HR06]. The system coupled to the measuring apparatus is described by the Hamiltonian $\hat{H} = \hat{H}_\mathrm{s}+\hat{H}_\mathrm{m}+\hat{H}_\mathrm{int}$, with $\hat{H}_\mathrm{s}$ and $\hat{H}_\mathrm{m}$ corresponding to the system and meter free Hamiltonians, respectively. $\hat{H}_\mathrm{int}$ represents the interaction term, which couples system and meter observables. First, the system observable $\hat{O}_\mathrm{s}$ eigenstate should not be disturbed by the measurement:

$$\left[\hat{H}_\mathrm{int}, \hat{O}_\mathrm{s}\right] = 0. \tag{1}$$

Secondly, the measured observable should be a constant of motion which prevents feeding back uncertainties of the non-commuting observables during the system free evolution between the two measurements:

$$\left[\hat{H}_\mathrm{s}, \hat{O}_\mathrm{s}\right] = 0. \tag{2}$$

The system observables satisfying criteria eq. 1 and eq. 2 are called QND observables. The two criteria guarantee the measurement repeatability. The QND measurement precision is limited by the coupling strength and the measurement time, but not by the measurement back-action. The minimum uncertainty which can be achieved corresponds to the standard quantum limit, which is the ground state uncertainty of the measured observable. In experiments, coupling between system and the meter is never infinitely strong which implies that the measurement does not project the state instantaneously. Leakage of energy to the environment during measurement and free evolution of the system destroys the quantum state. Following the terminology in [Cle+10] we include dissipation in the system Hamiltonian, thus measurements taking longer than the system energy relaxation time are non QND.

Implementing QND measurements of mechanical and optical oscillators usually relies on the nonlinear interaction with meter. Using mechanical systems was found to be impractical due to weak nonlinearity [Cav+80; BO96]. QND schemes were first realized in the domain of nonlinear quantum optics [BK96] with the aim of achieving noiseless telecommunication and quantum-limited sensing. The system and the meter were represented by Gaussian states interacting via nonlinear media provided by optical crystals [LSY89; Buc+01] and cold trapped atoms [Roc+97]. The level of QNDness was characterized by the quantum correlations between quadratures of the output signal and meter beams [Roc+92; GLP98].

Measurement and manipulation of individual quantum systems was first realized with Rydberg atoms [HR06]. The methods used in quantum optics and atomic physics were later adopted for the microwave superconducting quantum electronics. Superconducting artificial atoms became one of the leading platforms for the implementation of scalable quantum computing architectures, and QND measurements play an essential role in quantum error correction algorithms.

1.2 Superconducting circuits

Superconducting circuits with macroscopic dimensions can operate in the quantum regime if they have discrete spectrum of energy levels with spacing exceeding width of the levels. Due to low dissipation in the superconducting circuits the width of energy levels can be much smaller than their separation. In classical metallic superconductors the phenomenon of the non-dissipative current is explained by the microscopic theory developed by Bardeen, Cooper, and Schrieffer (BCS theory) [BCS57]. According to the theory, electrons with opposite spin and momentum experience weak attractive interaction mediated by phonons in the lattice. Coupled electrons form Cooper pairs with size orders of magnitude larger than the average spatial separation between single electrons. As a consequence, wavefunctions of individual Cooper pairs overlap, and they form a correlated collective state. Single-particle excitations, called quasiparticles, comprise additional degrees of freedom for the circuit. However, their energy is separated from the ground state by the superconducting energy gap Δ, the energy required to break the Cooper pair. Pure aluminum, the commonly used superconductor, has $\Delta = 1.2\,\mathrm{K}$, and thermal quasiparticle excitations can be neglected, although non-thermal quasiparticles can often play an important role in dissipation and dephasing.

In the macroscopic theory of superconductivity the ensemble of Cooper pairs is described by the collective wavefunction $\psi(\mathbf{r}, t) = \sqrt{n(\mathbf{r}, t)}e^{i\varphi(\mathbf{r},t)}$. The squared modulus of the wavefunction has a meaning of the Cooper pairs density, while gradient of the phase φ is related to the superconducting current density

$$\mathbf{j}_\mathrm{s} = (2e)n_\mathrm{s}\left[\frac{\hbar}{2m_\mathrm{e}}\nabla\varphi(\mathbf{r}, t) - \frac{2e}{2m_\mathrm{e}}\mathbf{A}(\mathbf{r}, t)\right], \tag{3}$$

where $\mathbf{A}$ is the vector potential satisfying $\mathbf{B} = \nabla\times\mathbf{A}$. The first manifestation of the quantum nature of the superconductivity is fluxoid quantization in the closed superconducting loop. It

can be derived by integrating the expression for the superconducting current density along the closed contour inside the superconductor:

$$n_{\mathrm{s}}\frac{2m_{\mathrm{e}}}{2e}\oint_C \mathbf{j}_{\mathrm{s}}\cdot\mathrm{d}\ell+\int_S \mathbf{B}\cdot\mathrm{d}S=\frac{\hbar}{2e}\oint_C \nabla\varphi(\mathbf{r},t)\cdot\mathrm{d}\ell=k\Phi_0, \tag{4}$$

where $\Phi_0=h/(2e)$ is the flux quantum, and k is the integer number. The integral of the phase gradient gives $2\pi k$ because the superconductor wavefunction has to be single valued after tracing around the contour. The left hand side of this equation defines the *fluxoid*, which is a sum of the external magnetic field $\Phi_{\mathrm{ext}}=B\cdot S$, and flux generated by the superconducting current.

One of the basic superconducting circuits is the quantum harmonic resonator, which has equidistant energy levels, and can exchange multiple photons. Therefore it can be used to model phonons in the crystals, and vibrations in the molecules. The resonator circuit can be represented in terms of inductances and capacitances which store the charging and magnetic energy. The dynamics of the resonator is described by a single degree of freedom. For example, if the flux ϕ in the superconducting loop plays a role of a coordinate, the charge q of the superconducting island is the conjugate momentum, with commutation relation $[q,\phi]=-i\hbar$. The Hamiltonian of the resonator

$$H=\frac{q^2}{2C}+\frac{\phi^2}{2L}, \tag{5}$$

where C is the capacitance and L is the inductance.

Circuits with anharmonic energy spectrum play a role of artificial atoms and spins. The key element in many superconducting atoms is the Josephson tunnel junction. It consists of the two superconducting electrodes separated by a thin insulating barrier. If the thickness of the barrier is smaller than the superconducting coherence length ξ, the wavefunctions of the two superconductors overlap, and Cooper pairs can tunnel coherently through the barrier. At a zero voltage bias the current through the junction is a sinusoidal function of the superconducting phase difference φ between the two electrodes $I=I_{\mathrm{c}}\sin\varphi$, with maximal value I_{c} which is called the critical current. The coupling energy stored in the Josephson junction equals

$$E_{\mathrm{J}}(1-\cos\varphi), \tag{6}$$

where $E_{\mathrm{J}}=I_{\mathrm{c}}(\Phi_0/2\pi)$, and $\Phi_0=h/(2e)$ is the flux quantum. If charging effects can be neglected, the Josephson junction behaves as a nonlinear inductance

$$L_{\mathrm{J}}=L_{\mathrm{J0}}/\cos\varphi,\quad L_{\mathrm{J0}}=\frac{1}{E_{\mathrm{J}}}\left(\frac{\Phi_0}{2\pi}\right)^2 \tag{7}$$

which can be used to construct nonlinear couplers [Kou+18b; Voo+18], parametric amplifiers [Cas+08; Ber+10; Whi+15; RD16b], and circuits with anharmonic spectra [DM04; CW08].

The atom-field coupling strength depends on the transition dipole moment between the states of electron in the atom, and on the value of the zero field fluctuations. Natural atoms have a small dipole moment, and achieving strong coherent coupling was possible only for highly excited atoms for which the electron wavefunction has large spatial extent [SWM10]. The dipole moment of the superconducting macroscopic atoms is defined by the circuit size and geometry. Besides that, electromagnetic field can be confined in a small volume to generate large zero point fluctuations. cQED allows for strong and ultra-strong coupling regimes, when coupling strength is comparable with the atom and resonator frequency [Bau+16; Yos+17].

The drawback of the large dipole moment of artificial atoms is their coupling to microscopic defects and spurious environmental modes, which in turn leads to decoherence and cross-talk. For example, the first superconducting qubit, the Cooper pair box (CPB) [NPT99] had coherence times of $\sim 1\,\mathrm{ns}$, which are comparable to the time needed for one operation and orders of magnitude shorter than needed for the fault-tolerant operation. The working principle of the CPB qubit is based on tunneling of Cooper pairs from the superconducting island to ground through the Josephson junction. The number of Cooper pairs on the island is controlled by the capacitively coupled voltage source. The CPB has large charge dispersion, and the qubit is susceptible to charge noise.

A significant effort was made to protect superconducting qubits from decoherence, and after two decades the coherence time increased to the millisecond range. This was achieved by both improving the materials, and by decoupling atoms from the environment. In the transmon qubit the protection from noise was achieved by suppressing the charge dispersion [Koc+07] at the expense of the atom anharmonicity. The typical transmon anharmonicity is around few percent of the transition frequency, which limits the qubit operation speed. Another way to suppress the sensitivity to charge noise is building atoms from high impedance circuits, like the fluxonium atom [Man+09]. In such circuits the zero point charge fluctuations are much smaller than charge of the single electron. Even stronger decoupling from the environment can be realized with topologically protected circuits, which promise simultaneous suppression of decoherence and energy relaxation without compromising the anharmonicity[Iof+02; Smi+20; Gye+21]. In these designs the qubit is encoded in the delocalized states created in the quantum circuits with multiple degrees of freedom.

1.3 Transmon artificial atom

The transmon artificial atom consists of a Josephson junction shunted by a large capacitance. An equivalent circuit of the transmon is shown in Fig. 1a. At least one electrode of the junction forms a superconducting island (shown in blue). The second electrode can also be made as an island (floating transmon design), or can be connected to ground. Both transmon implementations have the same Hamiltonian

$$H = \frac{(q-q_\mathrm{g})^2}{2(C+C_\mathrm{s})} + E_\mathrm{J}(1-\cos\varphi) = 4E_\mathrm{C}(n-n_\mathrm{g})^2 + E_\mathrm{J}(1-\cos\varphi), \tag{8}$$

where we introduced the charging energy of a single electron $E_\mathrm{C} = e^2/2(C+C_\mathrm{s})$, and $q_\mathrm{g} = 2en_\mathrm{g}$ is the effective offset charge. The transmon Hamiltonian can be solved exactly in the phase basis [Koc+07]. The atom wavefunctions at low excitation numbers are confined in the cosine potential, and have almost harmonic spectrum with levels spacing $\simeq \sqrt{8E_\mathrm{J}E_\mathrm{C}}$ (see Fig. 1 b).

Transmon qubits are typically designed with ratio $E_\mathrm{J}/E_\mathrm{C} \geq 50$. The atom anharmonicity calculated as a difference between transition energies decreases linearly with the charging energy $E_{12} - E_{01} \simeq -E_\mathrm{C}$. Strong off-resonant pumps can induce transmon escape from the cosine potential driving the atom into a free particle state [Les+19]. Because of low anharmonicity transmon atoms are not a good approximation of the two level systems, yet they can be operated as qubits if excitation of higher levels is low.

In the transmon atom the anharmonicity is compromised in favor of suppressed sensitivity to the charge noise, which is a dominant source of decoherence for atoms operating in the Cooper pair box regime $E_\mathrm{J}/E_\mathrm{C} = 1$. The circuit energy levels E_i calculated as function of the charge offset for different ratio $E_\mathrm{J}/E_\mathrm{C}$ are shown in Fig. 1 c. We plot the energy spectrum for intermediate value of $E_\mathrm{J}/E_\mathrm{C} = 5$ (bottom panel) for illustrative purposes. The charge dispersion is defined as peak-to-peak amplitude of the energy levels, and is proportional to $e^{-\sqrt{8E_\mathrm{J}/E_\mathrm{C}}}$. Therefore, the transmon sensitivity to charge noise is suppressed exponentially with the charging energy.

1.4 Fluxonium artificial atom

The design of the fluxonium artificial atom was proposed in 2009 [Man+09] as an alternative to qubits based on superconducting islands. The fluxonium atom consists of the Josephson junction shunted by the so-called superinductance which screens the charge offsets. Here we focus on the spectrum of the fluxonium, and discuss the properties and implementation of the superinductance separately.

Fig. 2 a shows the equivalent circuit of the fluxonium. The Josephson junction and superinductance form the superconducting loop which can be biased by the external magnetic field. According to the fluxoid quantization [Tin04], the total flux threading the superconducting loop, constituted by the sum of the applied external flux and flux induced by the screening

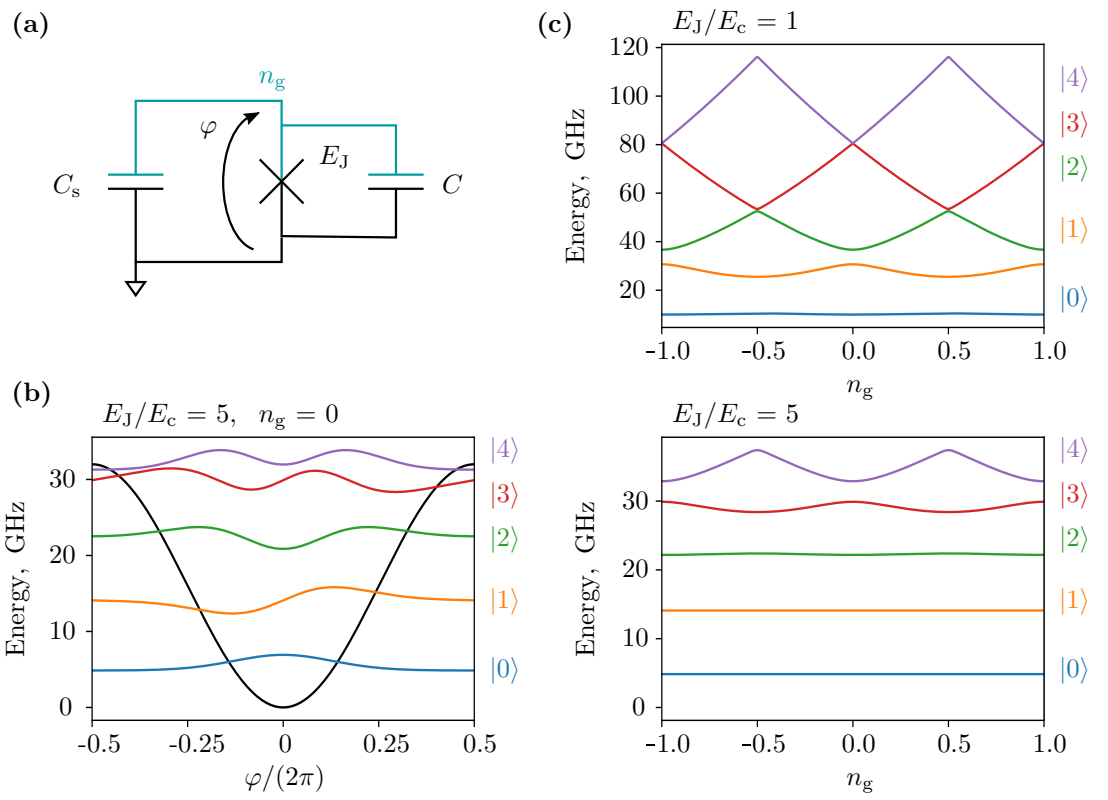

Figure 1: **Transmon artificial atom.** **(a)** Equivalent circuit of the transmon. The superconducting island shown in blue has offset charge n_g measured in the units of the Cooper pair charge. The Josephsnon junction with energy E_J and parallel plate capacitance C is shunted with capacitance $C_s \gg C$. The phase difference across the junction is φ. **(b)** The atom eigenfunctions in the phase representation calculated for $E_J = 16\,\mathrm{GHz}$ and $E_J/E_c = 5$, and the zero charge offset. **(c)** The circuit energy levels calculated for $E_J/E_c = 1$ (top panel) and $E_J/E_c = 5$ (bottom panel) as function of the offset charge. The transmon sensitivity to charge noise is suppressed exponentially with $\sqrt{E_J/E_C}$, the typical transmon ratio $E_J/E_c \geq 50$.

current, is quantized. Therefore for flux variables associated with inductance and Josephson junction ϕ_L and ϕ, assigned as shown in Fig. 2 a

$$\phi_L - \phi + \Phi_{ext} = k\Phi_0, \tag{9}$$

where k is the integer number of flux quanta in the loop. This boundary condition allows to reduce the number of degrees of freedom. We choose the junction flux variable as independent, and express $\phi_L = \phi - \Phi_{ext} + k\Phi_0$. The external flux is therefore included in the inductive energy.

The fluxonium Hamiltonian is

$$H = \frac{q^2}{2C} + \frac{1}{2L}\left(\phi - \Phi_{ext} + k\Phi_0\right)^2 + E_J \cos\varphi, \tag{10}$$

where C is the junction capacitance, L is the superinductance, and Φ_{ext} is the external magnetic field. The constant term in the Josephson energy (see eq. 6) is neglected because it does not affect the transition energies. It's worth mentioning that for the static external field there is no mistake in choosing other independent degree of freedom, and in including external flux in the Josephson energy instead of the inductive one. The eigenergies of the static Hamiltonian do not depend on the choice of variable. However, the correct assignment of the external flux is crucial for the time-dependent fields because it leads to different time evolution operators. There is no comprehensive theory on this topic yet; for the solution in the particular case of the Josephson junction SQUID biased by the external flux see Ref. [YSK19; RD21].

The inductive energy and Josephson energy form the fluxonium potential shown in Fig. 2 b (black lines) for the flux bias $\Phi_{ext} = 0$ and $\Phi_{ext} = \Phi_0/2$. The inductive energy gives rise to a parabolic potential while the Josephson energy adds the cosine oscillations on top. These

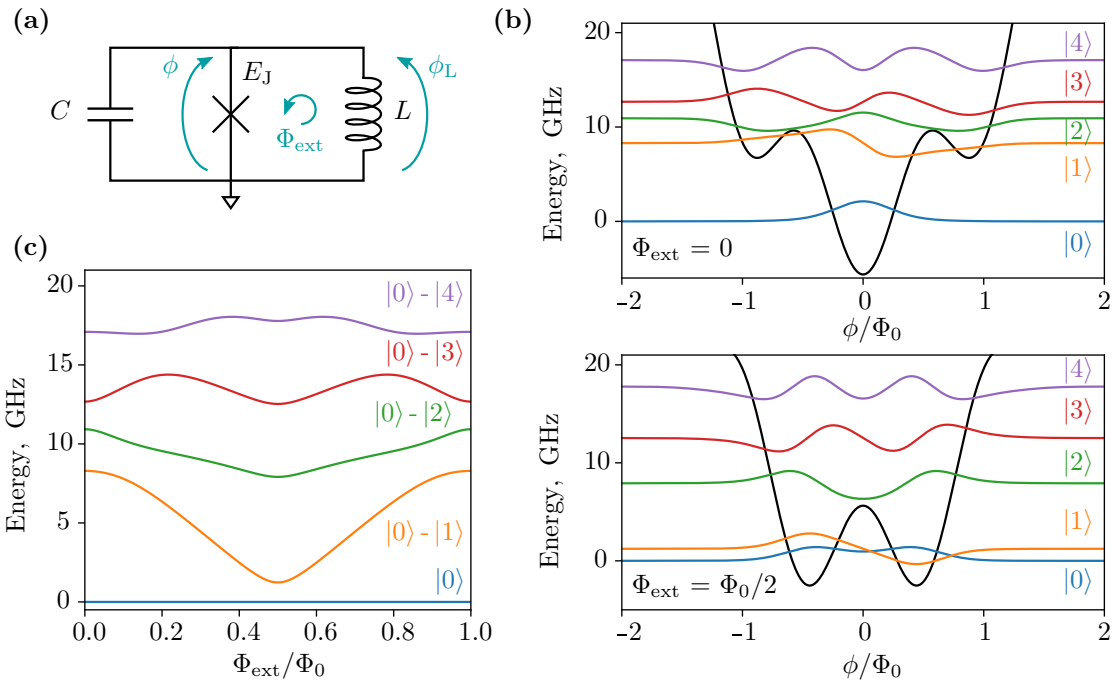

Figure 2: **Fluxonium artificial atom.** **(a)** Equivalent circuit of the fluxonium atom. The Josephson junction with energy E_J is shunted by the superinductance L. The capacitance C is given by the parallel plate capacitance of the Josephson junction and capacitance of the connecting electrodes. The applied magnetic field Φ_ext is used to tune the atom energy levels. The blue arrows with ϕ and ϕ_L labels indicate the flux variable assigned to the Josephson junction and the inductance. **(b)** Fluxonium potential energy (black lines) and first eigenfunctions of the Hamiltonian (eq. 10) calculated numerically at the zero applied field (top panel) and $\Phi_\mathrm{ext} = \Phi_0/2$ (bottom panel). The circuit parameters $C = 6.9\,\mathrm{fF}$, $L = 231\,\mathrm{nH}$ and $E_\mathrm{J}/h = 5.6\,\mathrm{GHz}$ are the same as for the device presented in Ref. [Gus+21]. The potential is shifted by the energy of the first fluxonium level. **(c)** Fluxonium spectrum as function of the applied magnetic field. Energy of the first fluxonium level is shifted to zero.

two functions are shifted relatively to each other by applying magnetic field, and the potential transforms from the single-well at the zero magnetic field to the double-well potential at half flux quantum bias. The corresponding eigenfunctions are shown in Fig. 2 b for the flux bias $\Phi_\mathrm{ext} = 0$ and $\Phi_\mathrm{ext} = \Phi_0/2$. The circuit parameters $C = 6.9\,\mathrm{fF}$, $L = 231\,\mathrm{nH}$ and $E_\mathrm{J}/h = 5.6\,\mathrm{GHz}$ are the same as for the device presented in Ref. [Gus+21].

The fluxonium energy levels are periodic functions of the external magnetic field with period of one flux quantum. Fig 2 c demonstrates the energy spectrum calculated as function of the external magnetic field by numerically diagonalizing the Hamiltonian (eq. 10) in the basis of Harmonic oscillator functions. At the spectrum extremum points, the fluxonium atom is first-order insensitive to flux noise because of zero derivative in respect to the external field. An important advantage of the fluxonium is its high anharmonicity which allows fast control gates at $|0\rangle - |1\rangle$ transition frequency without large spurious excitations of the higher levels.

The characteristic energy scales of the circuit can be calculated with transformation to the unitless variables phase $\varphi = 2\pi\phi/(\Phi_0)$, and number of Cooper pairs $n = q/(2e)$, with commutation relation $[n, \varphi] = -i$. Then the circuit Hamiltonian is

$$H = 4E_\mathrm{C}n^2 + \frac{1}{2}E_\mathrm{L}(\varphi - \varphi_\mathrm{ext})^2 + E_\mathrm{J}\cos\varphi, \tag{11}$$

with $E_\mathrm{C} = e^2/(2C)$ the charging energy of a single electron, and E_L the inductive energy. The impedance and the charge zero point fluctuations of the harmonic mode at the zero Josephson energy are

$$Z = \sqrt{\frac{L}{C}}, \quad q_\mathrm{zpf} = 2e\sqrt{\frac{R_\mathrm{Q}}{4\pi Z}}, \tag{12}$$

where $R_Q = h/(2e)^2 \approx 6.5\,\mathrm{k}\Omega$ is the resistance quantum.

1.4.1 Superinductance

The shunting superinductance has to fulfill several requirements. First, its impedance should exceed the resistance quantum $Z > R_Q$, which guarantees that the charge zero point fluctuations (see eq. 12) are suppressed below the charge of the single electron $q_{zpf} < e$. The second requirement is low microwave losses for the coherence of the circuit, and perfect conduction at DC current which allows to shunt the charge offsets between the Josephson junction electrodes. Finally, the spurious self-resonant modes of the superinductance should be above the first atom transition and, ideally, should be detuned from the atom transitions to prevent enhanced atom energy decay. Constructing such superinductance is not trivial. Superconducting wires have parasitic capacitance to ground, and impedance of a straight superconducting wire usually does not exceed the vacuum impedance $Z = 377\,\Omega$. Typically, superinductances are made out of the Josephson junction chains or from superconducting materials with high kinetic inductance.

Kinetic inductance of the superconducting wire is associated with the momentum of the Cooper pairs. The energy stored in the kinetic motion

$$E = \int n_s \frac{mv^2}{2} dV = \frac{1}{2} L_{kin} I^2, \tag{13}$$

here n_s is density of Cooper pairs, $m = 2m_e$ is their mass, v is the velocity, and I is superconducting current. For wire with length ℓ and cross-section area S current $I = 2en_s vS$, and the kinetic inductance equals

$$L_{kin} = \frac{2m_e}{n_s(2e)^2} \frac{\ell}{S}. \tag{14}$$

The kinetic inductance is also present in normal metals $L_{kin} = m_e \ell/(n_e e^2 S)$. However, the ratio between reactive impedance and resistance $\omega L_{kin}/R = \omega\tau$, where the electron scattering time $\tau \sim 10\,\mathrm{fs}$, and kinetic inductance gives significant contribution only at frequencies $\omega \sim 10\,\mathrm{THz}$.

The kinetic inductance of the superconductors scales inversely with the density of Cooper pairs which decreases with increasing kinetic energy $n_s = n_{s0}(1-j^2/j_{crit}^2)$, here j is the superconducting current, and j_{crit} is the critical current at which superconductivity breaks [Tin04]. Therefore the kinetic inductance has intrinsic nonlinearity

$$L_{kin} \approx L_{kin,0} \left(1 + \frac{j^2}{j_{crit}^2}\right). \tag{15}$$

Disordered superconductors with mean free path of normal electron much smaller than the superconductor coherence length $\ell_e \ll \xi$ typically have large kinetic inductance. Mattis-Bardeen theory for the skin effect in superconductors and normal metals relates the kinetic inductance to the normal state resistance R_n [MB58; Tin04]. In the limit of low temperatures compared to the critical temperature $T \ll T_c$

$$L_{kin} = \frac{\hbar R_n}{\pi\Delta}, \tag{16}$$

here $\Delta \approx 1.76 k_b T_c$ is the BCS superconducting gap. Materials with high normal state resistivity $\rho = RS/\ell$ possess high kinetic inductance. For example, NbTiN films with $\rho = 100{-}200\,\mu\Omega\,\mathrm{cm}$, and $T_c \approx 9\,\mathrm{K}$ have kinetic inductance per square $L_{kin} = 0.05{-}0.1\,\mathrm{nH}/\square$ [Sam+16; Haz+19; Pit+20].

Only recently geometric superinductances with $Z > R_Q$ were built by winding the superconducting wire in compact spirals [Per+20], exploiting the fact that the characteristic impedance of the spiral scales linearly with the number of turns. To further increase the impedance, the substrate under the spiral is etched to form a suspended membrane. This reduces the effective dielectric constant, and, consequently, the capacitance of the circuit. The compact spirals with diameter $50{-}100\,\mu\mathrm{m}$ and ~ 100 turns were made from 100 nm wide aluminum wires with kinetic inductance $\lesssim 10\%$ of the total inductance.

1.4.2 Josephson junction chains as superinductance

In the first fluxonium implementation the superinductance was build from a chain of Josephson junctions [Man+09]. The equivalent circuit of the chain is shown in Figure 3. The chain can be treated as a lumped element inductance if the charging effects and the dynamics of individual junctions can be neglected. This approximation is valid if the drive frequency is much smaller than self-resonant frequency of the single junction. Assuming that the junctions are identical, the Hamiltonian of the chain with k junctions is

$$H = -\sum_k E_\mathrm{J} \cos\left(\frac{\varphi}{k}\right) = k\frac{(\Phi_0/2\pi)^2}{L_\mathrm{J0}} \cos\left(\frac{\varphi}{k}\right) \tag{17}$$

where φ is a total phase difference across the chain. For large k the Tailor expansion of the cosine up to the fourth order in its argument gives

$$H \approx -kE_\mathrm{J} + \frac{1}{2}\frac{(\Phi_0/2\pi)^2}{kL_\mathrm{J0}}\varphi^2 - \frac{1}{24}\frac{(\Phi_0/2\pi)^2}{k^3 L_\mathrm{J0}}\varphi^4. \tag{18}$$

Here the first term is a constant offset, the second term corresponds to the energy of linearized inductance and the last term gives the self-Kerr coefficient. The effective linear inductance of the chain scales with the number of junctions $L_\mathrm{lin} = kL_\mathrm{J0}$, while the ratio between nonlinear and linear terms decreases quadratically $H_\mathrm{nonlin}/H_\mathrm{lin} \propto 1/k^2$.

We have to go beyond the lumped-element model to obtain the full spectrum of modes in the Josephson junction chain. The chain can be approximated with an array of harmonic oscillators. Each Josephson junction is considered as linear inductor, and both junction parallel plate capacitance and capacitance to ground are taken into account. The solution of the array Hamiltonian gives the dispersion relation for the harmonic modes [Mas+12]

$$\omega_k = \omega_\mathrm{p}\sqrt{\frac{1-\cos(\pi k/N)}{C_\mathrm{g}/(2C)+1-\cos(\pi k/N)}} \tag{19}$$

here $\omega_\mathrm{p} = 1/\sqrt{L_\mathrm{J0}C}$ is the plasma frequency of a single junction, N is the number of Josephson junctions in array, $k \in [-N/2, N/2]$. Capacitance to ground leads to reduction of the chain plasma frequency. Figure 3 b shows the calculated spectrum of modes for different ratios C/C_g. High ratio C/C_g is preferable for the use of junction chain as superinductance because modes concentrate around plasma frequency, and first self-resonant mode of the chain can be far detuned from the atom transition frequency.

Decoherence in the Josephson junction chains can be caused by phase-slip events: a change of the phase drop across single junction by multiples of 2π. Quantum phase slip tunneling events occur due to fluctuations of phase, and can be dissipationless. For the fixed phase difference across the chain φ_bias the phase slip in one junction results in renormalization of the phase across all other junctions by $(\varphi_\mathrm{bias}-2\pi)/N$. The inductive energy of the chain therefore changes from $E_\mathrm{J}\varphi_\mathrm{bias}^2/2N$ to $E_\mathrm{J}(\varphi_\mathrm{bias}-2\pi)^2/2N$. For large ratio between Josephson and charging energy $E_\mathrm{J}/E_\mathrm{C} \gg 1$ for individual junctions the quantum phase fluctuations are small, and phase slip rate is suppressed exponentially [MLG02; Pop+10; RPH13]

$$v = N\frac{1}{h}\frac{4}{\sqrt{\pi}}(8E_\mathrm{J}^3E_\mathrm{C})^{1/4}\exp\left(-\sqrt{8\frac{E_\mathrm{J}}{E_\mathrm{C}}}\right). \tag{20}$$

Large $E_\mathrm{J}/E_\mathrm{C}$ ratio is achieved by increasing area of the Josephson junction. For $\sim 1\,\mu\mathrm{m}^2$ large Junctions with ratio $E_\mathrm{J}/E_\mathrm{C} \approx 100$ the measured phase slip rate $v \approx 1\,\mathrm{mHz}$ [Mas+12].

Experiments with resonators made out of JJ chains show that they fulfill all the requirements for the superinductance [Bel+12; Mas+12]. Their impedance exceeds the resistance quantum, plasma frequency $\omega_\mathrm{p} \sim 20\,\mathrm{GHz}$ [Wei+15], and the internal quality factor which quantifies microwave losses $Q_\mathrm{i} \sim 10^5$. The self-Kerr nonlinearity of Josephson junction chains made for superinductance applications is in range of $\propto$ MHz.

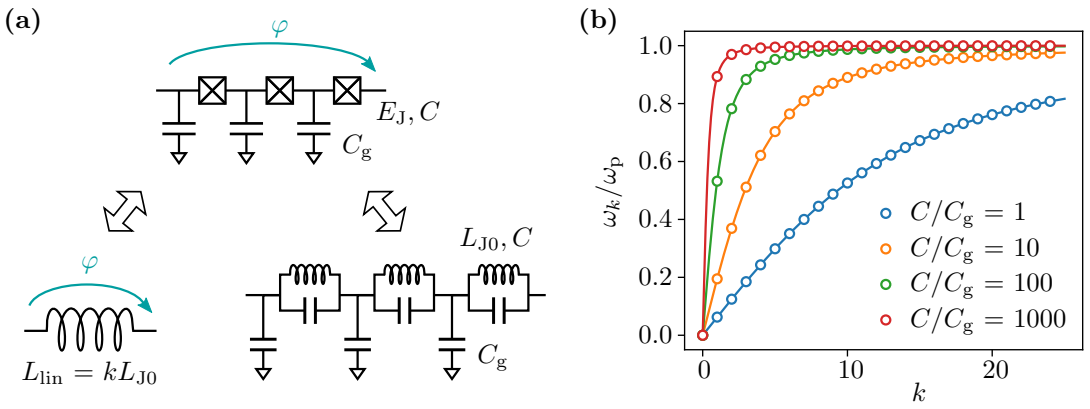

Figure 3: **Implementation of the superinductance with Josephson junction chain.** **(a)** Josephson junction chain and its representation in a lumped-element model, and harmonic oscillator array approximation. Identical junctions with Josephson energy E_J are connected in series. Each junction has the parallel plate capacitance C and capacitance to ground C_g. In the lumped-element model dynamics of the individual junctions is neglected. The chain Hamiltonian is described by a single collective variable φ which corresponds to the total phase difference across the chain. The equivalent linear inductance of the chain scales with number of junctions k. In the harmonic oscillator array approximation each junction is represented by its linear inductance L_{J0}. **(b)** Dispersion relation calculated for harmonic modes in array of 50 junctions for different ratios C/C_g. Markers show mode frequencies normalized by plasma frequency of the single junction $\omega_p = 1/\sqrt{L_{J0}C}$. Lines are guides for the eye.

1.4.3 Granular aluminum as superinductance

Granular aluminum (grAl) is obtained by evaporating pure aluminum in oxygen atmosphere. The room temperature resistivity of grAl films can be tuned in range $10-10^4\,\mu\Omega\,\mathrm{cm}$ by increasing the partial oxygen pressure during deposition. The resistivity also depends on aluminum deposition rate and temperature of the substrate. Superconductivity in grAl was a subject of research starting from 1960 [ACC66] due to a peculiar enhancement of the superconducting gap compared to bulk aluminum, and transition from superconducting to insulating behaviour, similar to transition observed in the homogeneously disordered films with increase of resistivity [Noa+13; Ivr+14]. Both the nature of the superconducting to insulator transition (SIT) and gap enhancement in grAl are still not fully understood.

GrAl consists of crystalline aluminum grains surrounded by amorphous AlO_x. The size of grains reduces drastically from $\sim 50\,\mathrm{nm}$ for pure aluminum to $3-4\,\mathrm{nm}$ in grAl films with $\rho = 100\,\mu\Omega\,\mathrm{cm}$, deposited at the room temperature [Deu+73]. Starting from this value the grain size is almost independent on the resistivity and has uniform distribution. Below $\rho = 100\,\mu\Omega\,\mathrm{cm}$ grAl films show metallic behaviour, with electron mean free path of the order of the grain size. With increasing resistivity coupling between the grains decreases, and electron mean free path becomes orders of magnitude smaller than the grain size. Despite decoupling of the grains the superconducting gap increases, and critical temperature reaches its maximum of $T_c \approx 2.2\,\mathrm{K}$ at $\rho \approx 400\,\mu\Omega\,\mathrm{cm}$ [DG81; Lev+19]. Starting from this value the superconducting gap gradually decreases, and a superconducting transition is not observed above $\rho \approx 10^4\,\mu\Omega\,\mathrm{cm}$. Instead, samples show insulating behaviour. The maximal critical temperature can be enhanced to $T_c \approx 3\,\mathrm{K}$ by depositing grAl onto cold substrates [ACC66; Pra+16]. Such films also have smaller grain size $\sim 2\,\mathrm{nm}$.

Complex conductivity of grAl obeys the Mattis-Bardeen equations for disordered superconductors [Pra+16], and the kinetic inductance can be calculated from the normal state resistance and the superconducting gap (see eq. 16). Kinetic inductance in GrAl films with resistivity close to SIT is in range of $\mathrm{nH}/\square$, with the kinetic inductance fraction L_{kin}/L_{total} close to unity. GrAl inductors have intrinsic nonlinearity which can be estimated by modeling grAl as a network of

connected Josephson junctions [Mal+18]. The self-Kerr coefficient of the fundamental mode

$$K_{11} \propto -a\frac{\omega_1^2}{j_{\mathrm{crit}} V_{\mathrm{grAl}}} \tag{21}$$

here a is the grain size, ω_1 is the mode frequency, j_{crit} is the critical current density, and V_{grAl} is the grAl volume. The grAl nonlinearity can be tuned over six orders of magnitude by changing the circuit volume and grAl resistivity. GrAl films with weak nonlinearity $K_{11} \lesssim 1\,\mathrm{kHz}$ can be used to implement superinductances [Grü+19], circuits with $K_{11} = 1{-}10\,\mathrm{kHz}$ are suitable for kinetic inductance detectors [Val+19] and parametric amplifiers [Vis+16; Boc+14], while nonlinearity of order of MHz is sufficient for constructing transmon qubits [Win+20b].

The dispersion relation for modes in grAl stripline resonators is similar to Josephson junction arrays. The plasma frequency $\omega_{\mathrm{p}} = \sqrt{2eI_{\mathrm{c}}/\hbar C}$, where I_{c} is the critical current and C is the grain capacitance. Due to difference in size the grain capacitance is much smaller than the parallel plate capacitance of artificial Josephson junctions. Therefore plasma frequency of grAl used for superinductances is at least 3-4 times larger compared to junction arrays. Resonators with low resistivity can easily have effective plasma frequency around 100 MHz, above the superconducting gap [Mal+18].

Resonators made out of grAl have internal quality factors Q_{i} above 10^5 [Grü+18], and they can handle parallel magnetic fields up to 1 T without degradation of Q_{i} [Bor+20]. Kinetic inductance scales inversely with the density of Cooper pairs, therefore devices made out of materials with dominating L_{kin} are susceptible to quasiparticle excitations, and grAl resonators are not an exception. The number of quasiparticles observed in experiments with different superconductors is many orders of magnitude higher than expected in thermal equilibrium at dilution refrigerator temperatures [Vis+11; Cat+11; Wan+14; Pop+14; Lev+14]. Comparison of loss mechanisms in grAl resonators of different geometries indicates that non-equilibrium quasiparticles can be a dominant source of dissipation in resonators with high impedance [Grü+18].

Such non-equilibrium quasiparticles can be generated by environmental and cosmic radioactivity. Continuous monitoring of grAl resonators reveals sudden frequency drops [Grü+18] similar to response of the microwave kinetic inductance detectors [Day+03]. High-energy particles hitting the substrate create phonons which in turn break Cooper pairs in the superconductor. Propagating pair-breaking phonons generate quasiparticle bursts [Kar+19] which lead to time-correlated errors in multiqubit arrays [Wil+21], undermining quantum error correction with surface codes [Fow+12]. An order of magnitude reduction of the quasiparticle bursts rate can be achieved by cleaning sample environment from radioactive contaminants, and by shielding cryostats from cosmic radiation with lead walls and by placing them in deep underground facilities [Car+21]. Another way to mitigate correlated errors is to hinder propagation of high frequency substrate phonons by building phonon traps or by engineering the phonon dispersion. Phonon traps are made from low gap superconducting films covering the substrate surface which downconvert frequency of phonons via electron-phonon interaction. [Hen+19; Mar21]

2 Dispersive interaction

The dispersive readout scheme was adopted from cavity quantum electrodynamics. It originates from the transverse interaction between the atom and the readout resonator. In the cQED it can be implemented with linear inductive or capacitive coupling, and is currently a prevailing readout scheme due to the simplicity of the design. Inherently, the transverse interaction is non-QND; in resonant case it can be used to generate maximally entangled atom-resonator state [Wal+04], provided that the coherent coupling rate g is larger than the energy decay rates of resonator κ and atom Γ, and the atom decoherence rate Γ_φ (strong coupling $g > [\kappa, \Gamma, \Gamma_\varphi]$ [RBH01b]). However, in the dispersive regime, when the detuning between atom and resonator $\Delta = \omega_\mathrm{a} - \omega_\mathrm{r}$ is large compared to the coupling strength $\Delta \gg g$, the off-resonant transverse interaction becomes QND in first order approximation.

To gain insight into the underlying model we use simplified representation of the artificial atom as a two-state system (spin). It is important to mention that the two-state model of the atom is very illustrative and allows qualitative description of the dispersive readout. However, virtual and resonant transitions between higher atom-resonator levels can strongly affect the dispersive shift and the atom relaxation rate. Therefore, numerical simulation of the many level atom-resonator Hamiltonian and transition matrix elements is usually needed for accurate quantitative agreement with experiments [Hou+08].

The spin-photon transverse interaction is described with the Rabi Hamiltonian:

$$H = \omega_\mathrm{r} a^\dagger a + \frac{\omega_{01}}{2}\sigma_z + g\left(a^\dagger + a\right)\sigma_x, \tag{22}$$

where the first two terms correspond to the free Hamiltonians of the resonator and spin, respectively. The last term shows coupling of the resonator displacement degree of freedom to the spin σ_x degree of freedom. Another simplification, the rotating wave approximation (RWA), allows to neglect the two-photon transition terms in the coupling Hamiltonian if the corresponding matrix elements are much smaller compared to the single-photon processes. In the dispersive limit $g \ll \Delta$, the resulting Hamiltonian can be diagonalized perturbatively by the unitary transformation

$$U = \exp\left[\frac{g}{\Delta}(a^\dagger \sigma_- - a\sigma_+)\right]. \tag{23}$$

Expanding $U^\dagger H U$ up to the first order in g yields the dispersive Hamiltonian

$$H = \left(\omega_\mathrm{r} + \chi\sigma_z\right) a^\dagger a + \frac{1}{2}\left(\omega_{01} + \chi\right)\sigma_z \tag{24}$$

with $\chi = g^2/\Delta$. The first term in eq. 24 demonstrates that the resonator frequency depends on the atom state, and, vice versa, the atom frequency depends on the resonator excitation number. The dispersive regime owes its name to the analogy with the atom-dependent refractive index of a cavity. The atom plays a role of an effective dielectric which changes the resonator frequency. The atom state can be measured via homodyne or heterodyne detection.

The dispersive interaction Hamiltonian $H_\mathrm{int} = \chi\sigma_z a^\dagger a$ satisfies the QND criteria (see eq. 1, 2), with the caveat that we neglected higher order terms in the expansion. Achieving strong dispersive coupling $\chi \sim \kappa$ along with improvement of the superconducting atoms relaxation time and parametric amplification rendered possible single-shot repeated measurements and detection of the atom quantum jumps [Mal+09; VSS11; Liu+14], which is a prerequisite for implementing continuous quantum error correction.

The quantum feedback from dispersive measurement causes atom dephasing. This can be seen intuitively from the eq.24 because fluctuations in the resonator photon number lead to jitter of the atom frequency. Large detuning between resonator and atom is advantageous in this case as drives applied at the atom frequency do not produce spurious excitations in the resonator. Therefore the amplitude of pulses used for the coherent manipulation of the atom state can be high, providing fast single-qubit gates. Furthermore, resonator frequency is usually designed to be above 4 GHz which corresponds to the thermal energy of 200 mK. The physical temperature of the device is usually order of magnitude smaller. One can find the thermal occupation of

the harmonic oscillator excited state using Boltzmann distribution $p_1/p_0 = \exp(-hf_\mathrm{r}/k_\mathrm{B}T)$, here p_0 and p_1 are the probabilities of the ground and excited states, and k_B is the Boltzmann constant. At physical temperature $T = 30\,\mathrm{mK}$ the thermal excitation of undriven resonator is $\approx 0.2\%$, and atom dephasing between measurement pulses is suppressed.

The expected residual non-QNDness of the dispersive readout can be estimated by diagonalizing the initial Rabi Hamiltonian within the rotating wave approximation (RWA). The resulting Jaynes-Cummings Hamiltonian has exact analytical solution for the eigenvalues and eigenvectors. The Jaynes-Cummings interaction entangles states with the same total excitation number, and the dressed eigenvestors take the form [Bla+20]:

$$\begin{aligned} |\overline{g,n}\rangle &= \cos(\theta_n/2)\,|g,n\rangle - \sin(\theta_n/2)\,|e,n-1\rangle \\ |\overline{e,n-1}\rangle &= \sin(\theta_n/2)\,|g,n\rangle + \cos(\theta_n/2)\,|e,n-1\rangle \end{aligned} \tag{25}$$

for $n \geq 1$, with the mixing angle $\theta_n = \arctan(2g\sqrt{n}/\Delta)$. The resonator excitation number at which numerator in the definition of the mixing angle becomes comparable to the detuning between atom and resonator is called the *critical photon number*

$$n_\mathrm{crit} = \Delta^2/(2g)^2. \tag{26}$$

In the dispersive limit $g \ll \Delta$ and for the resonator excitation much smaller than the critical photon number the dressed eigenvectors are primarily the uncoupled eigenvectors with mixing factor of $n(g/\Delta)^2$. The probability of the resonator to absorb photon from the atom is small, and interaction takes place only via virtual photon exchange. Nevertheless, even the weak entanglement leads to the Purcell enhancement of the atom relaxation rate [Pur46]. For the state $|\overline{e,0}\rangle$ the total energy relaxation

$$\gamma_\mathrm{total} \simeq \gamma + \left(\frac{g}{\Delta}\right)^2 \kappa \tag{27}$$

where γ and κ are the energy relaxation rates of the uncoupled atom and the resonator, respectively.

2.1 Dynamics of the dispersive measurement

In this section we focus on the dynamics of the readout resonator during the dispersive atom measurement. Here we introduce coupling of the readout resonator to the measurement apparatus, and demonstrate time evolution of the output states. We derive the expression for the measurement signal to noise ratio (SNR) and prepare the ground for discussing the high power readout.

Input-output theory

In our derivation of the dispersive coupling we treated the atom and resonator as isolated quantum system, neglecting coupling to the environment, control and readout fields. In order to extract information about the atom state encoded in the frequency or phase of the readout resonator one has to send signal from the source and direct the outgoing (transmitted or reflected) signal to the classical measurement apparatus. This can be achieved by coupling the readout resonator capacitively to the $50\,\Omega$ transmission line. Here we focus on the measurement in reflection with corresponding schematic shown in Fig. 4. To start with, we ignore the atom and exclude it from the system dynamics, assuming that the only effect of the atom-resonator coupling is the dispersive shift of the resonator frequency. In this case the dynamics of input, output, and resonator fields is described with input-output theory [YD84]. We outline the main results of the theory without repeating the detailed derivation which can be found in Ref. [Cle+10; Bla+20].

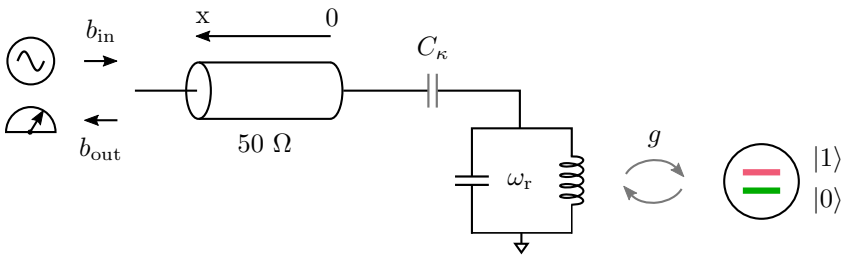

Figure 4: **Circuit schematic for dispersive atom measurement in reflection.** The readout resonator is coupled capacitively to the 50 Ω transmission line. The resonator coupling rate is κ. The readout signal sent via transmission line interacts with the readout resonator and reflected signal is measured at the output of the transmission line. The atom is shown schematically as the two level system coupled to the resonator with interaction strength g. Due to the dispersive interaction the resonator frequency acquires the atom state dependent frequency shift $\omega_{\rm r} = \omega_{\rm bare} \pm \chi_{01}/2$.

A long transmission line has a continuous spectrum of modes and is described with the Hamiltonian

$$H_{\rm tml} = \int_0^\infty {\rm d}\omega\, \hbar\omega\, b_\omega^\dagger b_\omega \tag{28}$$

with bosonic creation and annihilation operators satisfying the commutation relation $[b_\omega, b_{\omega'}^\dagger] = \delta(\omega - \omega')$. The capacitive coupling between resonator and transmission line results in the interaction Hamiltonian

$$H_{\rm int} = \frac{1}{\sqrt{2\pi}} \int_0^\infty {\rm d}\omega\, \sqrt{\kappa(\omega)}\, (b_\omega^\dagger - b_\omega)(a^\dagger - a). \tag{29}$$

Here $\sqrt{\kappa(\omega)}$ is the frequency dependent coupling constant given by the value of the coupling capacitance C_κ. The total Hamiltonian of the system consists of the resonator, transmission line, and interaction Hamiltonians, respectively:

$$H_{\rm tot} = H_{\rm r} + H_{\rm tml} + H_{\rm int}. \tag{30}$$

In the Heisenberg picture the evolution of the resonator field operator is given by the equation of motion

$$\dot{a} = \frac{i}{\hbar}[H_{\rm tot}, a]. \tag{31}$$

The following two approximations are used to simplify the calculations. The first one neglects the fast oscillating terms in the interaction Hamiltonian (RWA). The second approximation assumes that the drive is applied in the narrow range of frequencies in the vicinity of resonator frequency (Markov approximation) which is valid for $\kappa \ll \omega_{\rm r}$. This allows to replace $\kappa(\omega)$ with a constant value κ.

It is convenient to introduce bosonic operators for the input and output field corresponding to the waves propagating in the transmission line in opposite directions. The transmission line charge operator takes the form of

$$Q^{\rightleftarrows}(x,t) = i \int_0^\infty {\rm d}\omega \sqrt{\frac{\hbar\omega c}{4\pi v}}\, \exp^{i\omega(t \pm x/v)}\, b_\omega^{\dagger \rightleftarrows} - {\rm H.c.} \tag{32}$$

where c is the transmission line capacitance per unit length, and v is the phase velocity. The input and output mode field operators are defined as

$$\begin{aligned} b_{\rm in}(t) &= \frac{-i}{\sqrt{2\pi}} \int_{-\infty}^\infty {\rm d}\omega\, b_\omega^{\rightarrow} \exp^{-i(\omega-\omega_r)t} \\ b_{\rm out}(t) &= \frac{-i}{\sqrt{2\pi}} \int_{-\infty}^\infty {\rm d}\omega\, b_\omega^{\leftarrow} \exp^{-i(\omega-\omega_r)t} \end{aligned} \tag{33}$$

The boundary condition at $x = 0$ yields the first result of the input-output theory

$$b_{\rm out}(t) - b_{\rm in}(t) = \sqrt{\kappa} a(t). \tag{34}$$

The equation of motion for the resonator field operator is written in the form of the so called quantum Langevin equation (in a frame rotating at the drive frequency)

$$\dot{a}(t) = -i(\omega_\mathrm{r}-\omega_\mathrm{d})a-\frac{\kappa}{2}a-\sqrt{\kappa}\,b_\mathrm{in}(t), \tag{35}$$

here ω_r and ω_d are the resonator and drive frequencies, respectively. The second term of this equation shows that κ corresponds to the energy loss rate in the resonator. It can also be expressed through physical parameters of the system $\kappa = Z_\mathrm{tml}C_\kappa^2\omega_\mathrm{r}^2/C_\mathrm{r}$ [Bla+20].

In continuous wave measurements when all the transient process saturate the system is in its steady state $\dot{a} = 0$. The corresponding amplitude of the input field can be calculated using eq. 35

$$|b_\mathrm{in}| = \left|\frac{1}{\sqrt{\kappa}}\left(-i(\omega_\mathrm{r}-\omega_\mathrm{d})-\frac{\kappa}{2}\right)\right|\sqrt{\bar{n}}. \tag{36}$$

The amplitude of the input field has units of $\sqrt{\mathrm{Hz}}$. The square of the amplitude corresponds to the photon flux, and is related to the input power $|b_\mathrm{in}|^2 = P_\mathrm{in}/\hbar\omega_\mathrm{d}$. In steady state the input power equals output power and

$$P = \hbar\omega\left\langle b_\mathrm{out}^\dagger b_\mathrm{out}\right\rangle = \hbar\omega\frac{\kappa}{4}\left\langle a^\dagger a\right\rangle, \tag{37}$$

the factor of $\frac{1}{4}$ for the field inside the resonator is due to the interference of propagating waves.

Time evolution of the fields

The resonator subject to the classical drive evolves into the coherent steady state $|\alpha\rangle$ which is an eigenvector of the resonator annihilation operator. The corresponding eigenvalue α is a complex number. By introducing the dimensionless quadratures of the harmonic oscillator field $I = (a^\dagger+a)/2$ and $Q = (a^\dagger-a)/2$ the coherent state can be represented as a vector on the complex plane. The real and imaginary parts of α correspond to the average values of the quadratures $\mathrm{Re}(\alpha) = \langle I\rangle$, and $\mathrm{Im}(\alpha) = \langle Q\rangle$. The length of the vector is related to the average photon number $|\alpha|^2 = \bar{n}$. The commutation relation for the quadratures $[I, Q] = i/2$. A distinctive feature of the coherent state is the fact that the uncertainties of the quadratures are minimal allowed by the Heisenberg uncertainty principle $\langle\Delta I\rangle = \langle\Delta Q\rangle = 1/2$, and match the amplitude of the zero point fluctuations. The uncertainties do not scale with the photon number, and do not grow in time.

The dispersive coupling to the atom results in the atom state-dependent shift of the dressed resonator frequency $w_\mathrm{r} = w_\mathrm{r0}\pm\chi_{01}/2$, where w_r0 is the resonator bare frequency, and χ_{01} is the separation between resonator frequencies for atom in $|0\rangle$ and $|1\rangle$ states. By integrating the Langevin equation of motion (eq. 35) we find evolution of the field inside the readout resonator

$$a(t) = (a_0-a_\infty)\exp^{-i(\omega_\mathrm{r}-\omega_\mathrm{d})t-\kappa t/2}+a_\infty \tag{38}$$

where a_0 is the initial state, and $a_\infty = b_\mathrm{in}\sqrt{\kappa}/(-i(\omega_\mathrm{r}-\omega_\mathrm{d})-\frac{\kappa}{2})$ is the steady coherent state for the input field b_in. The quadratures of the resonator field evolve with rate of $\kappa/2$, while photon number in the resonator evolves with rate κ. Fig. 5 a shows the calculated evolution of the field inside the resonator on a time scale $t = 10/\kappa$. The drive is applied at the bare resonator frequency detuned from the dressed frequency by $\chi_{01}/2$. The initial boundary condition corresponds to the vacuum state in the resonator $a_0 = 0$, and the drive amplitude is chosen to give $\bar{n} = 10$ in the coherent steady state (see eq. 37).

Signal reflected from the resonator is measured at the output of the 50 Ω transmission line. We use the input-output relation (eq. 34) to calculate the evolution of the output pointer states. Fig. 5 b demonstrates the dynamics of the output field quadratures for $t = 10/\kappa$, and different ratio between dispersive shift and the resonator coupling rate. The output field pointer states trace out complex trajectory in the IQ-plane. In the beginning of the evolution, pointer states follow the $\mathrm{Re}(b_\mathrm{out})$ axis, while information about the atom state is contained entirely in the $\mathrm{Im}(b_\mathrm{out})$ quadrature of the output field. Therefore the signal to noise ratio of the dispersive readout is poor at the small integration times. The optimal 180° phase separation of the output field steady states for atom in $|0\rangle$ and $|1\rangle$ is achieved for $|\chi_{01}| = \kappa$.

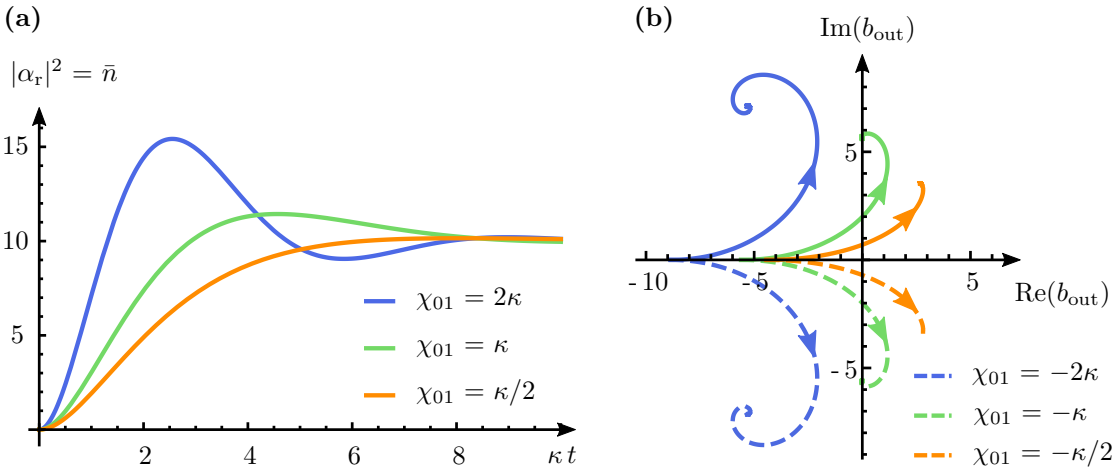

Figure 5: **Dynamics of the dispersive readout. (a)** Resonator ringup from the vacuum state to the steady coherent state with average excitation of $\bar{n} = 10$. The resonator is driven at the bare frequency which is detuned from the dressed resonator frequency by the value of the dispersive shift $\chi_{01}/2$. The resonator population is calculated using the equation of motion (see eq. 35) for different ratios of the dispersive shift χ_{01} and the resonator linewidth κ. **(b)** Time evolution of the output field quadratures calculated on the same time scale as in panel (a) using eq. 34. The solid and dashed lines demonstrate the position of the pointer states for positive and negative dispersive shifts, respectively.

2.2 Signal to noise ratio

By applying the Fourier transform to eq. 34 one obtains the relation between input and output signal in frequency domain:

$$b_{\mathrm{out}}(\omega) = \frac{w - w_{\mathrm{r}} - i\kappa/2}{w - w_{\mathrm{r}} + i\kappa/2}\, b_{\mathrm{in}}(\omega). \tag{39}$$

In the following, we assume that there are no spontaneous atom transitions during the measurement time. If the resonator is driven at the bare frequency $\omega = \omega_{\mathrm{r}0}$ the steady state quadratures of the output signal for the atom in $|0\rangle$ and $|1\rangle$ states equal

$$\langle I_{0,1}\rangle = \frac{\kappa^2 - \chi_{01}^2}{\kappa^2 + \chi_{01}^2}\,|\langle b_{\mathrm{in}}\rangle|\,,\ \langle Q_{0,1}\rangle = \pm\frac{2\kappa\chi_{01}}{\kappa^2 + \chi_{01}^2}\,|\langle b_{\mathrm{in}}\rangle|\,, \tag{40}$$

where the information about the atom state is contained entirely in the Q quadrature.

The output signal has to be amplified to the level accessible to the classical readout electronics. In the ideal case, a quantum-limited phase-preserving amplifier adds half photon of noise [Cav82; Cle+10]. Together with the half photon of the vacuum noise in the coherent state, it results in a total variance $\sigma_0^2 = 1/2$ for both quadratures. The quadratures of the outgoing field can be obtained using the heterodyne detection scheme [Bla+20]. The signal is downconverted to the intermediate frequency ω_{IF} and mixed in the digitizer with an in-phase and out-of-phase reference signal of the same frequency. The quadratures of the amplified output state are integrated for the measurement time τ_{m}:

$$Q_{\mathrm{m}} = \int_{t_0}^{t_0+\tau_{\mathrm{m}}} \left(\langle\hat{Q}\rangle + \delta Q\right) dt. \tag{41}$$

Here $\langle Q\rangle$ is the quadrature expectation value according to Eq. 40, and δQ denotes the normally distributed random noise. The integrated value I_{m} is obtained in a similar way. Both the average value $\langle Q_{\mathrm{m}}\rangle = \langle\hat{Q}\rangle\tau_{\mathrm{m}}$ and the variance $\sigma_{\mathrm{m}}^2 \propto \tau_{\mathrm{m}}$ of the integrated signal grow linearly with the measurement time τ_{m}. It is convenient to rescale the integrated quadratures to the square root of the measurement photons $\sqrt{n_{\mathrm{m}}} = \sqrt{\bar{n}\kappa\tau_{\mathrm{m}}/4}$, which corresponds to the number of photons leaving the resonator during the measurement time. The scaling makes σ_{m} independent of the

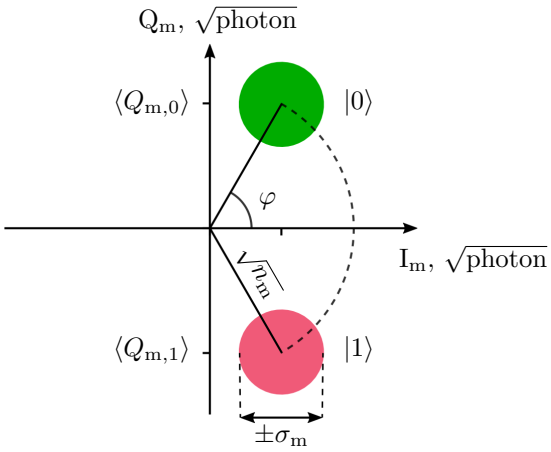

Figure 6: **IQ histogram of the integrated output signal**. Due to the dispersive shift of the resonator frequency the output coherent states acquire different phases depending on the atom state. The I and Q quadratures are rescaled to the square root of measurement photons $\sqrt{n_m} = \sqrt{\bar{n}\kappa\tau_m/4}$ [Hat+13; Voo+14]. The two disks correspond to the $|0\rangle$ and $|1\rangle$ pointer states, with identical variance $\langle(\Delta I_m)^2\rangle = \langle(\Delta Q_m)^2\rangle = \sigma_m^2$. In the case of quantum-limited noise $\sigma_m^2 = 1/2$.

integration time, and for a quantum-limited readout the quadrature variance is $\sigma_0^2 = 1/2$. The measurement efficiency of the readout amplification chain is defined as $\eta = \sigma_0^2/\sigma_m^2$ [Hat+13].

The typical dispersive measurement result is visualized in Fig. 6. The two disks in the IQ-plane represent coherent Gaussian states corresponding to the atom in $|0\rangle$ and $|1\rangle$. The separation between the states and their variance define the signal-to-noise ratio

$$\text{SNR} = \frac{|\langle Q_{m,g}\rangle - \langle Q_{m,e}\rangle|}{\sigma_{m,g} + \sigma_{m,e}} = \frac{\sqrt{n_m}}{\sigma_m}\sin(\varphi). \tag{42}$$

Here $\varphi = \arctan(\langle Q_g\rangle / \langle I_g\rangle)$ is the angle formed by the pointer states associated with the atom $|0\rangle$ state and positive real axis I_m,

$$\sin(\varphi) = \frac{2\kappa\chi_{01}}{\kappa^2 + \chi_{01}^2}. \tag{43}$$

The optimal SNR is achieved when the dispersive shift equals resonator linewidth $\chi_{01} = \kappa$, with the phase difference between the pointer states equal to 180°.

2.3 High power dispersive readout

Quantum applications require a certain threshold for the QND measurement fidelity [Bar+14]. The atom spontaneous transitions during the readout destroy the QND nature of the measurement (even if the atom-resonator interaction itself is QND), hence the upper bound on the measurement time is set by the atom relaxation. Short lifetime remains a formidable problem for superconducting qubits, naturally prone to strong coupling to the environmental degrees of freedom. Therefore in order to increase QNDness of readout it is desirable to decrease the measurement time to a fraction of the atom lifetime, while keeping the measurement signal to noise ratio constant.

As follows from eq. 42, the signal to noise ratio of the dispersive measurement scales as a square root with the number of excitations in the readout resonator and the measurement time. An obvious solution would be to increase the photon number in the readout resonator. However, until recently, measurements of superconducting qubits were performed at a moderate power of $\bar{n} = 1{-}15$ [Wal+17], with the notable exception of Andreev qubits [Hay+20; Jan+15]. The reason for the readout power limitation is the fact that increasing resonator excitation is typically accompanied by various non-QND processes, such as dressed dephasing [BGB08;

BGB09], nonlinear multimode mixing in the atom-resonator Hamiltonian [MPT20; PMT20], or transitions between resonant levels [Sli+12; San+16]. A typical signature of non-QND effects is in the degradation of the atom lifetime with increasing power observed for different types of superconducting qubits [Pic+08; Joh+12; Min+19]. So far there exists no comprehensive theory explaining the "T_1 vs. $\bar{n}$" problem. Moreover, the dominating non-QND effects can vary for different qubit implementations because they have distinct spectrum, range of nonlinearity, and coupling mechanisms to environmental defects. For example, transmon atoms can escape the bounding potential decoupling from the resonator when strong drives are applied at the resonator frequency [Les+19]. Artificial atoms with unbounded potential, such as flux qubits, are protected against such escapes.

Fluxonium circuits implemented with inductances made out of Josephson junction chains are also susceptible to non-QND effects starting from $\bar{n} \approx 2$ [Voo+14]. After replacing the Josephson junction chains with granular aluminum wires, the fluxonium turned out to acquire resilience to non-QND effects up to $\bar{n} \approx 200$ [Gus+21]. It is important to mention that the readout power corresponding to the critical photon number $n_{\mathrm{crit}} \approx 9{\cdot}10^3$ (see section 2.4) is order of magnitude larger than power used in the experiment, and atom-resonator interaction is still in the dispersive regime. Despite several spikes in transition rates at some photon numbers, there are photon number intervals where transition rates are comparable with the single-photon regime.

The fluxonium circuits made with Josephson junction arrays and granular aluminum have comparable geometry, circuit parameters, and spectrum. At a first glance, one would also expect similar behaviour at high readout power, but experiments prove the contrary. The only obvious difference between the two fluxonium implementations is the material of the inductance. Even though granular aluminum can be represented as an effective array of Josephson junctions [Mal+18], the one-to-one mapping between implementations breaks beyond the linearized model. First, intrinsic nonlinearity of granular aluminum can be engineered to be orders of magnitude lower compared to Josephson junction arrays with the same inductance. Secondly, its plasma frequency is $3-4$ times higher than that of the Josephson junction superinductors. This results in a more diluted spectrum of parasitic modes to which the atom can couple and leak its energy. These changes suppress nonlinear multimode mixing, and might explain the higher resilience of the grAl fluxonium to non-QND effects at large $\bar{n}$ when compared with Josephson junction array fluxoniums.

2.4 Fluxonium dispersively coupled to the readout resonator

Dispersive interaction of the fluxonium and the readout resonator was realized with both capacitive and inductive coupling schemes, illustrated in Fig. 7 and Fig. 8, respectively. Capacitive coupling requires resonator geometry with strong electric field gradient localized in the vicinity of the Josephson junction. This is possible, for example, with microstrip quarter-wavelength resonators [Man+09]. As an alternative, large antenna capacitance pads can be connected to the Josephson junction electrodes when coupling to the 3D readout resonator with diluted electromagnetic field [Som+21]. However, this might increase the dielectric losses in the fluxonium. Coupling to the atom charge degree of freedom results in renormalization of the atom capacitance $C' \approx C{+}C_{\mathrm{c}}$, where C is the capacitance of uncoupled atom, and C_{c} is the coupling capacitance.

Inductive dispersive coupling can be realized by sharing a part of the fluxonium loop inductance L_{s} with the readout resonator, as shown in Fig. 8 a. In comparison to capacitive coupling this scheme allows to tune the coupling strength in a wide range by changing the fraction between the shared and the fluxonium inductances. We use the inductive dispersive coupling for all the fluxonium atoms demonstrated in this manuscript.

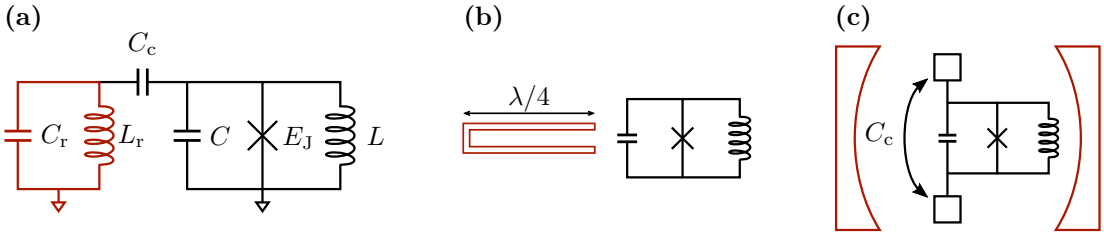

Figure 7: **Capacitive dispersive fluxonium coupling**. **(a)** Equivalent schematic of the fluxonium atom coupled capacitively to the readout resonator (shown in red). C_r and L_r are the resonator capacitance and inductance, respectively, C_c is the coupling capacitance. Fluxonium has capacitance C, Josephson energy E_J, and inductance L. **(b)** Fluxonium coupled to the microstrip quarter-wavelength resonator. To maximize the coupling strength the open end of the resonator is located in close vicinity to the Josephson junction. **(c)** Fluxonium coupling to the 3D waveguide resonator via additional antenna-like capacitance.

Circuit quantization

We derive the Hamiltonian of the inductively coupled fluxonium and the readout resonator following the superconducting circuit quantization procedure established in Ref. [Dev97]. We start from the circuit Lagrangian, and boundary conditions imposed by the fluxoid quantization rule. Then we eliminate dependent degrees of freedom using equations of motion, and make transition to the Hamiltonian with quantum operators.

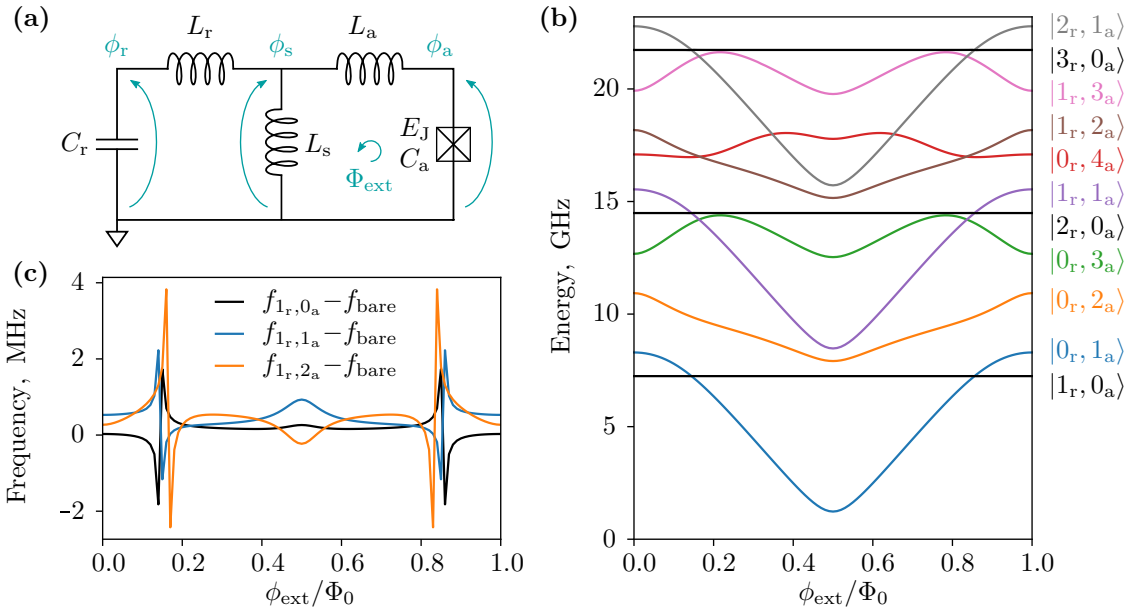

Figure 8: **Inductive dispersive fluxonium coupling**. **(a)** Equivalent schematic of the fluxonium atom coupled to the readout resonator via the shared inductance. C_r and L_r are the resonator capacitance and inductance, respectively, L_s is the coupling inductance. Fluxonium has capacitance C_a, Josephson energy E_J and inductance L_a. **(b)** Energy levels of the coupled atom-resonator system calculated by diagonalizing the Hamiltonian eq. 49. The Hamiltonian matrix is calculated in the basis of the harmonic oscillator wavefunctions for $N_r = 100$ and $N_a = 20$ excitation number in resonator and atom, respectively. Energy of the ground state $|0_r, 0_a\rangle$ is shifted to zero. The circuit parameters $C_r = 21.5\,\text{fF}$, $L_r = 22.5\,\text{nH}$, $L_s = 0.57\,\text{nH}$, $C_a = 6.9\,\text{fF}$, $L_a = 231\,\text{nH}$ and $E_J/h = 5.6\,\text{GHz}$ are the same as for the device presented in Ref. [Gus+21]. **(c)** Atom state dependent shift of the resonator frequency calculated with respect to the frequency of the uncoupled resonator $f_{bare} = 1/(2\pi\sqrt{L_r C_r}) = 7.244\,\text{GHz}$. The frequency divergence around $\phi_{ext} = 0.2\,\Phi_0$ and $\phi_{ext} = 0.8\,\Phi_0$ corresponds to level crossings (see panel b).

The fluxoid quantization in the superconducting loop formed by the atom and the shared inductances, and the Josephson junction gives

$$\phi_{L_\mathrm{a}}+\phi_\mathrm{s}-\phi_\mathrm{J}-\Phi_\mathrm{ext} = k\Phi_0. \tag{44}$$

ϕ_J is the flux across the junction, and k is an integer number, the phase across the atom inductance $\phi_{L_\mathrm{a}} = \phi_\mathrm{a}-\phi_\mathrm{s}$, the node flux variables $\phi_{\mathrm{a,s}}$ are assigned according to Fig. 8a. For simplicity of calculations we include the external field in the Josephson energy instead of the inductive energy, which is a valid substitution for the time-independent external fields as was discussed in Chapter 1.4. Then $\phi_\mathrm{J} = \phi_\mathrm{a}-\Phi_\mathrm{ext}-k\Phi_0$, and the Josephson energy equals $E_\mathrm{J}\cos(\varphi_\mathrm{a}-\varphi_\mathrm{ext})$; the term with the integer flux quantum $k\Phi_0$ cancels out because of the periodicity of the cosine function. The circuit Lagrangian

$$\mathscr{L} = \frac{C_\mathrm{r}}{2}\dot{\phi_\mathrm{r}}^2+\frac{C_\mathrm{a}}{2}\dot{\phi_\mathrm{a}}^2-\frac{1}{2L_\mathrm{r}}(\phi_\mathrm{s}-\phi_\mathrm{r})^2-\frac{1}{2L_\mathrm{a}}(\phi_\mathrm{s}-\phi_\mathrm{a})^2-\frac{1}{2L_\mathrm{s}}\phi_\mathrm{s}^2+E_\mathrm{J}\cos(\varphi_\mathrm{a}-\varphi_\mathrm{ext}). \tag{45}$$

Here C_r and C are the resonator and the atom capacitances, respectively. The resonator, fluxonium, and shared inductances are given by L_r, L_a, and L_s, respectively.

Euler-Lagrange equation of motion for ϕ_s is

$$\frac{d}{dt}\frac{\partial\mathscr{L}}{\partial\dot{\phi_\mathrm{s}}}-\frac{\partial\mathscr{L}}{\partial\phi_\mathrm{s}} = 0. \tag{46}$$

We find that ϕ_s has no dynamics because $\partial\mathscr{L}/\partial\dot{\phi_\mathrm{s}} = 0$. Therefore the number of degrees of freedom can be reduced by expressing ϕ_s via ϕ_r and ϕ_a

$$\phi_\mathrm{s} = \frac{L_\mathrm{r}L_\mathrm{a}L_\mathrm{s}}{L_\Sigma^2}\left(\frac{\phi_\mathrm{r}}{L_\mathrm{r}}+\frac{\phi_\mathrm{a}}{L_\mathrm{a}}\right), \quad L_\Sigma^2 = L_\mathrm{r}L_\mathrm{a}+L_\mathrm{r}L_\mathrm{s}+L_\mathrm{a}L_\mathrm{s} \tag{47}$$

For the Lagrangian of a system with coordinate ϕ the conjugate momentum is defined as $q = \partial\mathscr{L}/\partial\dot{\phi}$. The system Hamiltonian equals

$$H = \sum\dot{\phi}\frac{\partial\mathscr{L}}{\partial\dot{\phi}}-\mathscr{L} \tag{48}$$

Therefore the Hamiltonian of the coupled atom-resonator is:

$$H = \frac{q_\mathrm{r}^2}{2C_\mathrm{r}}+\frac{q_\mathrm{a}^2}{2C_\mathrm{a}}+\frac{L_\mathrm{a}+L_\mathrm{s}}{2L_\Sigma^2}\phi_\mathrm{r}^2+\frac{L_\mathrm{r}+L_\mathrm{s}}{2L_\Sigma^2}\phi_\mathrm{a}^2-\frac{L_\mathrm{s}}{L_\Sigma^2}\phi_\mathrm{r}\phi_\mathrm{a}-E_\mathrm{J}\cos(\varphi_\mathrm{a}-\varphi_\mathrm{ext}). \tag{49}$$

Here $q_{\mathrm{r,a}}$ and $\phi_{\mathrm{r,a}}$ are the resonator and the atom quantum flux and charge operators, respectively. The flux operator plays a role of coordinate, charge is the conjugate momentum, with commutation relation $[q,\phi] = -i\hbar$.

Hamiltonian diagonalization

Because of the high impedance of the fluxonium circuit, the phase zero point fluctuations $\varphi_\mathrm{zpf} \propto \sqrt{Z/R_\mathrm{Q}}$ are large. Therefore approximate analytical Hamiltonian solutions derived by a series expansion of the Josephson energy are not accurate. Instead we use the exact solution for the cosine matrix elements in terms of the Laguerre polynomials [Smi+16]. We calculate and diagonalize the atom-resonator Hamiltonian matrix numerically. To simulate the system behaviour at the high readout power we have to use large Hilbert space: hundreds levels for the readout resonator, and few tens levels for the atom.

The Hamiltonian matrix elements can be calculated using two different bases. The first four terms in the coupled atom-resonator Hamiltonian (eq. 49) comprise two harmonic oscillator modes: resonator-like and atom-like. The *normal mode basis* [Smi+16] is built by a linear combination of the resonator and atom flux variables which diagonalizes the harmonic part of the Hamiltonian together with the inductive coupling term

$$\begin{aligned}\phi_\mathrm{r} &= \phi_\mathrm{R}+\lambda_2\phi_\mathrm{A},\\ \phi_\mathrm{a} &= \phi_\mathrm{A}+\lambda_3\phi_\mathrm{R}.\end{aligned} \tag{50}$$

Typically, inductances scale as $L_\mathrm{a}/L_\mathrm{r} \approx L_\mathrm{r}/L_\mathrm{s} \approx 10$, and capacitances scale as $C_\mathrm{r}/C_\mathrm{a} \approx 4{-}10$, so $\lambda_2, \lambda_3 \ll 1$. In the resulting Hamiltonian the two normal modes are coupled solely via the cosine term

$$H = \frac{Q_\mathrm{R}^2}{2C_\mathrm{R}} + \frac{Q_\mathrm{A}^2}{2C_\mathrm{A}} + \frac{\phi_\mathrm{R}^2}{2L_\mathrm{R}} + \frac{\phi_\mathrm{A}^2}{2L_\mathrm{A}} - E_\mathrm{J} \cos\left(\phi_\mathrm{A} + \lambda_3 \phi_\mathrm{R} - \varphi_\mathrm{ext}\right), \tag{51}$$

here $C_\mathrm{R,A}$ and $L_\mathrm{R,A}$ are the rescaled resonator and atom capacitances and inductances, respectively. The Josephson energy contains terms with both ϕ_A and ϕ_R. Calculating cosine matrix elements with Laguerre polynomials is computationally intensive and requires truncation of the Hilbert space at $n \approx 150$ levels in the resonator mode and $i \approx 15$ levels in the atom mode.

The computational complexity is reduced if the *bare harmonic oscillator* (Fock) basis $\{\phi_\mathrm{r}, \phi_\mathrm{a}\}$ is used. The Hamiltonian unharmonic terms are given by the inductive coupling and the Josephson energy (eq. 49), but the Laguerre polynomials have to be calculated only for the phase of the atom with smaller Hilbert space compared to the resonator. This basis was used to simulate the high power readout with up to 220 photons in the readout resonator.

The diagonalized Hamiltonian matrix contains the hybridized eigenenergies $E_{|n,i\rangle}$ for n excitations in the resonator, and i excitations in the atom. Fig. 8 b shows the energy levels of the coupled atom-resonator Hamiltonian calculated for the circuit parameters of the device presented in Ref. [Gus+21]. Hybridization of the atom and the resonator levels results in the dispersive shift of the resonator frequency. Fig. 8 c shows the single photon dispersive shift calculated as difference between the atom state dependent resonator frequency and the bare resonator frequency as function of the external flux.

$$h\,\chi_i(n) = \left(E_{|n+1,i\rangle} - E_{|n,i\rangle}\right) - h\,f_\mathrm{bare}(n). \tag{52}$$

here $E_{|n,i\rangle}$ are the eigenenergies of the diagonalized Hamiltonian (eq. 49) for photon number n and atom state $|i\rangle$. The difference between the dispersive shift computed in the normal and bare basis (up to n = 150) is below 0.1%.

Coupling strength and critical photon number

In order to draw the analogy to the Rabi Hamiltonian and calculate the coupling strength (see eq. 22) we write the atom-resonator Hamiltonian in terms of raising and lowering operators of the bare harmonic oscillator modes

$$H = hf_\mathrm{r}\left(a^\dagger a + \frac{1}{2}\right) + hf_\mathrm{a}\left(b^\dagger b + \frac{1}{2}\right) - E_\mathrm{s}\left(a^\dagger + a\right)\left(b^+ + b\right) - E_\mathrm{J}\cos\left(\varphi_\mathrm{zpf}^\mathrm{a}(b^+ + b) - \varphi_\mathrm{ext}\right), \tag{53}$$

where the coupling energy $E_\mathrm{s} = (L_\mathrm{s}/L_\Sigma^2)\,\varphi_\mathrm{zpf}^\mathrm{r}\,\varphi_\mathrm{zpf}^\mathrm{a}$. In the Rabi Hamiltonian the coupling strength is given by the matrix element between the atom ground $|g\rangle$ and the first excited $|e\rangle$ states. Therefore we first have to diagonalize the Hamiltonian of the uncoupled atom to obtain the atom eigenvectors $|g\rangle$ and $|e\rangle$

$$H_\mathrm{a} = hf_\mathrm{a}\left(b^\dagger b + \frac{1}{2}\right) - E_\mathrm{J}\cos\left(\varphi_\mathrm{zpf}^\mathrm{a}(b^+ + b) - \varphi_\mathrm{ext}\right). \tag{54}$$

Then we find the matrix elements of the $(b^+ + b)$ operator for the calculated atom eigenvectors

$$\left(b^+ + b\right) = \sum_{i_\mathrm{a}} |i_\mathrm{a}\rangle\langle i_\mathrm{a}| \left(b^+ + b\right) \sum_{j_\mathrm{a}} |j_\mathrm{a}\rangle\langle j_\mathrm{a}| = \sum_{i_\mathrm{a} j_\mathrm{a}} \langle i_\mathrm{a}| \left(b^+ + b\right) |j_\mathrm{a}\rangle\, |i_\mathrm{a}\rangle\langle j_\mathrm{a}| \tag{55}$$

Here we used the fact that for a complete basis $\sum_{i_\mathrm{a}} |i_\mathrm{a}\rangle\langle i_\mathrm{a}| = 1$ is the identity operator. The coupling strength for the atom $|g\rangle$ and $|e\rangle$ states is therefore given by

$$g_\mathrm{ge} = E_\mathrm{s}\,\langle g| \left(b^+ + b\right) |e\rangle \tag{56}$$

To complete the analogy to the Rabi Hamiltonian we reduce the atom Hilbert space to the lowest two states

$$h\,E_\mathrm{s}\left(a^\dagger + a\right)\left(b^+ + b\right) = hg_\mathrm{ge}\left(a^\dagger + a\right)\Big(|g\rangle\langle e| + |e\rangle\langle g|\Big) = hg_\mathrm{ge}\left(a^\dagger + a\right)\sigma_x. \tag{57}$$

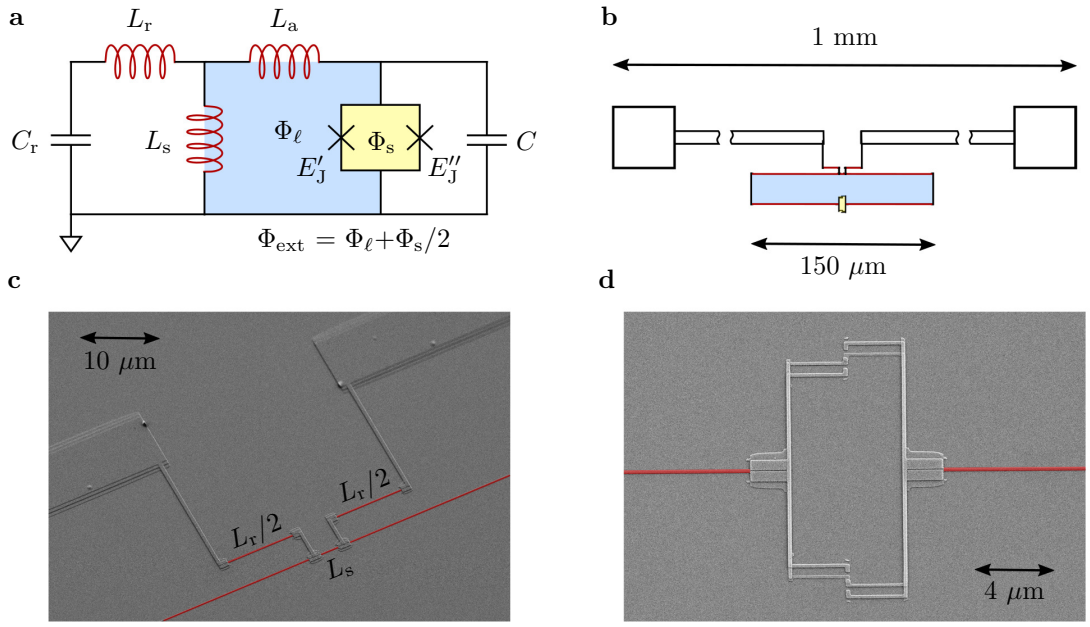

Figure 9: **Fluxonium with tunable Josephson energy**. **(a)** Equivalent atom-resonator circuit. The nonlinear element is implemented using a SQUID, the two Josephson junctions have energies E'_J and E''_J. The effective Josephson energy of the SQUID can be tuned in-situ by the magnetic flux Φ_s, from its maximum $(E'_J+E''_J)$ at $\Phi_s = 0$ to its minimum $|E'_J-E''_J|$ at the SQUID frustration $\Phi_s = \Phi_0/2$. The two loops shown in blue and yellow have areas ratio 50:1, and enclose magnetic flux Φ_ℓ and Φ_s, respectively. The big loop has area $24\times150\,\mu m^2$. **(b)** Practical implementation of the circuit. The readout resonator is made in shape of the dipole antenna. The dipole with length of 1 mm provides coupling rate $\kappa/2\pi = 1.16$ MHz to the microwave reflection readout setup. The readout resonator, atom, and shared inductances shown in red are made out of granular aluminum wires. **(c, d)** Scanning electron microscope image of the central part of the circuit, and SQUID area, respectively. The 160 nm wide granular aluminum wires used as the inductances are shown in red.

For the circuit parameters used to calculate the coupled atom-resonator energy levels (Fig. 8), at the flux bias $\Phi_{ext} = \Phi_0/2$ the coupling strength $g_{ge} \approx 31.1$ MHz, detuning between resonator and atom first transition frequency is $\Delta \approx 6$ GHz, and the critical photon number $n_{crit} = \Delta^2/(2g)^2 \approx 9{\cdot}10^3$.

However, it is important to mention that reducing fluxonium atom Hilbert space to two levels ($|g\rangle$ and $|e\rangle$) prior to calculating the coupled atom-resonator Hamiltonian does not give correct values for the dispersive shift. Using the expression for the dispersive shift in the photon-spin system $\chi = g^2/\Delta$ is also not applicable for fluxonium atoms, because virtual transitions between higher levels play an important role.

2.5 Fluxonium with tunable Josephson energy

For the high power dispersive readout we use a modified fluxonium circuit shown in Fig. 9. The only difference with the basic circuit (see. Fig. 8 a) is the Josephson junction implemented using a SQUID (two parallel Josephson junctions with energies E'_J and E''_J). The external magnetic field applied perpendicular to the plane of the circuit creates magnetic fluxes Φ_ℓ, and Φ_s through the loop formed by the inductances and the inner junction, and SQUID loop, respectively. The effective Josephson energy can be tuned in-situ

$$\begin{aligned} E_J(\varphi) &= E'_J \cos(\varphi_a - \varphi_\ell) + E''_J \cos(\varphi_a - \varphi_\ell - \varphi_s) \\ &= \mathrm{sgn}(E_{J_+}) \sqrt{E_{J_+}^2 + E_{J_-}^2}\, \cos\left(\varphi_a - \varphi_{ext} - \arctan\left(E_{J_-}/E_{J_+}\right)\right). \end{aligned} \tag{58}$$

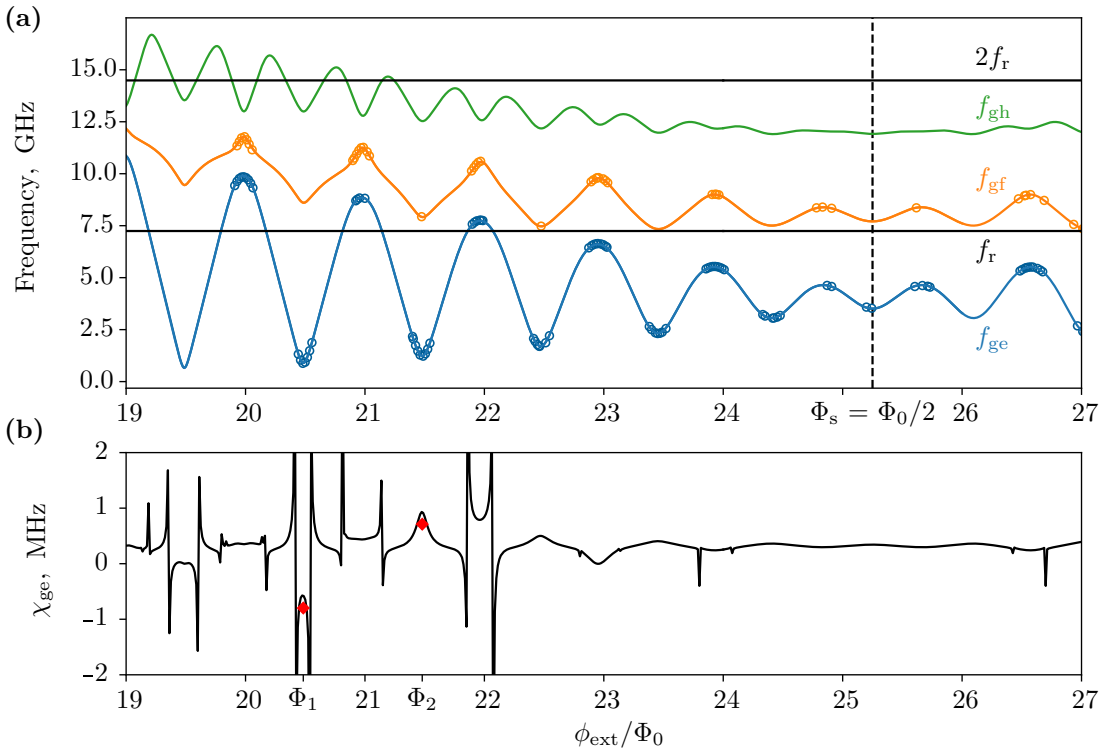

Figure 10: **Atom-resonator spectrum and the resonator dispersive shift**. **(a)**. Spectrum of the resonator (black lines) and atom transition frequencies (colored lines). Markers show measured atom $|g\rangle$−$|e\rangle$ (blue) and $|g\rangle$−$|f\rangle$ (orange) transition frequencies. Lines correspond to the numerical fit. The SQUID maximal flux frustration is indicated by the dashed vertical line. From the numerical fit we extract the atom capacitance $C_a = 6.9\,\text{fF}$, inductance $L_a = 231\,\text{nH}$ and Josephson energies $(E'_J+E''_J)/h = 24.0\,\text{GHz}$, and $|E'_J-E''_J|/h = 0.71\,\text{GHz}$. The readout resonator capacitance $C_r = 21.5\,\text{fF}$ is found from finite element circuit simulations using Ansys HFSS software (see section 5.3). The resonator inductance $L_r = 22.5\,\text{nH}$ is calculated form the bare resonator frequency $f_{r,\text{bare}} = 7.244\,\text{GHz}$ measured at zero external field. **(b)** Dispersive shift $\chi_{ge} = f_{r,e}-f_{r,g}$ of the readout resonator in the single-photon regime. The black line corresponds to χ_{ge} calculated from the coupled atom-resonator energy levels. We find the value of the shared inductance $L_s = 0.57\,\text{nH}$ by fitting the dispersive shift to measured values (red markers). The dispersive shift is comparable with the resonator linewidth $\chi_{ge} \approx \kappa$ at the two flux biases $\Phi_1 = 20.5\,\Phi_0$ and $\Phi_1 = 21.5\,\Phi_0$. Biasing the atom at these flux points optimizes the dispersive readout signal to noise ratio (see eq. 42).

Here we use the notations $E_{J_+} = (E'_J+E''_J)\cos\varphi_s$, and $E_{J_-} = (E'_J-E''_J)\sin\varphi_s$. The external field is defined as $\Phi_{ext} = \Phi_\ell+\Phi_s/2$. The effective Josephson energy is maximal at zero flux through the SQUID loop $\Phi_s = 0$ and equals $E'_J+E''_J$. The minimum effective Josephson energy $|E'_J-E''_J|$ is observed at the SQUID frustration $\Phi_s = \Phi_0/2$.

Spectrum and the dispersive shift

We perform two-tone spectroscopy to measure the transition frequencies of the fluxonium atom. This method relies on the dispersive interaction of the atom and the readout resonator. The first microwave tone is applied at the bare resonator frequency $f_{r,\text{bare}} = 7.244\,\text{GHz}$ and we record the phase response of the resonator as function of the applied magnetic field. The second tone scans frequencies in the vicinity of the expected atomic transition. This tone saturates the atomic transition on resonance which results in a shift of the resonator frequency. The change in the phase of the output signal indicates that the probe tone crossed the atomic transition frequency (we did not observe crossings with spurious systems coupled to the readout resonator). Fig. 10 a demonstrates the measured $|g\rangle$−$|e\rangle$ and $|g\rangle$−$|f\rangle$ transition frequencies (markers) and

the numerical fit of the spectrum (lines).

We fit the measured spectrum with calculated eigenenergies of the uncoupled fluxonium atom to extract the atom capacitance, inductance, and Josephson energies. A numerical fit of the data with full atom-resonator Hamiltonian is cost intensive, and the gain in precision is small. The error between energy levels calculated for coupled and uncoupled fluxonium away from crossings with the resonator (where frequency diverges) is $\lesssim 70\,\mathrm{kHz}$. The bare readout resonator frequency $f_{\mathrm{r,bare}} = 7.244\,\mathrm{GHz}$ is measured by a single tone spectroscopy at zero external field where the resonator is decoupled from the atom, and dispersive shift is negligible compared to the resonator frequency ($\chi_{\mathrm{ge}}(\Phi_{\mathrm{ext}} = 0) = 1.7\,\mathrm{kHz}$). The resonator frequency and coupling rate $\kappa/2\pi = 1.16\,\mathrm{MHz}$ are obtained with the circle fit of the complex refection coefficient (see section 5.4.1).

The dispersive shift of the readout resonator $\chi_{\mathrm{ge}} = f_{\mathrm{r,e}} - f_{\mathrm{r,g}}$ as function of external field is shown in Fig. 10 b. The two red markers indicate the measured values at the single-photon regime. We calculate the dispersive shift by fitting the data with coupled atom-resonator Hamiltonian with one fitting parameter, shared inductance. Other circuit parameters are found from the single and two-tone spectroscopy. In general case the photon number dependent shift $\chi_{\mathrm{ge}}(n)$ is defined as difference between resonator transition frequencies when atom is in ground and excited states [Smi+16]:

$$h\,\chi_{\mathrm{ge}}(n) = \left(E_{|n+1,\mathrm{e}\rangle} - E_{|n,\mathrm{e}\rangle}\right) - \left(E_{|n+1,\mathrm{g}\rangle} - E_{|n,\mathrm{g}\rangle}\right), \tag{59}$$

where $E_{|n,\mathrm{i}\rangle}$ are the energy levels for states with n photons in the resonator and atom state $|i\rangle$. The dispersive shift can take both negative and positive values, as shown in Fig. 10 b for Φ_1 and Φ_2, respectively. These flux bias points are optimal for the dispersive readout, because the dispersive shift is comparable with the resonator linewidth, as required to maximize the signal to noise ratio (see eq. 42). All the following high power measurements were performed at these bias points.

2.5.1 High power dispersive QND readout

In this section we demonstrate the high power dispersive fluxonium readout. We start from the photon number calibration and the resonator nonlinearity which leads to the bifurcation of the resonator and limits the readout power used for the linear dispersive readout. We measure the dispersive shift as function of the photon number, and demonstrate the reduction of the measurement time required to obtain a fixed signal to noise ratio. We characterize the QNDness of the high power dispersive readout by measuring the transition rates between the atom ground and excited states, and by state preparation fidelity. We also calculate the dipole matrix elements and the Purcell decay rate of the fluxonium atom. Note that parts of this section were already published in Ref. [Gus+21].

Photon number calibration

The photon number inside the readout resonator can be estimated using the input-output relations for the resonator measured in reflection. For the resonator driven on resonance the input power P and photon number in the steady state $\bar{n}$ are related with the equation (see section 2.1)

$$P = \hbar\omega\frac{\kappa}{4}\bar{n}, \tag{60}$$

here κ is the resonator coupling rate. The power sent by the generator is reduced by $\approx 90\,\mathrm{dB}$ by commercial attenuators and resistive coaxial cables inside the cryostat to suppress the thermal noise fed into the sample. However, precise value of the total attenuation with contributions from cables, filters, and connectors is unknown. Therefore eq. 60 can be used only for rough estimation of the photon number.

Another way to calibrate the photon number is based on the dispersive interaction between the atom and the resonator. The hybridization of states leads to the atom state dependent resonator

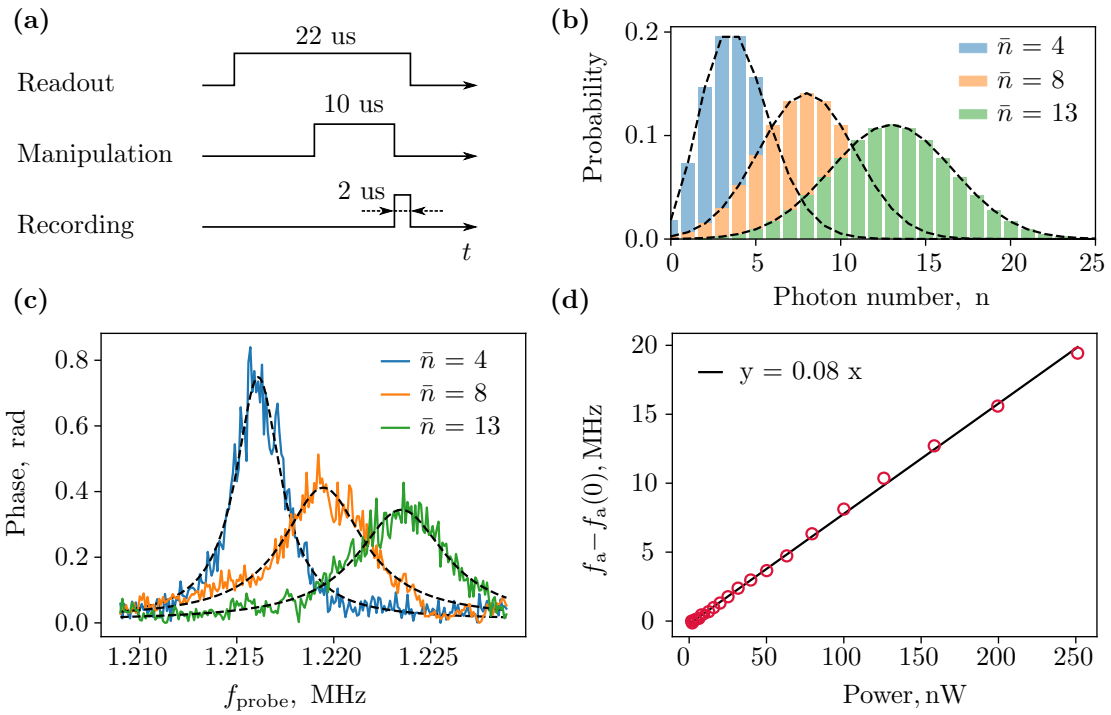

Figure 11: **Photon number calibration with the ac Stark shift of the atom frequency**. **(a)** Pulse sequence used for measurement of the ac Stark shift. Pulse at the readout resonator frequency populates resonator with $\bar{n}$ photons in the steady coherent state. The manipulation pulse is sent at the probe frequency around the atomic transition. The readout resonator response is integrated during the recording time and averaged for 2000 repeated pulse sequences. **(b)** Poisson distribution of the photon numbers in the coherent states with different $\bar{n}$. **(c)** Recorded phase response of the readout resonator as function of manipulation frequency. Colored lines correspond to the measured data, while black lines indicate the Lorentzian fit. The manipulation pulse saturates the atom $|g\rangle$-$|e\rangle$ transition on resonance. **(d)** Extracted ac Stark shift of the atom transition frequency as function of the fridge input power (red markers) measured at $\Phi_{\mathrm{ext}} = \Phi_2$. Black line is the linear fit. The extracted coefficient was used to calibrate the photon number inside the readout resonator (see eq.62).

frequency. Likewise, the atom frequency acquires the so-called ac Stark shift dependent on the photon number

$$f_{\mathrm{a}}(\bar{n}) = f_{\mathrm{a}}(0) + \chi_{\mathrm{ge}}\bar{n}. \tag{61}$$

Then the photon number can be calculated from the slope of the atom frequency dependence on the input power

$$\frac{d\bar{n}}{dP} = \frac{1}{\chi_{\mathrm{ge}}}\frac{df_{\mathrm{a}}}{dP}. \tag{62}$$

We use the time domain setup to measure the ac Stark shift of the atom frequency. The pulse sequence is shown in Fig. 11 a. We apply a readout pulse at the resonator frequency with duration much longer than the resonator response time $2/\kappa \approx 280\,\mathrm{ns}$. This ensures that the resonator evolves into a steady coherent state. After 10 µs we apply the manipulation pulse at the probe frequency around the atom transition. When the manipulation pulse is detuned from the atomic transition the readout resonator frequency corresponds to the equilibrium excitation of the atom $f_{\mathrm{r}} = P_{\mathrm{g}} f_{\mathrm{r,g}} + P_{\mathrm{e}} f_{\mathrm{r,e}}$, where P_{g} and P_{e} are the probabilities to find the atom in $|g\rangle$ and $|e\rangle$ states, respectively. The manipulation pulse is order of magnitude longer than the atom coherence time and it saturates the atom to the incoherent 50 % population, and the resonator frequency shifts to $(f_{\mathrm{r,g}} + f_{\mathrm{r,e}})/2$. The resonator state is recorded immedeately after the saturation pulse.

The output resonator phase response as function of the probe frequency reveals the shape of the atom line. Populating resonator with higher photon numbers causes measurement-induced dephasing [Gam+06], which is reflected in the broadening of the atom linewidth. The

probability distribution of photons in the coherent state is Poissonian

$$P(n) = \frac{\bar{n}^n \exp^{-\bar{n}}}{n!}. \tag{63}$$

The standard deviation increases with the photon number as $\sqrt{\bar{n}}$ (see Fig. 11 b). The atom frequency can be extracted with data fit to Lorentzian lineshape at low power, and by Gaussian fit at high power.

We fix the signal generator output power and sweep power at the cryostat input by the step attenuator with 1 dB increment. The initial power at the cryostat input was measured with the spectrum analyser. The measured phase response of the resonator at different input power is demonstrated in Fig. 11 c. We fit the extracted atom frequency with linear function to find the conversion coefficient from the input power to photon numbers $\bar{n}/P = 0.11/\mathrm{nW}$ for power measured in nW. The photon number was calibrated with the ac Stark shift of the fluxonium frequency for $\bar{n} < 15$, and extrapolated linearly for higher readout power values. The calculated photon numbers are consistent with estimation obtained with eq. 60.

Another method of calibrating the photon number by the measurement-induced dephasing of the atom in a time-domain experiment [Bul+18] was not possible for our fluxonium, because the integration time (when not using a parametric amplifier) was comparable with the atom decoherence time (see section 2.5.4).

Readout resonator nonlinearity

The total nonlinearity of the readout resonator has two contributions: intrinsic nonlinearity K_{11} and inherited anharmonicity α. In our fluxonium implementation the intrinsic nonlinearity is associated with the self-Kerr of the granular aluminum. The inherited anharmonicity is due to hybridization with the atom levels. The total nonlinearity imposes a limit on the readout power: the linear dispersive regime breaks at the photon number corresponding to bifurcation of the readout resonator.

Response of the nonlinear resonator measured in reflection is described by the input-output relations [EW14]:

$$\begin{aligned} \dot{a}(t) &= -i\omega_{\mathrm{r0}} a - iK_{11} a^\dagger a a - \frac{\kappa}{2} a + \sqrt{\kappa}\, b_{\mathrm{in}}(t) \\ b_{\mathrm{out}}(t) - b_{\mathrm{in}}(t) &= \sqrt{\kappa} a(t) \end{aligned} \tag{64}$$

here ω_{r0} is the bare resonator frequency, K_{11} is the self-Kerr coefficient; a, b_{in}, and b_{out} are the amplitudes of the field inside the resonator, input, and output fields, respectively. The amplitude of the input field has units of $\sqrt{\mathrm{Hz}}$, and is related to the input power at the drive frequency $|b_{\mathrm{in}}| = \sqrt{P_{\mathrm{in}}/\hbar\omega_{\mathrm{d}}}$. The steady state solution for the resonator field $\dot{a}(t) = 0$ satisfies the equation

$$\left(\delta^2 + \frac{1}{4}\right) n - 2\delta\xi n^2 + \xi^2 n^3 = \frac{|b_{\mathrm{in}}|^2}{\kappa} \tag{65}$$

where $n = |a|^2$ is the photon number inside the resonator, δ and χ are values of the drive detuning and resonator nonlinearity normalized to the resonator energy decay rate κ

$$\delta = \frac{\omega_{\mathrm{d}} - \omega_{\mathrm{r0}}}{\kappa}, \quad \xi = \frac{K_{11}}{\kappa} \tag{66}$$

Equation (65) is cubic in respect to the photon number n. The derivative $\mathrm{d}n/\mathrm{d}\delta = \infty$ at the critical value $\xi_{\mathrm{crit}} = -(\sqrt{27}\,|b_{\mathrm{in}}|^2/\kappa)^{-1}$, which corresponds to onset of the bifurcation regime. The photon number at which bifurcation starts

$$n_{\mathrm{max}} = \frac{\kappa}{\sqrt{3} K_{11}}. \tag{67}$$

The nonlinear resonator phase response as function of the drive frequency can be calculated from the complex reflection coefficient $\varphi(\omega_{\mathrm{d}}) = \arg(S_{11})$. The reflection coefficient is defined as

$$S_{11} = \frac{b_{\mathrm{out}}}{b_{\mathrm{in}}} = \frac{1}{0.5 - i\delta + i\xi n} - 1. \tag{68}$$

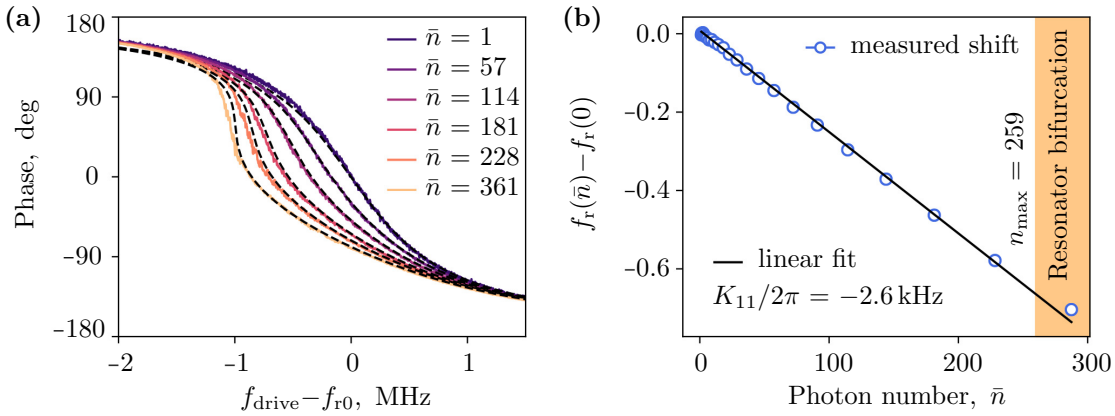

Figure 12: **Intrinsic nonlinearity of the readout resonator**. **(a)**. Phase response of the readout resonator measured at different photon numbers (colored lines). The atom is biased at zero magnetic field where resonator inherited anharmonicity is negligible. Dashed black lines indicate the expected phase response calculated using input-output relations for the nonlinear resonator (see eq. 65, 68) for the extracted value of the self-Kerr coefficient $K_{11}/2\pi = -2.6\,\mathrm{kHz}$. **(b)** The Kerr shift of the resonator frequency vs $\bar{n}$ (markers) obtained from the circle fit of the measured resonator reflection coefficient. Black line is a linear fit. The orange interval corresponds to the bifurcation of the resonator which starts at $n_{\mathrm{max}} = 259$.

Intrinsic nonlinearity

We measure the intrinsic self-Kerr coefficient K_{11} of the resonator by the single tone spectroscopy at variable input power. The atom is biased at the zero magnetic field where resonator is decoupled from the atom, and the inherited nonlinearity is negligible ($\sim 10^{-2}\,\mathrm{Hz}$). Fig. 12 a shows the measured phase response of the readout resonator as function of the detuning between drive frequency and bare resonator frequency f_{r0}. We extract the resonator frequency $f_{\mathrm{r}}(\bar{n})$ with the circle fit of the complex reflection coefficient. The frequency shift as function of the photon number

$$f_{\mathrm{r}}(\bar{n}) - f_{\mathrm{r0}} = -K_{11}\,\bar{n}. \tag{69}$$

The measured frequency shift is demonstrated in Fig. 12 b.

From the linear fit of the data we obtain the self-Kerr coefficient $K_{11}/2\pi = -2.6\,\mathrm{kHz}$. This value was used to calculate the expected resonator phase response, shown in black dashed lines in Fig. 12 a. The small discrepancy between the calculated and measured phase at high photon numbers can be explained by the error in photon number calibration caused by the dependence of the dispersive shift on the readout power. The calculated photon number at which the resonator bifurcates $n_{\mathrm{max}} = 259$ (see eq. 67).

Inherited anharmonicity

Dispersive interaction of the fluxonium atom and the readout resonator leads to hybridization of their states, and the resonator acquires anharmonicity, which we call *inherited*. We define the resonator anharmonicity $\alpha_{|i\rangle}(n)$ for the fluxonium in state $|i\rangle$ as difference between resonator transition frequencies for $n{+}1$ and n photons in the resonator

$$h\,\alpha_{|i\rangle}(n) = \left(E_{|n+1,i\rangle} - E_{|n,i\rangle}\right) - \left(E_{|n,i\rangle} - E_{|n-1,i\rangle}\right), \tag{70}$$

where $E_{|n,i\rangle}$ are the energies of the coupled fluxonium-resonator Hamiltonian, and atom states $i = \{g, e\}$. In Fig. 13 a,b we show the inherited anharmonicity calculated as function of the external magnetic field in the vicinity of $\Phi_{\mathrm{ext}} = \Phi_1$ and $\Phi_{\mathrm{ext}} = \Phi_2$ for $n = 1$. The resonator anharmonicity for the fluxonium in the ground state (dashed lines) is in range of few Hz, and the total nonlinearity of the resonator is dominated by the self-Kerr of the granular aluminum. In contrast, the resonator anharmonicity for the fluxonium in the excited state (solid lines) is in range of the intrinsic nonlinearity (see section 2.5.1).

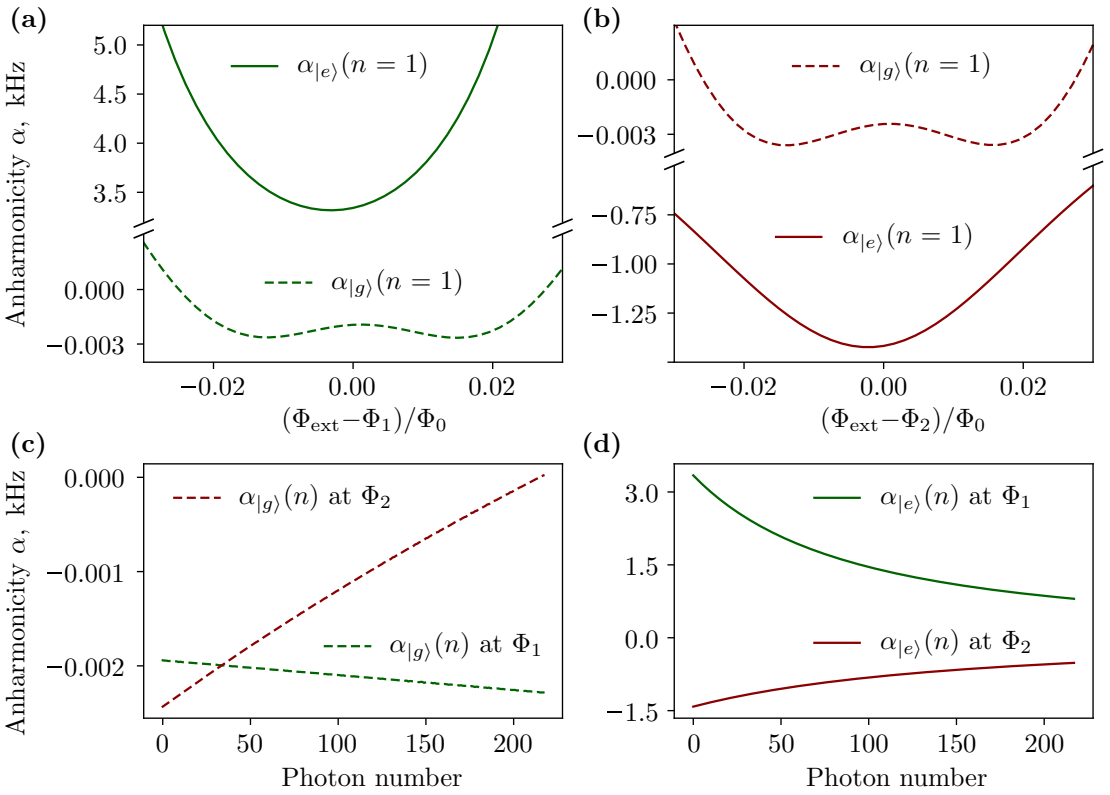

Figure 13: **Inherited anharmonicity of the readout resonator**. **(a, b)**. Anharmonicity of the resonator calculated numerically in the vicinity of $\Phi_{\text{ext}} = \Phi_1$ (green lines) and $\Phi_{\text{ext}} = \Phi_2$ (bordeaux lines) from the eigenenergies of the coupled fluxonium-resonator Hamiltonian for $n = 1$. The inherited anharmonicity is fluxonium state dependent: for the $|g\rangle$ state (dashed lines) it is negative at both flux points Φ_1 and Φ_2. Anharmonicity for the $|e\rangle$ state (solid lines) has different signs at Φ_1 and Φ_2, and is orders of magnitude stronger, than for the $|g\rangle$ state. **(c, d)** Inherited anharmonicity as function of the photon number in the resonator. The left panel corresponds to $\alpha_{|g\rangle}(n)$ while right panel shows $\alpha_{|e\rangle}(n)$. Note that the absolute value of $\alpha_{|e\rangle}$ decreases with $\bar{n}$.

Depending on the flux bias and relative position of the atom-resonator levels the inherited anharmonicity can take values of different sign. The anharmonicity also depends on the photon number in the readout resonator. The calculated $\alpha_{|\text{g,e}\rangle}(n)$ is shown in Fig. 13 c,d. For the atom in the excited state the absolute value of the anharmonicity decreases monotonously with $\bar{n}$. At the Φ_1 flux point the inherited anharmonicity compensates the intrinsic nonlinearity $K_{11}/2\pi = -2.6\,\text{kHz}$ at low photon numbers, and the total nonlinearity is positive up to $\bar{n} \approx 25$. We perform the high power fluxonium measurements for photon numbers up to the onset of bifurcation for either $|g\rangle$ or $|e\rangle$ states. The observed maximal photon number $n_{\text{max}} = \min(n_{\text{max,g}}, n_{\text{max,e}}) \approx 200$ for both Φ_1 and Φ_2.

Dispersive shift as function of the photon number

We extract the dispersive shift $\chi_{\text{ge}} = f_{\text{r,e}} - f_{\text{r,g}}$ from the phase separation of the coherent state clouds in the IQ plane (see Section 2.2). The clouds are obtained by recording the signal reflected from the readout resonator. For QND readout the signal integration time should be shorter than the atom energy relaxation time. Therefore we use the time domain setup to shape the readout tone and collect the data. We send the microwave readout tone at the drive frequency f_{drive} in the continuous wave regime, with the tone duration of 4 millisecond, much longer than the resonator response time $2/\kappa \approx 280\,\text{ns}$. The output signal is integrated for the time required to obtain the SNR = 3 for resolving the $|g\rangle$ and $|e\rangle$ atom states, corresponding to the single-shot state discrimination fidelity of 99.7%.

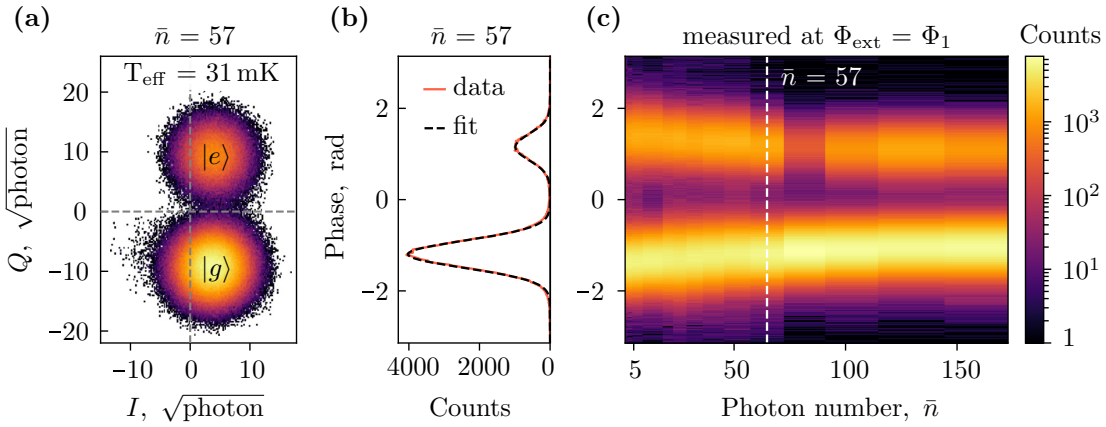

Figure 14: **Phase separation of the $|g\rangle$ and $|e\rangle$ pointer states in the IQ plane used to extract the dispersive shift as function of $\bar{n}$. (a)**. Measured IQ histogram for fluxonium biased at $\Phi_{ext} = \Phi_1$ for $\bar{n} = 57$ and integration time $\tau_m = 944$ ns. Color indicates the number of counts. The quadratures are rescaled to the square root of the measurement photons $\sqrt{n_m} = \sqrt{\bar{n}\kappa\tau_m/4}$. The two Gaussian clouds correspond to the steady states with atom in $|g\rangle$ and $|e\rangle$. The atom effective temperature extracted from the measured $|e\rangle$ state population corresponds to the mixing chamber temperature of the dilution refrigerator. **(b)** Phase distribution histogram for the measured IQ points at $\bar{n} = 57$ (red). Black line shows the data fit with double Gaussian function. **(c)** Phase histograms measured for different photon numbers $\bar{n}$. At each photon number the readout frequency was adjusted to give the maximal phase separation of the pointer states. The measurement time is chosen to give the fixed SNR = 3 (see eq. 42). All measurements are done without the use of a parametric amplifier.

Figure 14 a shows an example of the measured IQ clouds for $\bar{n} = 57$ photons in the resonator. Fluxonium is biased at $\Phi_{ext} = \Phi_1$. The histogram contains $\approx 2{\cdot}10^5$ points collected over several minutes (the 4 millisecond traces are separated by the time required to process and save the data). The color code indicates the number of counts. The IQ clouds are rotated such that information about the atom state is encoded in the Q-quadrature, and the quadratures are rescaled to the square root of the measurement photons $\sqrt{n_m} = \sqrt{\bar{n}\kappa\tau_m/4}$. The integration time $\tau_m = 944$ ns. We fit the data by a double Gaussian function to obtain the position of the pointer states and excitation of the atom. The measured excited state population $P_e = 20.4\%$. The corresponding effective temperature of the atom $T_{eff} = 31.1$ mK calculated from the Boltzmann distribution (eq. 93) is consistent with the temperature expected in the thermal equilibrium with the mixing chamber of the dilution refrigerator. The atom first transition frequency $f_{ge}(\bar{n} = 57) \approx 0.88$ GHz. Fig. 14 b shows the phase histogram for the data shown in the panel a.

We measure the IQ clouds for increasing input power up to the bifurcation of the readout resonator. The corresponding phase histograms are plotted in Fig. 14 c, the color corresponds to the number of counts. The integration time was adjusted at each $\bar{n}$ to give fixed SNR = 3 calculated for the Q-quadrature of the output signal (see eq. 42). The total number of counts for all $\bar{n}$ was limited by the same value $\approx 2{\cdot}10^5$. Therefore the color change between the histograms with different $\bar{n}$ indicates that the atom excitation depends on the photon number. The minimum excited state population $P_e = 4.1\%$ was observed at $\bar{n} \approx 72$, and corresponds to $T_{eff} = 13.3$ mK which is smaller than the fridge temperature $T_{MXC} = 31 \pm 3$ mK.

We map the measured phase difference between the states to the dispersive shift by calculating the expected phase response of the readout resonator taking into account both intrinsic and inherited nonlinearity (see Section 2.5.1). The phase separation of the pointer states also depends on the drive frequency. At each photon number the drive frequency f_{drive} was selected such that it gives the maximal phase separation of the $|g\rangle$ and $|e\rangle$ pointer states in the IQ plane. The examples of the phase response and the extracted dispersive shift for the single-photon and the high power readout are illustrated in Fig. 15.

Fig. 16 shows the extracted dispersive shift $\chi_{ge}(\bar{n})$ measured at $\Phi_{ext} = \Phi_1$ and $\Phi_{ext} = \Phi_2$ as function of the photon number (markers). The orange interval corresponds to the observed onset

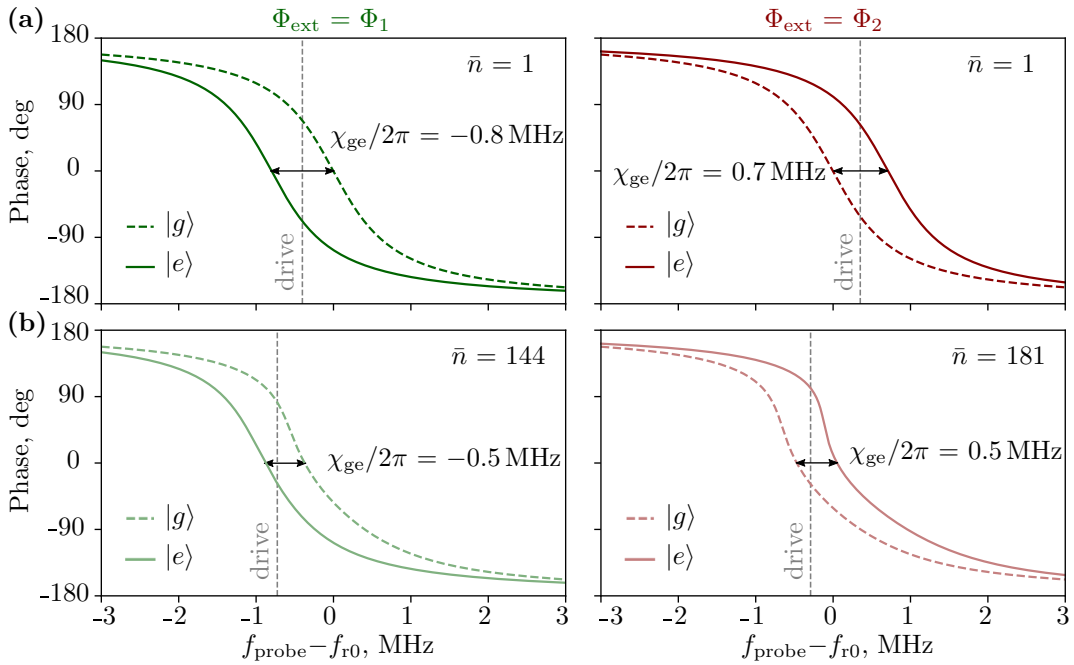

Figure 15: **Phase response of the readout resonator used to extract the dispersive shift.** The phase response as a function of detuning from the bare frequency $f_{r0} = 7.244\,\mathrm{GHz}$ was calculated using input-output theory for the nonlinear resonator (see section 2.5.1) taking into account both the intrinsic nonlinearity and inherited anharmonicity of the resonator. The left and right columns of the figure correspond to the fluxonium bias points $\Phi_{ext} = \Phi_1$ and $\Phi_{ext} = \Phi_2$, respectively. **(a)** Phase response in the single-photon regime. The dashed and solid lines correspond to the fluxonium in the $|g\rangle$ and $|e\rangle$ states, respectively. We match the maximal phase separation between the curves for $|g\rangle$ and $|e\rangle$ states to the measured phase between the IQ plane pointer states. The dashed grey lines show the readout drive frequency. The phase separation was converted to a frequency shift using numerical inversion of the calculated resonator phase response. **(b)** Phase response at the highest photon number used in experiments, $\bar{n} = 144$ at $\Phi_{ext} = \Phi_1$ and $\bar{n} = 181$ at $\Phi_{ext} = \Phi_2$.

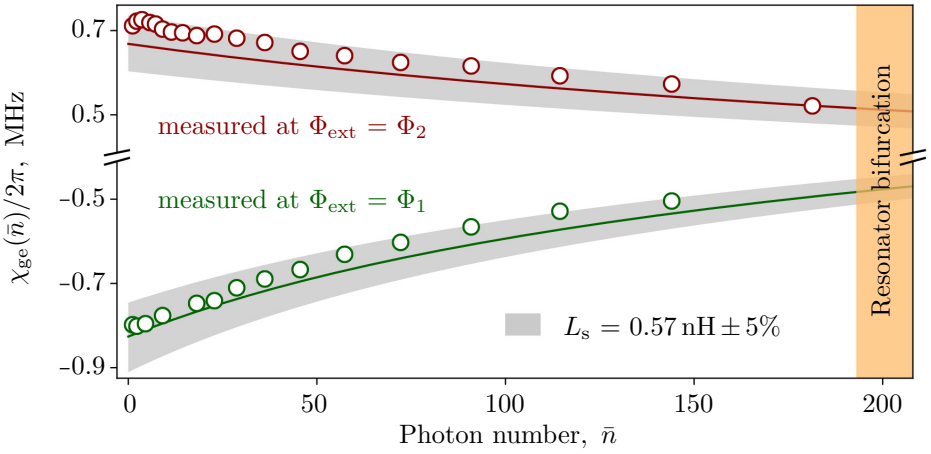

Figure 16: **Dispersive shift as function of photon number**. Markers show the measured $\chi_{ge}(n)$ at Φ_1 (green) and Φ_2 (bordeaux). Lines correspond to the $\chi_{ge}(n)$ calculated from the eigenenergies of the coupled fluxonium-resonator Hamiltonian (see eq. 59) for the value of the shared inductance $L_s = 0.57\,\mathrm{nH}$. All other circuit parameters were extracted from the single and two-tone spectroscopy of the resonator and atom, respectively. The grey-shaded intervals represent $L_s \pm 5\%$. The orange shaded interval indicates the observed onset of the resonator bifurcation.

of the resonator bifurcation regime. The solid lines show the dispersive shift calculated from the eigenenergies of the fluxonium-resonator Hamiltonian for the value of the shared inductance $L_s = 0.57\,\mathrm{nH}$ (see eq. 59). The grey shaded intervals correspond to $L_s = 0.57\,\mathrm{nH}\pm5\%$. The dispersive shift is negative at $\Phi_{ext} = \Phi_1$, and positive at $\Phi_{ext} = \Phi_2$. Importantly, the absolute value of the dispersive shift decreases with the photon number.

Fluxonium transition rates

We characterize the QNDness of the continuous high power dispersive readout by measuring the dependence of the fluxonium transition rates between the $|g\rangle$ and $|e\rangle$ states on the photon number inside the resonator. We apply a continuous wave drive which populates the readout resonator with $\bar{n}$ photons, and record the IQ-quadratures of the output signal. The IQ plane was rotated such that the signal is entirely contained in the Q quadrature. Fig. 17 a shows a cut of the Q-quadrature time trace measured at $\Phi_{ext} = \Phi_1$ with $\bar{n} = 91$. The blue line corresponds to the measured data, each point of the trace was obtained with the integration time of $\tau_m = 624\,\mathrm{ns}$ without the use of a parametric amplifier. The corresponding IQ histogram is shown in Fig. 17 b.

The IQ histogram allows to distinguish two atom states. We fit the histogram with double Gaussian function and extract the position of the pointer states and the standard deviation σ of the distributions. We use a two-point latching filter to detect the fluxonium quantum jumps. We assign the atom state $|g\rangle$ or $|e\rangle$ to the points within $\pm2.5\,\sigma$ intervals around the centers of the corresponding distributions. The jump is detected if the next measured point is within a $\pm2.5\sigma$ region centered on the other state. The output of the latching filter is shown in black.

We use the collected statistics of the time intervals spent in each fluxonium state to calculate the atom transition rates. Fig. 18 demonstrates the extracted histograms of the fluxonium quantum jumps. The top and bottom panels correspond to fluxonium $|g\rangle$ and $|e\rangle$ states, respectively. The probability of the time intervals should obey a Poissonian statistics for the uncorrelated quantum jumps $p(\tau) = \Gamma e^{-\Gamma\tau}$ with transition rate Γ equal to the inverse mean time $\bar{\tau}$. We fit the histograms with an exponential function to find the transition rates (black lines). The calculated $\Gamma_\uparrow$ is the fluxonium excitation rate, while $\Gamma_\downarrow$ is the relaxation rate. At some photon numbers histograms deviate from the Poisson statistics as demonstrated in the right column of

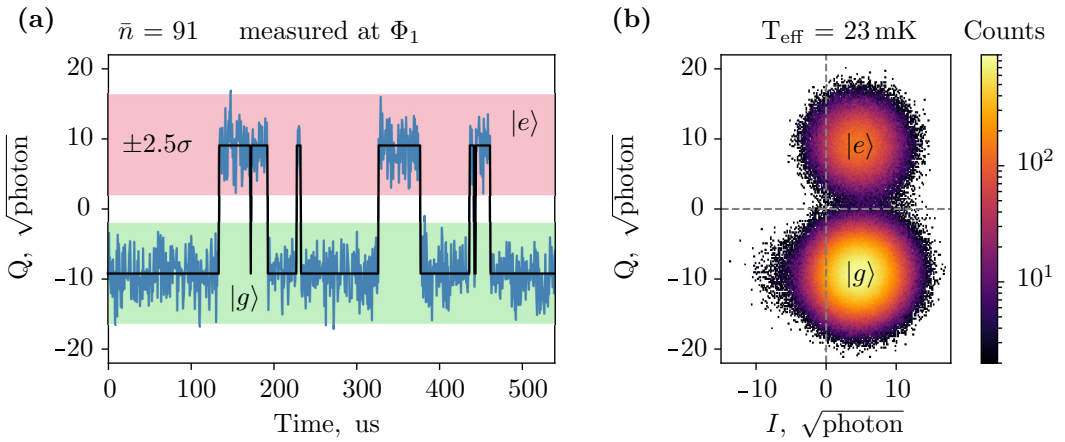

Figure 17: **Continuous wave atom state measurement**. **(a)** A cut of the time trace of the Q-quadrature resonator response measured for $\bar{n} \approx 91$ circulating photons at $\Phi_{ext} = \Phi_1$. We measure the resonator response (blue lines) without the use of a parametric amplifier. Each point of the trace was obtained by integrating resonator output signal for $\tau_m = 624\,\mathrm{ns}$. The measurement displays spontaneous quantum jumps of the fluxonium between the ground, $|g\rangle$, and excited state, $|e\rangle$. Shaded green and pink intervals show a $\pm2.5\,\sigma$ deviation from the centers of the corresponding distributions. The signal to noise ratio SNR = 3. The black lines indicate the atom state estimation based on a two-point latching filter. **(b)** The corresponding IQ histogram, color indicates the number of counts.

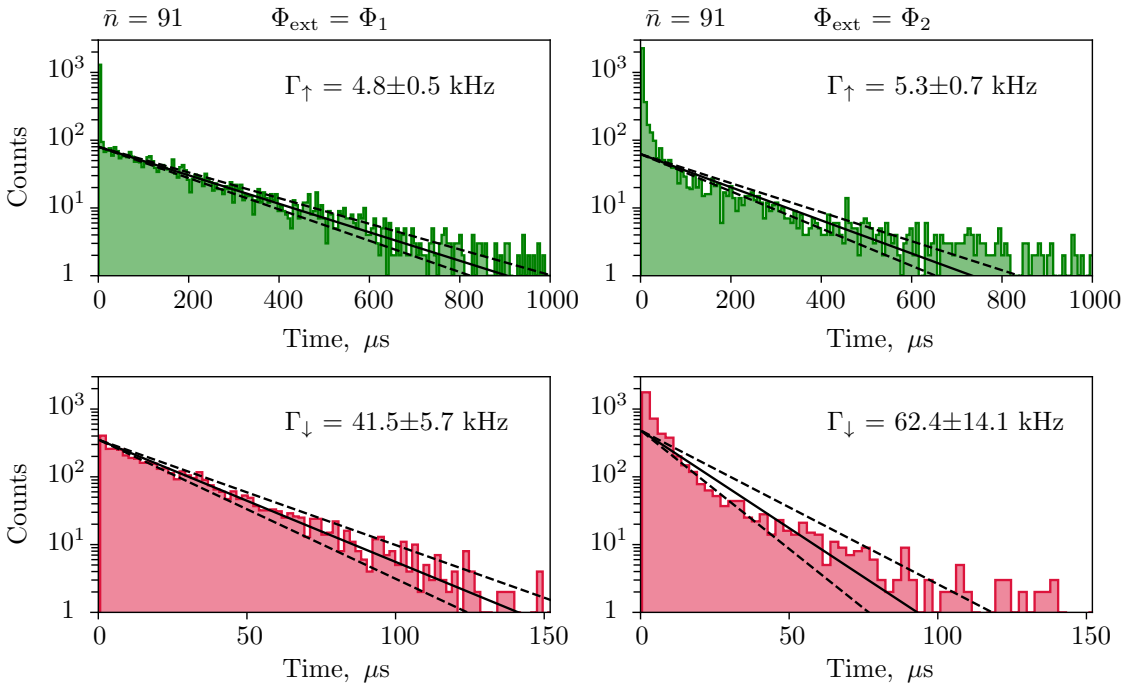

Figure 18: **Histograms of the fluxonium quantum jumps measured at $\bar{n} = 91$.** The left and right columns of the figure correspond to the flux biases $\Phi_{\text{ext}} = \Phi_1$ and $\Phi_{\text{ext}} = \Phi_2$, respectively. Histograms in green and pink correspond to fluxonium measured in the $|g\rangle$ and $|e\rangle$ states, respectively. We fit the histograms with exponential function to extract the fluxonium excitation rate $\Gamma_\uparrow$ (from $|g\rangle$ to $|e\rangle$) and relaxation rate $\Gamma_\downarrow$ (from $|e\rangle$ to $|g\rangle$). The solid black lines show the exponential fit to the measured data, and the dashed black lines indicate the standard deviation of the extracted transition rates $\Gamma_\uparrow$ and $\Gamma_\downarrow$. Distributions can deviate form the exponential decay which implies a presence of the correlated quantum jumps, similarly to the results reported in Ref. [Voo+14] for the fluxonium with Josephson junction array inductance.

Fig. 18. Usually, the deviation is stronger for $|g\rangle$ state, and distributions have excess number of the short jumps. Non-Poissonian jumps were previously observed in the fluxonium made with Josephson junction chains [Voo+14]. Most probably, they are related to the non-equilibrium quasiparticles.

In the same way we measure the atom transition rates for increasing photon number in the readout resonator. At each photon number the IQ output signal was recorded during few minutes, and the integration time was adjusted to obtain fixed SNR = 3. The extracted transition rates as functions of $\bar{n}$ for $\Phi_{\text{ext}} = \Phi_1$ and $\Phi_{\text{ext}} = \Phi_2$ are shown in Fig. 19 a. Green and crimson markers correspond to $\Gamma_\downarrow$ and $\Gamma_\uparrow$, respectively. The shaded pink interval in the left panel corresponds to results obtained using the dimer Josephson junction array (DJJAA) parametric amplifier [Win+20a] at $\Phi_{\text{ext}} = \Phi_1$ for $\bar{n} < 10$. Otherwise it was impossible to achieve the SNR = 3 because the integration time without a parametric amplifier was too long compared to the energy relaxation time.

The blue line shows the fluxonium free decay rate from the excited state measured in absence of the resonator excitation during the fluxonium evolution. As expected, the free decay rate does not depend on the readout power, and it serves as a reference value for the rates measured while resonator is populated with $\bar{n}$. The decay rate from the fluxonium excited state in presence of resonator drive $\Gamma_{\text{total}} = \Gamma_\uparrow + \Gamma_\downarrow$ is dominated by the relaxation rate $\Gamma_\downarrow$. Typically the decay rate of the superconducting qubits increases with $\bar{n}$ due to emerging non-QND effects, and we expect that Γ_{total} should be higher than the free decay rate, which is the case for the $\Phi_{\text{ext}} = \Phi_2$ flux bias point. Surprisingly, at the $\Phi_{\text{ext}} = \Phi_1$ flux bias Γ_{total} is lower than the free decay rate for photon numbers smaller than 60. The observed reduction of the transition rates during the measurement resembles the quantum Zeno effect [Sli+16].

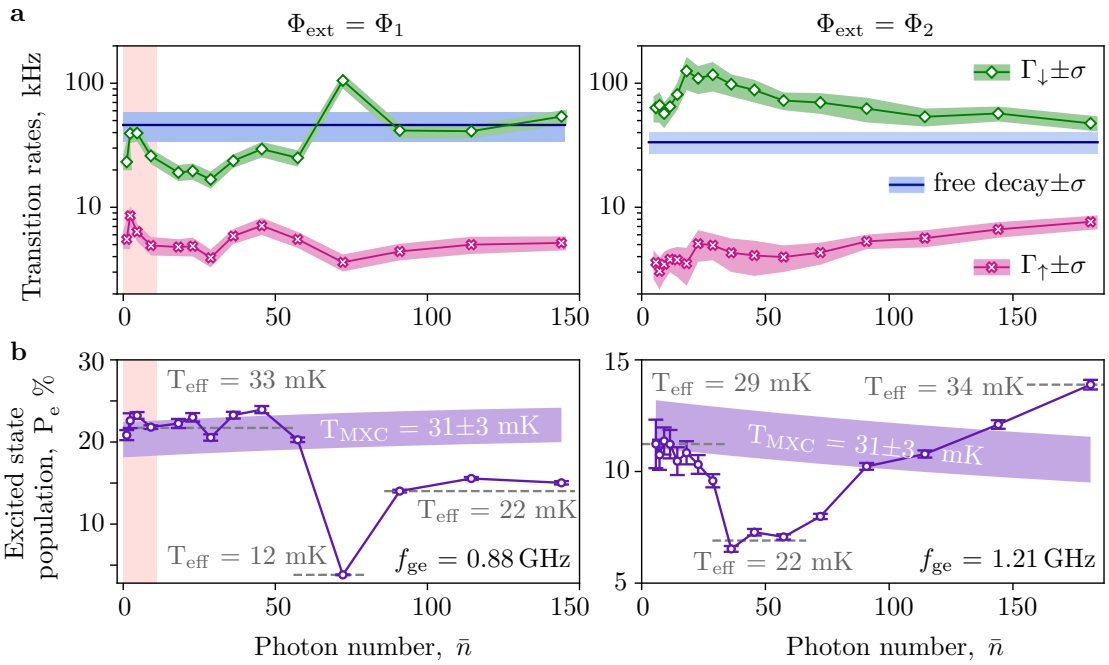

Figure 19: **Atom transition rates and excitation measured in presence of $\bar{n}$ photons in the readout resonator.** The left and right columns of the figure correspond to the flux biases $\Phi_{ext} = \Phi_1$ and $\Phi_{ext} = \Phi_2$, respectively. **(a)** Fluxonium transition rates vs. $\bar{n}$ extracted from quantum jumps measurements (cf. Fig. 17 and Fig. 18). Green and crimson markers correspond to the relaxation and excitation rates, $\Gamma_\downarrow$ and $\Gamma_\uparrow$, respectively. The blue lines with shaded intervals indicate the free decay rate $1/T_1$ with its standard deviation, measured in absence of the readout resonator drive during the atom evolution (see section 2.5.4). The pink shaded interval in the left column presents the results obtained using the DJJAA parametric amplifier [Win+20a], which was indispensable to detect quantum jumps at $\bar{n} < 10$. **(b)** Excited state population (markers) vs. $\bar{n}$ extracted from the IQ histograms. The error bars correspond to the overlap between the $|g\rangle$ and $|e\rangle$ distributions. Grey dashed lines show the levels of the qubit effective temperature calculated from the measured $|e\rangle$ population using Boltzmann distribution (see eq. 93). The shaded purple interval shows the expected thermal occupation of the $|e\rangle$ state calculated assuming thermal equilibrium with the mixing chamber of the dilution refrigerator at temperature $T_{MXC} = 31 \pm 3$ mK. The qubit frequency is different at the two flux biasing points. The tilt of the intervals corresponds to the shift of the atom frequency due to the AC-Stark effect.

Except for some photon-number related spikes in the transition rates there is no clear trend for an increasing relaxation rate with the photon number. For comparison, in Ref. [Min+19] the authors report that the relaxation rate of their transmon qubit increases by a factor of 25 when the resonator is populated with 50 photons, and there is an obvious accelerating trend for the relaxation rate with $\bar{n}$. In our case the total decay rate is of the same order as the free decay rate across the entire range of the photon numbers. The most pronounced spikes in $\Gamma_\downarrow$ are observed at $\bar{n} = 72$ at $\Phi_{ext} = \Phi_1$ (factor of 6) and $\bar{n} = 18{-}54$ at $\Phi_{ext} = \Phi_2$ (factor of 2.5). The spikes were not reproduced in the numerical simulations of the single-mode full system Hamiltonian with included drives, atom decay, and nonlinearity of the shared inductance. Therefore we believe that they can originate from spurious modes of the resonator and the superinductor, similar to Ref. [San+16].

We argue that the measured significant spikes in $\Gamma_\downarrow$ are not related to the time fluctuations of the rates. Usually, the time fluctuations of the rates are correlated, and the total rate Γ_{total} together with the atom excited state population remains stable. In contrast, the measured spikes are reflected in the fluxonium excitation shown in Fig. 19 b. The atom excited state population was extracted from the double-Gaussian fit of the IQ histograms (purple markers). We calculate the fluxonium effective temperature using Boltzmann distribution (see eq. 93). At the photon numbers corresponding to the spikes of the transition rates the effective atom temperature

deviates from the cryostat temperature $T_{MXC} = 31 \pm 3$ mK. The purple interval shows the expected population of the excited state calculated for the atom in the thermal equilibrium with the cryostat. We take into account the AC stark shift of the atom frequency which is positive for $\Phi_{ext} = \Phi_2$ and negative for $\Phi_{ext} = \Phi_1$, according to the sign of the dispersive shift (cf. 16). Notice, that at low photon number the excited state population corresponds to the thermal equilibrium.

Integration time and QNDness of readout

The main benefit of the high power readout is a reduction of the integration time required to obtain the fixed signal to noise ratio which is supposed to improve the readout QNDness. Fig. 20 a demonstrates the integration time required for the single-shot $|g\rangle$ and $|e\rangle$ states discrimination with SNR = 3 as function of the photon number. Left and right panels correspond to the fluxonium biased at $\Phi_{ext} = \Phi_1$ and $\Phi_{ext} = \Phi_2$. The integration time varies slightly for the two biasing points at the same $\bar{n}$ because of difference in the dispersive shifts. As follows from the eq. 42, and eq. 43, the ratio between the dispersive shift and the resonator linewidth defines the position of the pointer states in the IQ plane (see Section 2.2). The absolute value of the dispersive shift decreases with the photon number (see Fig. 16). Fortunately, the decrease of the dispersive shift is slower than $\sqrt{\bar{n}}$ improve of the SNR, and the integration time decreases with $\bar{n}$. Without the use of a parametric amplifier (circle markers) we gain an order of magnitude in the state discrimination time by increasing the readout power from the single photon regime to 150 photons in the readout resonator.

Further improvement can be achieved with the use of a dimer Josephson junction array parametric amplifier (DJJAA) [Win+20a]. The same order of magnitude reduction of the integration time is observed at $\bar{n} = 9$ for DJJAA operated at 20 dB power gain. We demonstrate that combination of the high power readout and parametric amplification allows discrimination

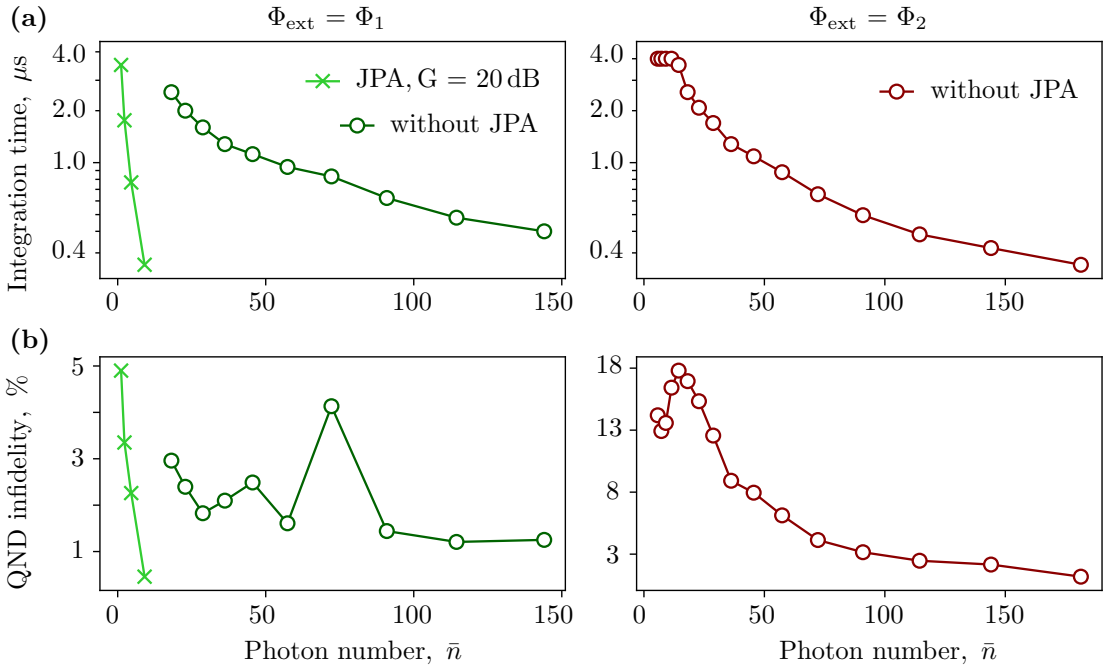

Figure 20: **a** Integration time and QND infidelity of the readout vs $\bar{n}$. Left and right panels correspond to $\Phi_{ext} = \Phi_1$ and $\Phi_{ext} = \Phi_2$, respectively. Markers show the data acquired without (circles) and with (crosses) the use of a dimer Josephson junction array parametric amplifier (DJJAA) [Win+20a] operated at 20 dB of power gain. **a** Reduction of the integration time required for the single-shot state discrimination with SNR = 3 in the continuous wave measurement. **(b)** QND infidelity of the readout calculated from the probability to detect the same fluxonium state in two successive measurements [Das+20; Tou+19]: $1-\mathcal{Q} = 1-(P_{g|g}+P_{e|e})/2$.

of the atom states faster than the response time of the readout resonator $2/\kappa \approx 280\,\mathrm{ns}$ (see Ref. [Tak+21]). For continuous wave measurements at power of $\bar{n} = 56$ photons and SNR = 6 the state discrimination time $\tau = 175\,\mathrm{ns}$.

QNDness of the readout does not necessarily improve with $\bar{n}$ due to a tradeoff between the photon number dependent integration time and the non-QND effects. We extract the readout QND infidelity from the quantum jumps recorded in a continuous wave measurements. The QND infidelity is given by the conditional probabilities to detect the same fluxonium state in two successive measurements: $1-\mathcal{Q} = 1-(P_{\mathrm{g|g}}+P_{\mathrm{e|e}})/2$ [Das+20; Tou+19]. Fig. 20 b shows the extracted QND infidelity. In overall, the QND infidelity decreases with $\bar{n}$ in correspondence with the reduction of the integration time. However, we also observe spikes in the QND infidelity reflecting spikes in the transition rates. Without the use of a parametric amplifier the infidelity is in range of 2−3% for $\bar{n} \geq 114$. By using the DJJAA and a moderate readout power $\bar{n} = 9$ we measure the infidelity below 1%.

Fidelity of the active state preparation

Another way to characterize the QNDness of the high power readout is the process fidelity of the active qubit state preparation. Qubits can also be prepared in the target state by waiting until the thermal equilibrium, and by subsequently applying the conditional π pulse to flip the state. However initialization by thermalization requires time on the scale of the atom energy relaxation. Since the coherence of the superconducting qubits nowadays reaches the millisecond range, this method can impose a limit on the speed of the quantum processors. Active state preparation is done with the measurement based feedback, and allows to reduce the processing time by orders of magnitude. The ability to measure and correct the qubit state with high fidelity plays an essential role in the quantum error correction algorithms.

The atom state preparation starts from a dispersive measurement. The atom state is evaluated in real-time, and depending on the result the conditional π pulse is applied to set the atom in the target state. The state preparation implies fast (compared to the atom decay rate) measurement-based feedback which is implemented using the custom-designed field-

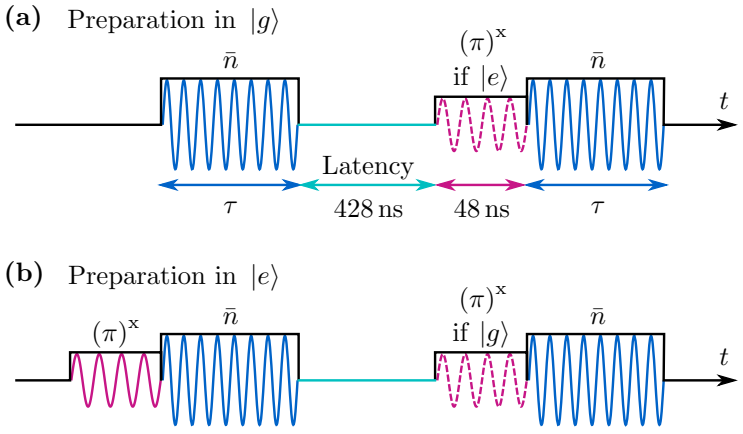

Figure 21: **Pulse sequences used for the fluxonium active state preparation (a)** The $|g\rangle$ state preparation. Pulses in dark blue color correspond to the readout microwave signal of the duration τ, which populate the readout resonator to $\bar{n}$ after the ringup time of ~ 400 ns. We integrate the output IQ signal for the integration time τ_{m} required to achieve the SNR=3. The atom state evaluation takes 428 ns, the feedback latency time of the custom-designed FPGA board [Geb+20]. We apply the conditional π pulse (shown in crimson dashed) if the fluxonium was measured in the $|e\rangle$ state. The last measurement pulse gives the state preparation fidelity. **(b)** The $|e\rangle$ state preparation. We start the preparation sequence with the π pulse (shown in crimson solid) which inverts the atom $|g\rangle$ and $|e\rangle$ states population. Similarly to the $|g\rangle$ state preparation we measure and evaluate the atom state, and apply the conditional π pulse if the fluxonium was measured in the $|g\rangle$ state.

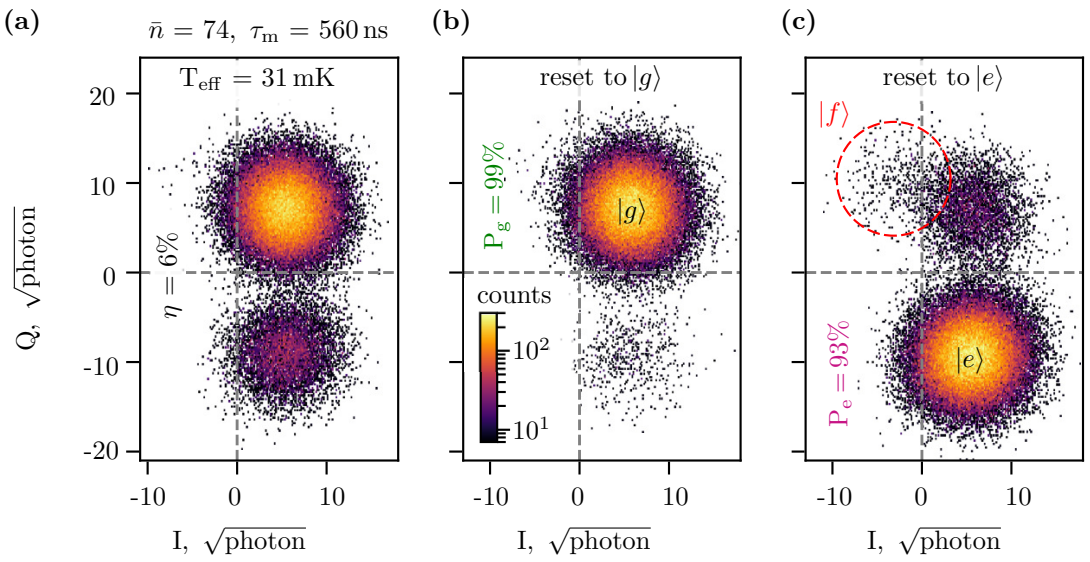

Figure 22: **Fluxonium active state preparation without the use of a parametric amplifier.** Fluxonium is biased at $\Phi_{ext} = \Phi_2$. **(a)** IQ histogram of the repeated pulsed fluxonium measurement without the state preparation. Resonator steady state population is $\bar{n} = 74$. The integration time $\tau_m = 560\,\mathrm{ns}$. From the standard deviation of the Gaussian $|g\rangle$ and $|e\rangle$ states we extract the measurement efficiency $\eta = 6\%$ (see section 2.2) corresponding to an effective noise temperature of 6.0 K. **(b and c)** Histograms for $|g\rangle$ and $|e\rangle$ state preparation, respectively. Green and crimson labels indicate the state preparation fidelity. The red circle in panel c shows the appearance of the fluxonium $|f\rangle$ state, concealed by the dominating $|g\rangle$ state population in panels a and b.

programmable gate arrays (FPGA) electronics board developed in the group of Oliver Sander from KIT [Geb+20] (see also section 5.4 for technical details). The FPGA board was designed for the time domain measurements and control of the microwave circuits, and has the feedback latency of 428 ns.

The pulse sequences used for the $|g\rangle$ and $|e\rangle$ fluxonium state preparation are shown in Fig. 21. For the ground state preparation we start by sending the microwave pulse at the resonator frequency. During the first 400 ns the readout resonator rings up to a state with $\bar{n}$ photons, and we start integrating the output IQ signal for the time τ_m required to achieve the SNR=3 without the use of a parametric amplifier. The IQ plane is divided in the two semi-planes corresponding to the $|g\rangle$ and $|e\rangle$ states. The measured pointer state position gives a binary estimation of the atom state. The state evaluation takes 428 ns, after which we apply the pi pulse if fluxonium was measured in the excited state. We measure the result of the state preparation by applying the second readout pulse with the same power and duration as the first one. For the excited state preparation we apply the pi pulse prior to the first measurement to invert the atom population for a better comparison between the $|g\rangle$ and $|e\rangle$ state preparation. The probability to measure the fluxonium in the target state gives the state preparation fidelity.

The state preparation fidelity is a more stringent way to quantify the QNDness of the high power readout compared to the QNDness extracted from the continuous wave measurements. First of all, in the continuous measurements without the use of a parametric amplifier we could resolve only two lowest states of the atom. The next atom state $|f\rangle$ has a pointer state in the vicinity of $|g\rangle$ state, and transitions to the $|f\rangle$ state contribute to the calculated rates $\Gamma_\uparrow$ and $\Gamma_\downarrow$. The state preparation process includes the manipulation pulse which can not correct the atom state if it was assigned wrongly. Therefore the state preparation fidelity accounts for the atom decay during the measurement (under drive), during the latency time (free evolution), and for the atom manipulation errors.

Fig. 22 a shows the measured IQ histogram for the fluxonium biased at $\Phi_{ext} = \Phi_2$. The histogram was obtained by the repeated pulsed measurements at $\bar{n} = 74$ without the use of a

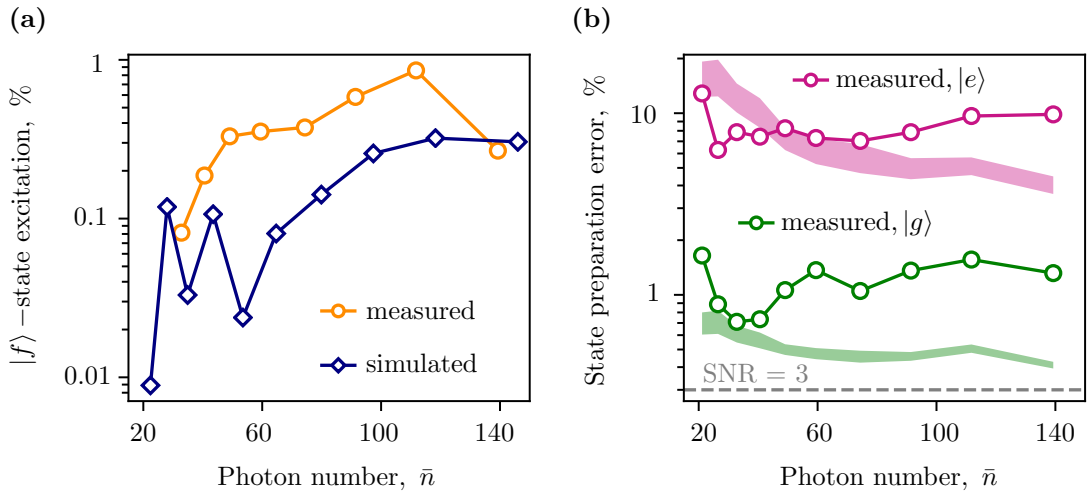

Figure 23: **Fluxonium state preparation error budget. (a)** Population of the fluxonium second excited state $|f\rangle$. Yellow markers show the measured $|f\rangle$ state population extracted from the IQ distributions for the $|e\rangle$ state preparation. The blue markers indicate the expected population calculated by the numerical simulation of the time-dependent atom-resonator Hamiltonian with drive and dissipation. **(e)** State preparation errors. Markers correspond to the errors calculated from the population of the target $|g\rangle$ (green) and $|e\rangle$ (crimson) states. The shaded intervals indicate the expected errors calculated from the measured free decay, $\Gamma_\uparrow$, and $\Gamma_\downarrow$ rates, taking into account the $|f\rangle$ state excitation. The gray dashed line shows the minimal error corresponding to the state discrimination with SNR = 3.

parametric amplifier. This measurement was used to calibrate the integration time required for the SNR = 3, and to find the linear discriminator which divides the IQ plane into the $|g\rangle$ and $|e\rangle$ state semi-planes. For the shown data the discriminator coincides with the I axis. We extract the effective qubit temperature $T_{\text{eff}} = 31\,\text{mK}$ from the calculated population of the Gaussian states. The measurement efficiency $\eta = 6\%$ (see section 2.2) which is ten times smaller than the measurement efficiency with the use of the DJJAA [Tak+21]. The corresponding number of the noise photons per unit time and bandwidth $n_\text{n} = 2\sigma_\text{m}^2 = 15.8$, where σ_m is the average measured standard deviation of the $|g\rangle$ and $|e\rangle$ Gaussian states. An effective noise temperature $T_{\text{eff}} = n_\text{n} h f_\text{r}/k_\text{B} \approx 6\,\text{K}$. For comparison, the noise temperature of the commercial high electron mobility transistor amplifier (HEMT) used in the experiment is $T \approx 2\,\text{K}$. Fig. 22 b,c correspond to the fluxonium prepared in the $|g\rangle$ and $|e\rangle$ states, respectively. The ground state preparation fidelity is 99%, while for the excited state it is few percent smaller. The IQ histogram for the excited state reveals a third cloud in the vicinity of the ground state. By comparing the dispersive shifts and the expected position in the IQ plane we conclude that this cloud corresponds to the fluxonium second excited state $|f\rangle$. The $|f\rangle$ state excitations are particularly harmful for the quantum applications because they are responsible for the qubit leakage out of the computational subspace.

We measure the fluxonium state preparation fidelity for photon numbers from $\bar{n} = 20$ to $\bar{n} = 140$. The state preparation fidelities are above 98% for the excited state, and above 90% for the excited state for $\bar{n} \approx 26{-}140$. The error budget for the fluxonium $|g\rangle$ and $|e\rangle$ state preparation as function of $\bar{n}$ is shown in Fig. 23. Panel a demonstrates the fluxonium $|f\rangle$ state excitation as function of the photon number. Yellow markers correspond to the measured $|f\rangle$ state population calculated from the Gaussian fit of the IQ histograms for the $|e\rangle$ state preparation. We calculate the expected $|f\rangle$ state excitations (blue markers) by numerically simulating the excited state preparation experiment (see the following section for the details). We include both readout drive and the fluxonium free energy decay into the atom-resonator Hamiltonian. The simulations demonstrate that the $|f\rangle$ state excitations are due to the local atom relaxation acting on the hybridized levels of the driven atom-resonator system. Fig. 23 b shows the measured state preparation errors for the ground (green markers) and excited (crimson markers) state. The state discrimination error for the SNR=3 is 0.3%, and it sets the lower limit for the errors. To calculate the expected errors we take into account the atom transitions with rates $\Gamma_\uparrow(\bar{n})$ and

$\Gamma_\downarrow(\bar{n})$ during the readout, the free decay during the latency time, and the $|f\rangle$ state excitations. The expected errors are shown as shaded intervals.

For the excited state the dominant contribution to the state preparation error is the atom energy decay, while for the ground state excitations to the $|e\rangle$ and $|f\rangle$ states give comparable contributions. For the high photon numbers the fluxonium leakage out of the computational space might become a limiting factor for the QND qubit operation. By using a parametric amplifier [Win+20a] combined with the dispersive readout at the moderate power $\bar{n} \approx 10$ we achieved 97% fidelity for the $|e\rangle$ state preparation.

2.5.2 Multimode mixing in atom-resonator Hamiltonian

We believe that the observed resilience of the grAl fluxonium is due to suppressed nonlinearity of the shared, resonator, and atom inductances in comparison to the fluxonium implementations with Josephson junction chains. Nonlinearity is responsible for the multimode mixing in the atom-resonator Hamiltonian and can cause spurious transitions and leakage out of the computational subspace. In the dispersive regime $L_\mathrm{a} \sim 10L_\mathrm{r} \sim 10L_\mathrm{s}$, and the shared inductance usually has the smallest number of Josephson junctions compared to the resonator inductance and fluxonium superinductance. The nonlinearity of the Josephson junction chain is suppressed quadratically with the number of Josephson junctions, therefore nonlinearity of the shared inductance is the strongest one.

In the simplified case we consider L_r and L_a as linear inductances. Then the only difference with the atom-resonator Hamiltonian (eq. 49) is the nonlinear interaction term. We write the interaction Hamiltonian as for the chain of Josephson junctions (see eq. 17)

$$H_\mathrm{int} = -k^2 \frac{(\Phi_0/2\pi)^2}{L_\mathrm{s}} \cos\left(\frac{\varphi_\mathrm{s}}{k}\right). \tag{71}$$

here k is the number of junctions in the shared inductance. The phase ϕ_s across the shared inductance is a dependent degree of freedom, and it can be expressed via ϕ_r and ϕ_a using the Kirchhoff's law for the currents:

$$\frac{1}{L_\mathrm{r}}(\varphi_\mathrm{s}-\varphi_\mathrm{r})+\frac{k}{L_\mathrm{s}}\sin\left(\frac{\varphi_\mathrm{s}}{k}\right)+\frac{1}{L_\mathrm{a}}(\varphi_\mathrm{s}-\varphi_\mathrm{a}) = 0. \tag{72}$$

This equation has no analytical solution for ϕ_s. However, a good intuition can be obtained using the first order approximation. The linearized equation gives

$$\varphi_\mathrm{s} = \frac{L_\mathrm{s}}{L_\Sigma^2}\left(L_\mathrm{a}\varphi_\mathrm{r}+L_\mathrm{r}\varphi_\mathrm{a}\right), \tag{73}$$

here $L_\Sigma^2 = L_\mathrm{r}L_\mathrm{a}+L_\mathrm{r}L_\mathrm{s}+L_\mathrm{a}L_\mathrm{s}$. Substitution of this solution into interaction term (eq. 71) and expansion of the cosine up to the fourth order in its argument yields

$$H_\mathrm{int} \approx H_{\mathrm{int}_1}+H_{\mathrm{int}_2}+H_{\mathrm{int}_3} = -\frac{L_\mathrm{s}}{L_\Sigma^2}\phi_\mathrm{r}\phi_\mathrm{a}-\frac{1}{4k^2}\frac{L_\mathrm{a}^2L_\mathrm{r}^2L_\mathrm{s}^3}{(L_\Sigma^2)^4}\phi_\mathrm{r}^2\phi_\mathrm{a}^2-\frac{1}{6k^2}\frac{L_\mathrm{a}L_\mathrm{r}L_\mathrm{s}^3}{(L_\Sigma^2)^4}\left(L_\mathrm{r}^2\phi_\mathrm{r}\phi_\mathrm{a}^3+L_\mathrm{a}^2\phi_\mathrm{a}\phi_\mathrm{r}^3\right), \tag{74}$$

here H_{int_1} corresponds to the linear coupling, while H_{int_2} and H_{int_3} are responsible for the multimode mixing between atom and resonator. For the circuit parameters used in Fig. 8 the interaction terms scale as $H_{\mathrm{int}_2}/H_{\mathrm{int}_1} \approx 0.07/k^2$, and $H_{\mathrm{int}_3}/H_{\mathrm{int}_1} \approx 0.2/k^2$. Replacing Josephson junction array by granular aluminum increases k by at least an order of magnitude, and multimode mixing is suppressed to a percent fraction of linear coupling.

At first glance the problem of multimode mixing seems to be solved in the linear capacitive coupling schemes (see Fig. 7). However, we argue that necessity to couple via the Josephson junction capacitance negates the benefit. In these schemes the electromagnetic field induced by coupling to the readout resonator concentrates in the area of nonlinear junction, and multimode mixing should be comparable or even larger than in case of the inductive coupling via Josephson junction array.

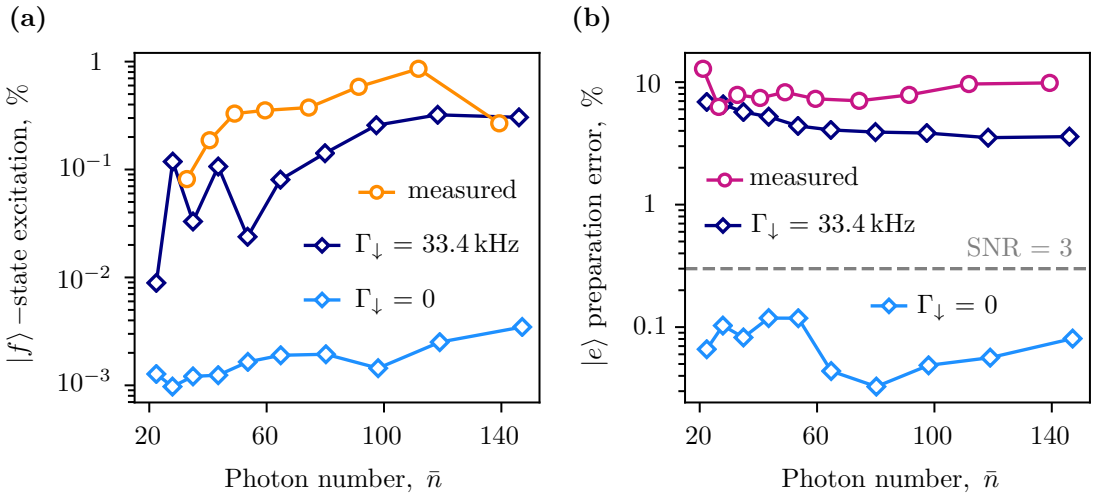

Figure 24: **Error budget for the atom $|e\rangle$ state preparation. (a)** Leakage to the second excited atom state $|f\rangle$. Yellow markers show measured $|f\rangle$ state excitation probability. Blue markers correspond to the calculated values extracted from the numerical simulations of $|e\rangle$ state preparation process with $\Gamma_\downarrow = 33.4\,\mathrm{kHz}$ (dark blue) and $\Gamma_\downarrow = 0\,\mathrm{kHz}$ (light blue) atom local decay included in the time dependent system Hamiltonian. The value of $\Gamma_\downarrow = 33.4\,\mathrm{kHz}$ is taken according to the measured free decay of the atom. **(b)** The $|e\rangle$ state preparation error. The simulated $|e\rangle$ state preparation error with atom local decay $\Gamma_\downarrow = 33.4\,\mathrm{kHz}$ (dark blue markers) is of the same order as the measured error (crimson), while excluding atom local decay (light blue markers) results in two orders of magnitude smaller errors, below the state discrimination threshold for SNR = 3.

2.5.3 Numerical simulation of the state preparation errors

Numerical simulations of dynamics of open multi-level quantum systems require large computational resources. Numerical simulations were performed by Madita Willsch from the research group lead by Prof. Dr. Kristel Michielsen, using the supercomputer JUWELS [Jül19] located at the Jülich Supercomputing Centre. We define the time dependent atom-resonator Hamiltonian

$$H = H_0 - E_I \sin(\omega_d t)\phi_\mathrm{r}, \tag{75}$$

where H_0 is the static atom-resonator Hamiltonian defined in eq. 49 with tunable Josephson energy (eq. 58), and the last term describes an external time-dependent resonator drive with amplitude E_I and frequency ω_d that represents the measurement pulse applied to the system. We perform the simulations for different values of the drive amplitude E_I to obtain steady state photon numbers matching the ones observed in the experiment.

We include the dissipative effects by considering the Lindblad master equation for the time evolution of the density matrix $\rho(t)$

$$\begin{aligned}\frac{\partial}{\partial t}\rho(t) &= -i[H,\rho(t)] \\ &- \sum_{k=1,2}\left(\frac{1}{2}L_k^\dagger L_k\rho(t) + \frac{1}{2}\rho(t)L_k^\dagger L_k - L_k\rho(t)L_k^\dagger\right).\end{aligned} \tag{76}$$

The Lindblad operator $L_1 = \sqrt{\kappa}a_\mathrm{r}$ models the resonator decay with rate $\kappa/2\pi = 1.16\,\mathrm{MHz}$. We define the atom decay operator as $L_2 = \sqrt{\Gamma_\downarrow}\sum_j \sqrt{j}\,|j-1\rangle\langle j|$, where $\Gamma_\downarrow = 33.4\,\mathrm{kHz}$ is the atom free decay rate measured at $\Phi_\mathrm{ext} = \Phi_2$, and $|j\rangle$ denotes the j-th bare atom eigenstate, obtained by diagonalizing the atom part of the Eq. 75. We obtain the solution to Eq. 76 by utilizing the wave-function Monte–Carlo method [DCM92; DZR92; Jac14]. The simulated probabilities to detect the atom in the states $|g\rangle$, $|e\rangle$ and $|f\rangle$ were averaged during same measurement time τ_m as in the experiment. These probabilities were used to calculate the expected errors for the $|e\rangle$ state preparation as function of the readout photon numbers (see Fig. 24). We emphasize that the atom leakage out of the computational subspace, which is two orders of magnitude

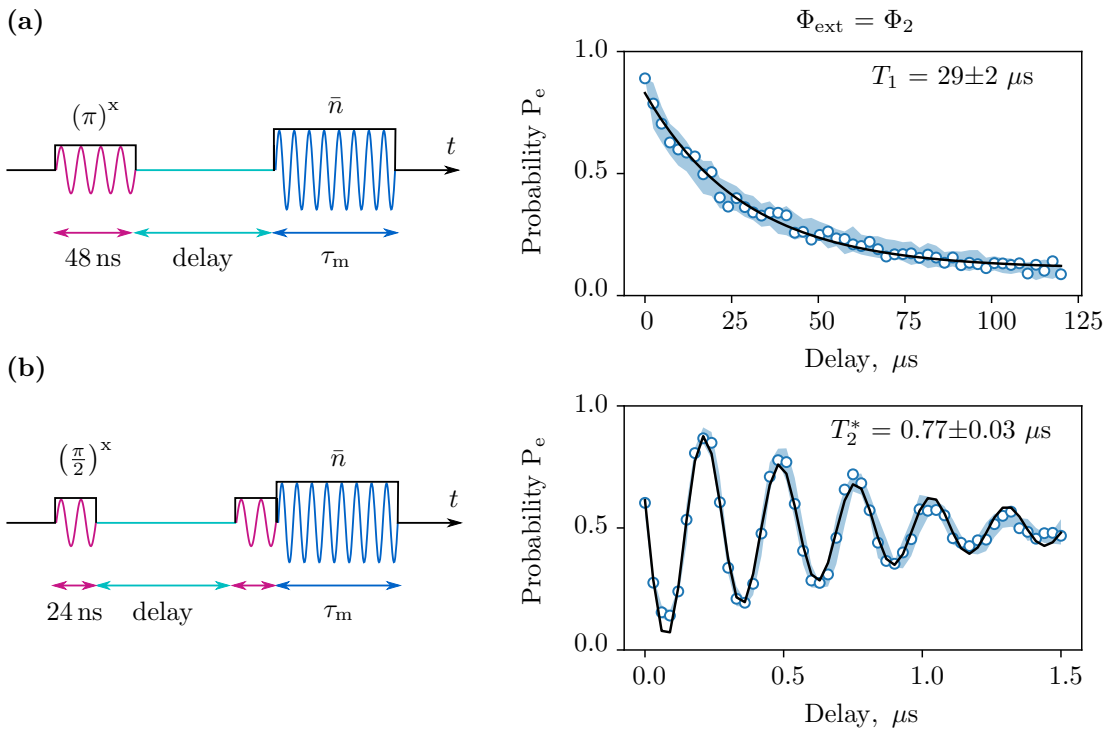

Figure 25: **Coherence of the grAl fluxonium with tunable Josephson energy.** Left column shows the pulse sequences used to measure the energy relaxation time T_1 and the Ramsey coherence time T_2^* (panel a and b, respectively). Manipulation and readout pulses are shown in crimson and dark blue, respectively. Right column demonstrates the measurement result for the fluxonium atom biased at $\Phi_{ext} = \Phi_2$. Blue markers correspond to the measured data, and black line is the numerical fit. Notice that the contrast is reduced due to the thermal population of the atom. We use exponential function to extract T_1, and damped cosine function to extract T_2^*. The blue shaded intervals show spread of the data measured at readout power corresponding to $\bar{n} = 5{-}140$ photons in the readout resonator. As expected, fluxonium coherence does not depend on $\bar{n}$ because resonator is not populated during the atom free evolution. Labels indicate the average values of T_1 and T_2^* and their standard deviation.

higher than expected from thermal population of the $|f\rangle$ state, is due to the atom relaxation acting on the hybridized levels of the driven atom-resonator system (compare the results with and without atom decay in Fig. 24).

2.5.4 Atom coherence

The two figures of merit which quantify the qubits coherence are the energy relaxation time, and the decoherence time of the superposition state $(|g\rangle{+}|e\rangle)/2$. The energy relaxation is given by the sum of the transition rates between $|g\rangle$ and $|e\rangle$

$$\frac{1}{T_1} = \Gamma_\uparrow{+}\Gamma_\downarrow. \tag{77}$$

For qubit prepared in the excited state the probability P_e decays exponentially with time to the equilibrium value $(\Gamma_\downarrow{-}\Gamma_\uparrow)/(\Gamma_\uparrow{+}\Gamma_\downarrow)$. The decoherence rate has two contributions

$$\frac{1}{T_2^*} = \frac{1}{2T_1}{+}\frac{1}{T_\varphi}. \tag{78}$$

The first term in this equation corresponds to destruction of the superposition state due to transitions, while the second term corresponds to pure dephasing caused by random fluctuations of the qubit frequency. In the absence of pure dephasing $T_2 = 2T_1$.

The pulse sequence used to measure the fluxonium energy relaxation T_1 is shown in Fig. 25 a. Initially, the fluxonium atom is in the thermal equilibrium state with $P_{\text{thermal}} \approx 12\%$. We apply the resonant π-pulse at ω_{ge} to invert the fluxonium population. The probability to measure atom in the excited state P_{e} is measured after the variable delay. Measurements were made for the steady state $\bar{n} = 5{-}140$ photons inside the readout resonator. Since resonator is not populated during the free atom evolution the measurement gives the atom free decay rate. The right panel of the figure shows the measured excited state population. Markers demonstrate data for $\bar{n} \approx 5$, while the shaded interval indicates the spread of probabilities for measurements at different $\bar{n}$. As expected, the free decay T_1 of the fluxonium does not depend on the readout power. The measured T_1 is four orders of magnitude smaller than expected from the calculated Purcell relaxation rate (see section 2.5.5). Similarly to the single-loop fluxonium, energy relaxation could be dominated by dielectric losses or losses induced by non-equilibrium quasiparticles [Grü+19].

We use the Ramsey pulse sequence (see Fig. 25 b) to measure the atom decoherence time T_2^* [Ram50]. It consists of the two off-resonant $\pi/2$-pulses separated by a variable delay. The drive frequency was detuned from the atom transition by $\Delta = 3.5\,\text{MHz}$. The first $\pi/2$ pulse leaves the atom in the $(|g\rangle{+}|e\rangle)/2$ superposition state. The atom state accumulates phase during the free evolution until the second $\pi/2$ pulse projects the atom onto the longitudinal axis. The measured excited state population shows sinusoidal oscillations with frequency Δ. The fluxonium decoherence time was extracted from a fit of the measured probability P_{e} with an exponentially damped cosine function. The measured $T_2^* \approx 0.77\,\mu\text{s}$ is two orders of magnitude smaller than expected in the limit of zero dephasing, although the fluxonium was biased at the spectral minimum $\Phi_{\text{ext}} = \Phi_2$ where sensitivity to flux noise should be suppressed up to the first order. For comparison, the single-loop fluxonium has $T_2^* \approx T_1$ [Grü+19]. The tunability of the Josephson energy achieved by adding another loop to the circuit comes with a price of increased dephasing. From eq. 58 follows that in presence of the local flux noise the fluxonium circuit has no bias point with zero derivative in respect to both Φ_ℓ and Φ_{s}. Such local flux noise can be generated by magnetic impurities in the materials.

2.5.5 Purcell decay rate

Dispersive coupling of the atom and the readout resonator leads to hybridization of their levels. The atom relaxation caused by coupling bears the name of Purcell decay rate[Pur46] which sets the upper bound for the atom lifetime. The Purcell decay rate can be calculated by including dissipation in the system dynamics. In quantum mechanics dissipation is modeled by coupling quantum system to a continuum of modes (harmonic oscillator bath). The bath acts as an external noise source which can exchange energy with the system and cause transitions between the system's states. The transition rates are related to the noise spectral density of the bath [Cle+10] and are calculated using the Fermi's Golden Rule.

Here we outline the results of the unpublished derivation of the fluxonium Purcell decay rate made by Dr. Gianluigi Catelani, by kind permission of the author. First, the harmonic oscillator bath is represented as the fluctuating voltage source V coupled capacitively to the readout resonator (see Fig. 26). The circuit Lagrangian

$$\begin{aligned}\mathscr{L} = &\frac{1}{2}C_{\text{r}}\dot{\phi_{\text{r}}}^2 + \frac{1}{2}C_{\text{a}}\dot{\phi_{\text{a}}}^2 + \frac{1}{2}C_\kappa(\dot{\phi}_{\text{r}} - V)^2 \\ &- \frac{1}{2L_{\text{r}}}(\phi_{\text{s}} - \phi_{\text{r}})^2 - \frac{1}{2L_{\text{a}}}(\phi_{\text{s}} - \phi_{\text{a}})^2 - \frac{1}{2L_{\text{s}}}\phi_{\text{s}}^2 + E_{\text{J}}\cos(\varphi_{\text{a}} - \varphi_{\text{ext}})\,.\end{aligned} \tag{79}$$

We use the normal mode basis (see section 2.4) to decouple the harmonic modes with atom and resonator variables. In this basis the atom and the resonator are coupled only via the Josephson energy term, but coupling to the voltage source appears both for the atom and the resonator

$$H = \frac{Q_{\text{R}}^2}{2C_{\text{R}}} + \frac{Q_{\text{A}}^2}{2C_{\text{A}}} + \frac{\phi_{\text{R}}^2}{2L_{\text{R}}} + \frac{\phi_{\text{A}}^2}{2L_{\text{A}}} - E_{\text{J}}\cos(\phi_{\text{A}} + \lambda_3\phi_{\text{R}} - \varphi_{\text{ext}}) + \frac{C_\kappa}{C_{\text{R}}}VQ_{\text{R}} + \lambda_2\frac{C_\kappa}{C_{\text{A}}}VQ_{\text{A}}, \tag{80}$$

here λ_2 and λ_3 are the numerical coefficients; and $C_{\text{R,A}}$ and $L_{\text{R,A}}$ are the rescaled resonator and atom capacitances and inductances, respectively. For the circuit parameters used in the

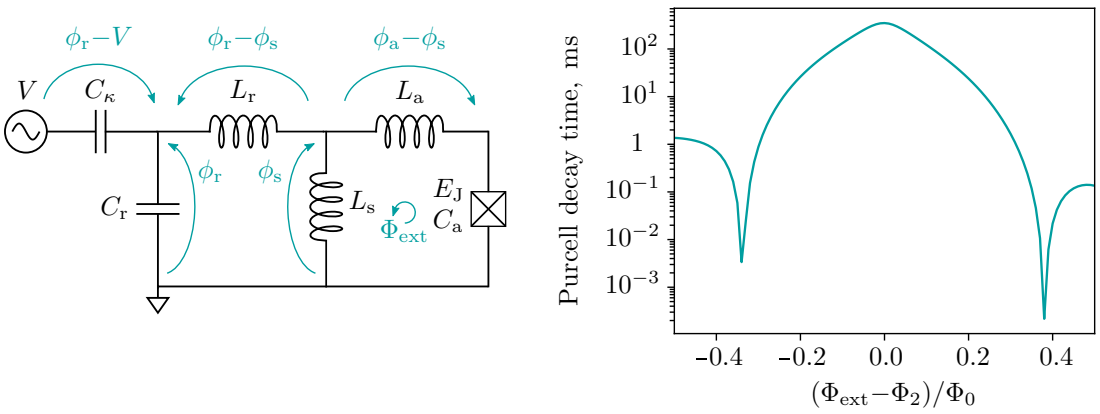

Figure 26: **Calculation of the Purcell fluxonium decay rate.** Left panel shows the equivalent atom-resonator circuit coupled to the fluctuating voltage source V via capacitance C_κ. The source represent the harmonic oscillator bath with continuous spectrum. The coupling Hamiltonian is treated as perturbation, and atom Purcell relaxation rate is calculated from the transition probabilities using the Fermi's Golden Rule (see main text). The right panel shows the calculated Purcell decay time as function of the external magnetic field around the $\Phi_{ext} = \Phi_2$ bias point.

experiment $|\lambda_2| \approx 5{\times}10^{-3}, |\lambda_3| \approx 0.02$. The fluctuating voltage is then replaced by the coupling term to the harmonic oscillator bath $V \to \sum_k \lambda_k Q_k$. Applying the Fermi's Golden rule we obtain the resonator and the atom decay to the bath

$$\begin{aligned} \Gamma_{\downarrow}^{\mathrm{R}} &= \left(\frac{C_\kappa}{C_\mathrm{R}}\right)^2 |\langle 0g|\, Q_\mathrm{R}\, |1g\rangle|^2 S(\omega_\mathrm{R}) \equiv \kappa, \\ \Gamma_{\downarrow}^{\mathrm{Q}} &= \lambda_2^2 \left(\frac{C_\kappa}{C_\mathrm{A}}\right)^2 |\langle 0g|\, Q_\mathrm{A}\, |0e\rangle|^2 S(\omega_\mathrm{ge}) \equiv \frac{1}{T_1}. \end{aligned} \tag{81}$$

Here $S(\omega)$ is the noise source spectral density which grows linearly with frequency for the Ohmic bath. In the limit of weak coupling $\lambda_2, \lambda_3 \ll 1$ and the Purcell decay time

$$T_1 \approx \frac{\omega_\mathrm{R}}{\omega_\mathrm{ge}} \frac{1}{\kappa} \frac{1}{p}, \quad p = \frac{|\langle 0g|\, Q_\mathrm{r}\, |0e\rangle|^2}{|\langle 0g|\, Q_\mathrm{r}\, |1g\rangle|^2}. \tag{82}$$

Notice that we have the initial uncoupled resonator charge operator in the participation factor p. This factor relates the transition probabilities under action of the resonator charge on the hybridized resonator and atom states (see section 2.5.5 for the charge matrix elements). The hybridized states were obtained by diagonalization of the atom-resonator Hamiltonian.

Dipole matrix elements

The matrix elements between states $|n, e\rangle$ and $|n, g\rangle$ of the charge and flux operators give coupling strength of the atom to dissipation channels as was shown in detail in Ref. [Grü19]. Fig. 27 demonstrates the calculated matrix elements for the uncoupled readout resonator charge q_r, atom flux ϕ_a, and atom charge q_a as function of the external magnetic field. We calculate the matrix elements numerically by representing charge and flux in terms of raising and lowering operators of the bare harmonic oscillator modes. The resonator charge matrix elements are nonzero due to hybridization of the coupled atom and resonator levels. In favor of the high power QND readout, in the vicinity of the fluxonium bias $\Phi_{ext} = \Phi_1$ and $\Phi_{ext} = \Phi_2$ all matrix elements do not increase with the photon number. The peaks of the resonator charge matrix elements (Fig. 27 a) correspond to crossings between the levels $|0, e\rangle$ and $|1, g\rangle$, while the dips in the vicinity of $\Phi_{ext} = \Phi_1$ correspond to crossings between the levels $|1, e\rangle$ and $|0, f\rangle$.

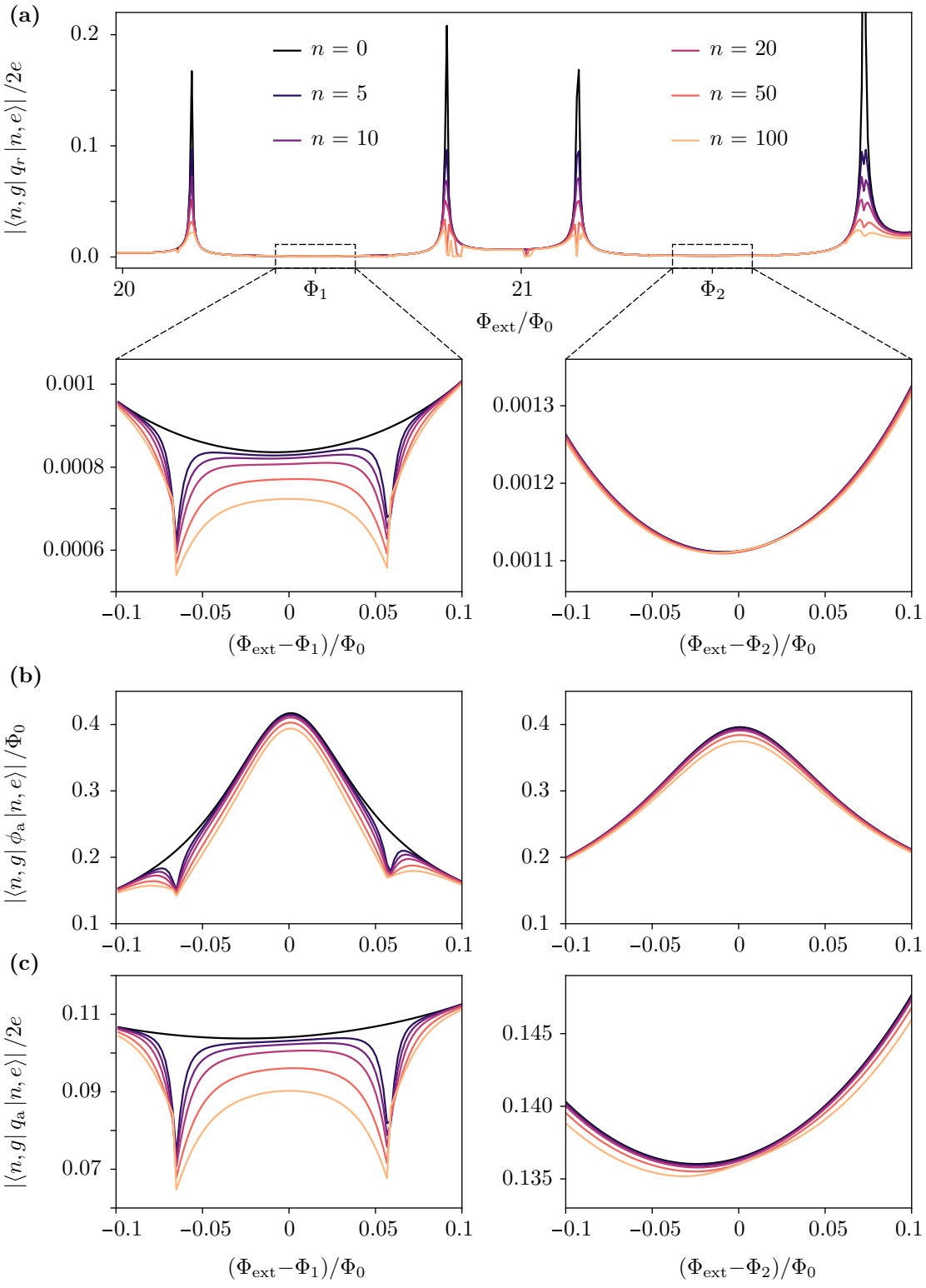

Figure 27: **Absolute value of the matrix elements between hybridized atom-resonator states $|n,e\rangle$ and $|n,g\rangle$ vs. $\Phi_{\rm ext}$.** Panels **a, b, c** show the matrix elements of the uncoupled readout resonator charge $q_{\rm r}$, atom flux $\phi_{\rm a}$, and atom charge $q_{\rm a}$ operators, respectively. The color code indicates the readout resonator photon number. Notice the difference in scale between the matrix elements of the resonator and the atom operators. The resonator and atom charge matrix elements are comparable only in the vicinity of crossings between the $|0,e\rangle$ and $|1,g\rangle$ levels (peaks in panel a).

2.6 Gradiometric fluxonium atom

The gradiometric design of the fluxonium atom allows to suppress its sensitivity to magnetic fields homogeneous on the scale of the device. The flux trapped in the superconducting loop remains after external field is ramped down to zero. Ideally, this implies elimination of decoherence due to the bias source noise. In addition, removing the flux degree of freedom in the experiment by freezing the gradiometric fluxonium at the degeneracy point is beneficial in the scale up of superconducting quantum systems, as it suppresses correlated errors caused by fluctuations of the environmental field.

Our interest in the gradiometric fluxonium is dictated by possible applications in quantum fluxon electronics [LS91; BLZ01], and quantum simulators [Pet+18]. The field-protected gradiometric artificial atoms can also be used for hybrid quantum circuits, which require high magnetic fields to operate natural spins [Xia+13]. In this section we discuss the design, implementation and characterization of the granular aluminum gradiometric fluxonium atom. I would like to mention that superconducting gradiometric atoms were already presented in literature, for example, flux qubits with tunable gap [Sch+13], and gate-tunable fluxonium [Pit+20]. However, to our knowledge, there is no comprehensive study demonstrating field sensitivity suppression, flux trapping, and coherence of the atoms simultaneously.

The concept of the gradiometric fluxonium atom

The gradiometric fluxonium atom can be built from a Josephson junction enclosed by two superconducting loops of equal size. The superconducting material used for the loops should have high impedance to suppress charge fluctuations, and low internal microwave losses to preserve quantum coherence. The equivalent schematic of the atom is shown in Fig. 28.

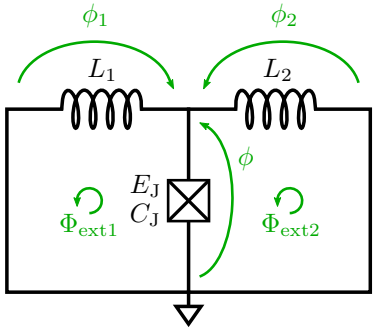

Figure 28: **Equivalent schematic of the gradiometric fluxonium atom.** The Josephson junction (JJ) with the Josephson energy E_J and the parallel plate capacitance C_J is enclosed by two superconducting loops with kinetic inductances L_1 and L_2, respectively. The green arrows show the assigned branch flux variables and the direction of the external magnetic field Φ_{ext1} and Φ_{ext2} in the loops.

According to fluxoid quantization [Tin04], the total flux threading the superconducting loop, constituted by the sum of the applied external flux and flux induced by the screening current, is quantized. We consider the two loops formed by the Josephson junction and each of the inductances to write the boundary conditions:

$$\begin{aligned} \phi - \phi_1 + \Phi_{ext1} &= n\Phi_0 \\ \phi_2 - \phi + \Phi_{ext2} &= m\Phi_0 \end{aligned} \tag{83}$$

Here Φ_{ext1} and Φ_{ext2} are the external magnetic fluxes in the loops (see Fig. 28); n and m are the integer numbers of flux quanta trapped in each loop, and Φ_0 is the flux quantum. The numbers of trapped flux n and m are are further restricted by the fluxoid quantization of the outer loop

$$m + n = k, \tag{84}$$

where k is the integer number of flux trapped in the outer loop. With the boundary conditions taken into account, the gradiometric fluxonium circuit is described by a Hamiltonian with one degree of freedom:

$$H = \frac{q^2}{2C} + \frac{1}{2L_\mathrm{a}} \left(\phi - \Phi_\mathrm{d} + \alpha\Phi_\Sigma\right)^2 - E_\mathrm{J} \cos\varphi, \tag{85}$$

where atom capacitance C is determined by the sum of the parallel plate capacitance of the Josephson junction and the coplanar capacitance of the connecting electrodes. The equivalent linear inductance of the atom equals the inductance of the two loops connected in parallel $L_\mathrm{a} = L_1 L_2/(L_1+L_2)$. The $\Phi_\mathrm{d} = (\Phi_\mathrm{ext1}-\Phi_\mathrm{ext2})/2+(m-n)\Phi_0/2$ term corresponds to the gradient of total flux threading the two loops. The coefficient $\alpha = (L_1-L_2)/(L_1+L_2)$ reflects the asymmetry of the loop inductances. It is responsible for the residual atom flux sensitivity $\Phi_\Sigma = (\Phi_\mathrm{ext1}+\Phi_\mathrm{ext2})/2+k\Phi_0/2$. In case of perfectly symmetric inductance atom feels only the gradient of flux.

In order to pin the atom at the degeneracy point it should be threaded by a magnetic field leading to an odd number of magnetic flux quanta in the outer loop prior to the cooldown. After the superconducting phase transition the flux is trapped in the outer loop. In case of equal area of the two loops and homogeneous magnetic field external flux Φ_ext1 equals to Φ_ext2. The superconducting state with the lowest screening current corresponds to the trapped flux distribution $|m-n| = 1$. The state with larger difference between trapped fluxes is metastable and relaxes to the ground state via phase slips through the tunnel Josephson junction. As a result, the effective atom bias is $\Phi_\mathrm{d} = 0.5\,\Phi_0$. The applied magnetic field can be ramped down to zero because induced circulating currents in the loop preserve the value of the trapped flux. The trapped flux tunnels between the loops through the Josephson junction creating a superposition of circulating currents, in a complete analogy to the non-gradiometric fluxonium biased at the degeneracy point.

Circuit implementation

With the view of possible applications of the gradiometric fluxonium in hybrid circuits we need materials which preserve coherence in strong magnetic fields. For the proof of principle device we decided to use granular aluminum (grAl) for the fluxonium inductors, and Al−$\mathrm{AlO_x}$−Al Josephson junction as nonlinear element. GrAl is resilient to in-plane magnetic fields up to 1 T as was demonstrated in Ref. [Bor+20], and also can be used as a nonlinear element to construct qubits [Win+20b]. However since we do not have established fabrication of grAl nonlinear elements with well controlled parameters, we choose more reliable conventional Josephson junctions. We aim at demonstrating suppression of the fluxonium sensitivity to the external field, and flux trapping during cooldown.

The circuit implementation of the gradiometric fluxonium coupled to the readout antenna resonator is shown in Fig. 29. The sapphire chip contains four gradiometric atoms and four non-gradiometric atoms each coupled to the readout resonator via a shared inductance. The test structures located at the edges of the chip are used to check the room temperature resistance of the Josephson junctions and grAl film from which we calculate the expected Josephson energy and kinetic inductance, respectively (see eq. 16 and eq. 100). Typically, we observe a spread of ±30% of the grAl resistance, and ±10−20% of the junctions resistance across the wafer.

The non-gradiometric atoms are used as reference to calibrate the external magnetic field by measuring the periodicity of their spectrum. The fluxonium loops are made of granular aluminum wires with a sheet kinetic inductance of $L_\mathrm{kin} = 0.14$−$0.2\,\mathrm{nH}/\square$, corresponding to a maximum of the superconducting gap in grAl [Pra+16; Lev+19]. We design atoms with the same dimensions of grAl inductors, because we expect the natural spread of the atom frequencies due to variation of kinetic inductance and Josephson energy across the wafer. The loop size is comparable with design of the fluxonium with tunable Josephson junction (see section 2.5). In principle, more compact atoms can be built using grAl with higher resistivity.

Fig. 30 shows a sapphire chip mounted inside the copper waveguide sample holder (see section 5.2). We perform finite element simulation of the electromagnetic field inside the waveguide to find the optimal geometry of the resonator dipole antenna which yields target $\kappa_c/2\pi \approx$

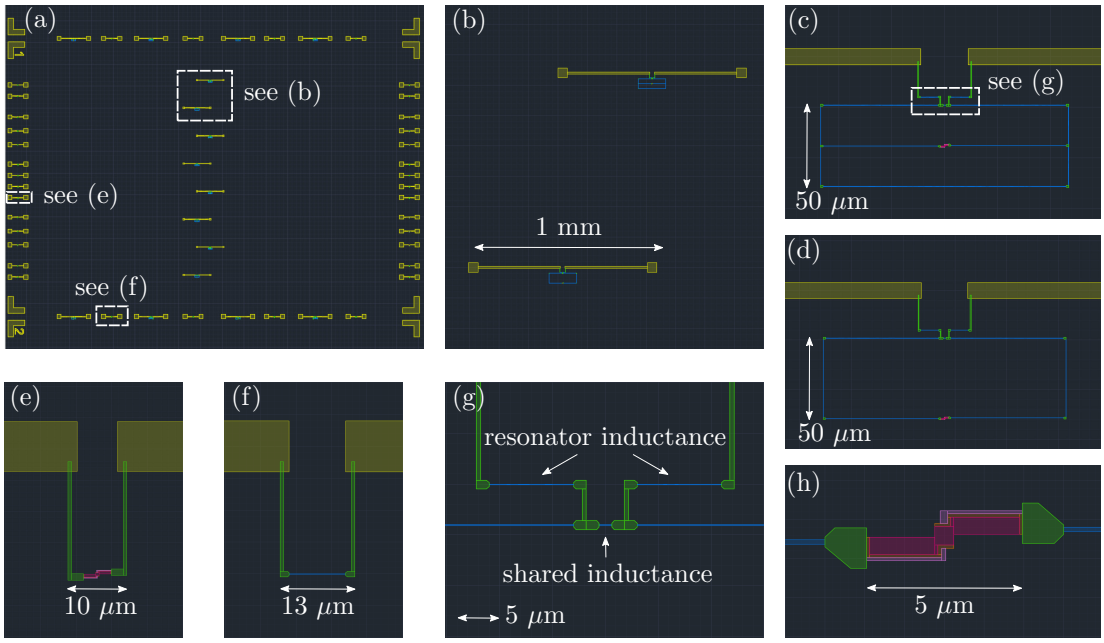

Figure 29: **The chip design.** **(a)** The chip contains eight coupled atom-resonator circuits located in the center, and the test circuits located at the edges. The color of the patterns corresponds to the different e-beam dose used for the large and small structures (see section 5.1). **(b)** A zoom-in showing one gradiometric (top) and one non-gradiometric atom (bottom) each coupled to the readout resonators via a shared inductance. The readout resonators have the shape of a dipole antenna, the capacitance pads (granular aluminum shunted with Al) are shown in yellow. **(c, d)** A zoom into the central parts of the circuits for gradiometric and non-gradiometric fluxoniums, respectively. The outer loops of the gradiometric fluxonia are of equal size ($50\times150\,\mu m^2$) with loops of the non-gradiometric ones. **(e, f)** The Josephson junction and the grAl test structures, correspondingly, which were used to measure the room temperature resistances of the Josephson junction and the grAl film. **(g)** A zoom into the grAl readout resonator inductance and the shared inductance. Green color indicates connecting electrodes (grAl shunted with Al). **(h)** Double-angle shadow evaporation mask for the Niemeyer-Dolan type Josephson junction [Nie+74]. Pink color indicates mask for the junction electrodes. Crimson and orange color correspond to the resist undercut.

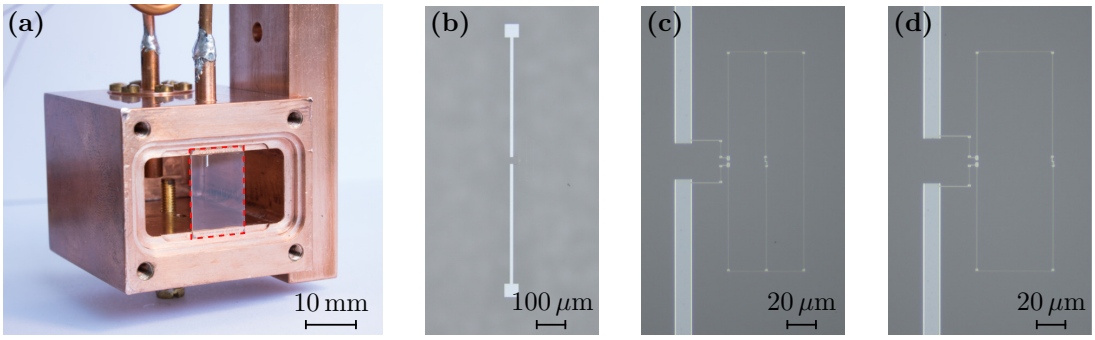

Figure 30: **Sample in 3D copper waveguide.** **(a)** The copper waveguide without the cap. Red dashed rectangle indicates C-plane sapphire chip with eight atom-resonator structures located in the middle. The waveguide is attached to the copper rod which provides thermalization to the mixing chamber plate of the dilution refrigerator. Detailed description of the waveguide and magnetic shielding of the sample is presented in section 5.2. **(b)** Optical microscope image of the resonator dipole antenna. **(c, d)** Central parts of the gradiometric and non-gradiometric fluxonium atoms coupled to the readout resonators, respectively.

Mode number	1	2	3	4
Mode frequency, GHz	3.65	13.06	13.18	14.05
Coupling Q	5.7×10^{10}	2.7×10^{7}	4.1×10^{7}	1.9×10^{8}

Table 1: **Eigenmodes of the gradiometric fluxonium loops.** Frequencies of the eigenmodes and their coupling quality factors were obtained with the Ansys HFSS simulation of the fluxonium loops in the 3D waveguide sample holder. We use a linearized model of the atom with Josephson energy excluded from the simulation. The Josephson junction is modeled as a lumped capacitance.

1.0 MHz coupling rate of the resonator mode to the readout port (see section 5.3). From simulation we extract the resonator capacitance $C_\mathrm{r} = 20.2\,\mathrm{fF}$. We vary the inductance of the eight resonators on the chip within 20% to achieve a 100 MHz spacing between them. The corresponding resonator frequencies 6.7−7.5 GHz lie in the passband of the waveguide.

We also simulate a distribution of the electromagnetic field in the fluxonium loops to find their self-resonant frequencies. Fluxonium atoms designed for inductive coupling to the readout resonator typically have small electric dipole moments and the first transition frequency below the waveguide cutoff. This allows to decouple the atom from stray electromagnetic fields and suppress the radiative losses. In order to reduce the computational complexity we simulate the fluxonium loops separately, without coupling to the readout resonator. The Josephson junction is represented as a lumped capacitance given by the parallel plate capacitance of the Josephson junction and the coplanar capacitance of the connecting electrodes. The simulated loops eigenmodes, up to 15 GHz, and their coupling quality factors are listed in Table 1.

We utilize the three angle electron-beam evaporation technique (see Fig. 31 a, b) to fabricate the entire circuit including Josephson junctions and grAl wires in a single lithography step [Grü+19]. First, the Josephson junction electrodes are evaporated at angles of ±30°. The first layer of the Josephson junction is oxidized to obtain the insulating tunnel barrier. Before evaporation of the grAl wires the oxide in the areas of contact between aluminum and grAl is removed with argon ion milling [Grü+17]. After that grAl wires are evaporated at the zero

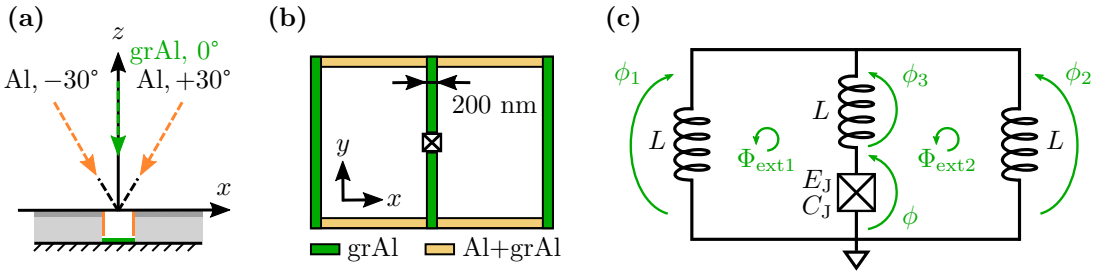

Figure 31: **Fabrication details of the gradiometric fluxonium.** **(a)** A sketch of the three angle metal deposition technique used to evaporate the aluminum Josephson junction electrodes (orange) and granular aluminum wires (green). The substrate is located parallel to the XY plane. We use the Copolymer EL13 / PMMA A4 double-layer e-beam resist stack (light grey and dark grey, respectively) to pattern the mask. The image demonstrates evaporation of 200 nm wide grAl wires. Note, that there is no undercut in the bottom resist layer. Therefore, the aluminum layers (20 and 30 nm thick) evaporated at ±30° angle are deposited on the resist walls, and are hence removed after the lift-off. GrAl wires (50 nm thick) are evaporated at zero angle. **(b)** A schematic image of the metal layers in the gradiometric fluxonium loops. The Josephson junction is shown symbolically. The wires along the Y axis are out of grAl, while wires along the X axis consist of grAl shunted by aluminum. The middle grAl wire forms an additional inductance in series with the Josephson junction. **(c)** Equivalent schematic of the fluxonium atom with an additional inductance. The circuit is described by the Hamiltonian Eq. 90, with the atom equivalent inductance $L_\mathrm{a} = 3L/2$.

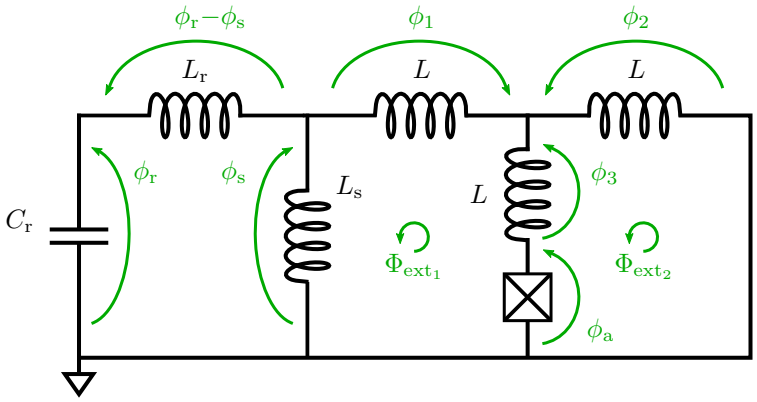

Figure 32: **Circuit schematic of the gradiometric fluxonium coupled to the readout resonator**.

angle. Due to the circuit geometry we get an additional inductance in series with the Josephson junction (see Fig. 31 b, c). It has no internal dynamics, and the circuit Hamiltonian can also be reduced to the Hamiltonian of a simple fluxonium. In case of the equal inductances in all three brunches

$$H = \frac{q^2}{2C}+\frac{1}{2L_a}\left(\phi-\Phi_d\right)^2-E_J\cos\varphi, \tag{86}$$

where the atom equivalent inductance $L_a = 3L/2$, and Φ_d is the field gradient between the two loops. Details of the fabrication process are presented in section 5.1.

Gradiometric fluxonium with additional inductance coupled to the readout resonator

The fluxoid quantization in the superconducting loops gives boundary conditions

$$\begin{aligned}\phi_1-\phi_3-\phi_a+\phi_s-\Phi_{ext1} &= n\Phi_0,\\ \phi_2-\phi_3-\phi_a+\Phi_{ext2} &= m\Phi_0.\end{aligned} \tag{87}$$

Here Φ_{ext1} and Φ_{ext2} are the external magnetic fluxes in the loops (see Fig. 28); n and m are the integer numbers of flux trapped in each loop, and Φ_0 is a flux quantum. The Hamiltonian of the circuit written in the terms of the branch flux and charge variables

$$H = \frac{q_r^2}{2C_r}+\frac{q_a^2}{2C_a}+\frac{1}{2L_r}\left(\phi_r-\phi_s\right)^2+\frac{1}{2L_s}\phi_s^2+\frac{1}{2L}\phi_1^2+\frac{1}{2L}\phi_2^2+\frac{1}{2L}\phi_3^2-E_J\cos\left(\varphi_a\right). \tag{88}$$

In the following calculations we use the notations $L = \frac{2}{3}L_a$, $L_\Sigma^2 = L_rL_a+L_rL_s+L_aL_s$. We define the flux gradient as $\Phi_d = (\Phi_{ext1}-\Phi_{ext2})/2+(m-n)/2$ and the residual flux $\Phi_\Sigma = (\Phi_{ext1}+\Phi_{ext2})/2+(m+n)/2$. We substitute ϕ_1 and ϕ_2 using the boundary conditions Eq. 87 and we find equations of motion for variables without dynamics ϕ_3 and ϕ_s:

$$\begin{aligned}\phi_3 &= \frac{1}{6L_\Sigma^2}\left(-4L_a\left(L_r+L_s\right)\phi+2L_aL_s\phi_r-3L_rL_s\left(\phi-\Phi_\Sigma\right)\right),\\ \phi_s &= \frac{1}{2L_\Sigma^2}\left(2L_aL_s\phi_r+L_rL_s\left(\phi+3\Phi_\Sigma\right)\right).\end{aligned} \tag{89}$$

These equations allow to eliminate dependent degrees of freedom and the Hamiltonian takes the form:

$$\begin{aligned}H =& \frac{q_r^2}{2C_r}+\frac{q_a^2}{2C_a}+\frac{L_a+L_s}{2L_\Sigma^2}\left(\phi_r-A\Phi_\Sigma\right)^2+\frac{L_r+L_s+\frac{3}{4}\frac{L_rL_s}{L_a}}{2L_\Sigma^2}\left(\phi_a-\Phi_d+B\Phi_\Sigma\right)^2\\ &-\frac{L_s}{2L_\Sigma^2}\phi_r(\phi_a-\Phi_d)-E_J\cos\left(\varphi_a\right)\end{aligned} \tag{90}$$

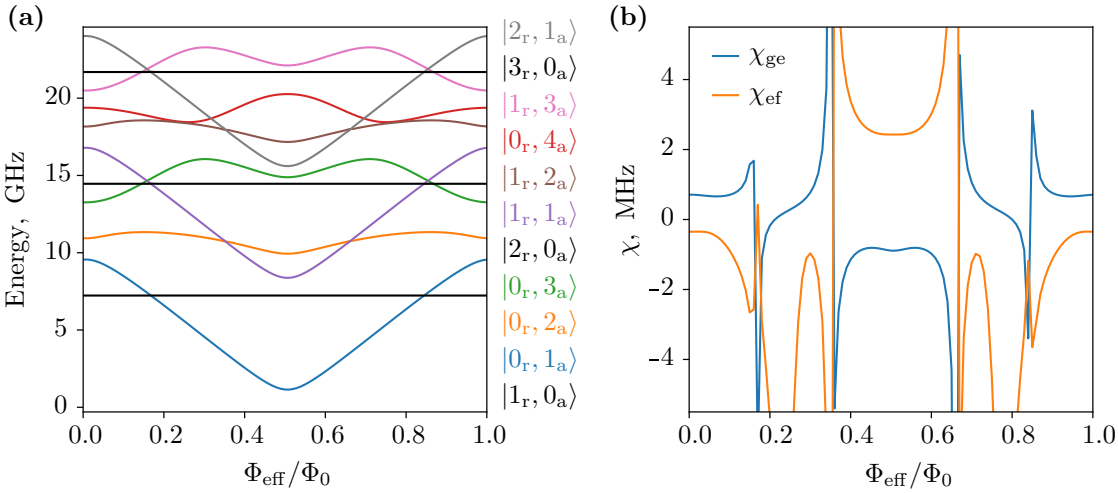

Figure 33: **The calculated target spectrum of the coupled atom-resonator circuit. (a)** Energy levels of the coupled gradiometric fluxonium atom and the readout resonator as function of the effective external magnetic field. The ground level is shifted to the zero energy. The effective field corresponds to the residual flux sensitivity of the atom (see section 2.6). The labels indicate number of photons in the resonator and the atom. **(b)** The dispersive shift of the readout resonator calculated for the first two atom transitions. At the $0.5\,\Phi_0$ flux bias, $\chi_{\mathrm{ge}} \approx -0.9\,\mathrm{MHz}$, while $\chi_{\mathrm{ef}} \approx 2.2\,\mathrm{MHz}$.

with the numerical coefficients

$$A = \frac{3}{2}\frac{L_\mathrm{s}}{L_\mathrm{a}+L_\mathrm{s}}, \quad B = \frac{3L_\mathrm{r}L_\mathrm{s}}{4L_\Sigma^2 - L_\mathrm{r}L_\mathrm{s}}. \tag{91}$$

The coefficient B is responsible for the residual flux sensitivity of the fluxonium atom. For the target circuit parameters listed in Table 1 $B \approx 0.5\%$, which corresponds to the expected factor 200 suppression of the fluxonium sensitivity to perpendicular magnetic field.

Target circuit parameters

The target circuit parameters are summarized in Table 2. We aim at the readout resonator frequency of 7.2 GHz. The atom capacitance C_a is defined by the size of the Josephson junction and by geometry of the connecting leads. The parallel plate capacitance can be calculated from an empirical expression $C_\mathrm{J} = 50\,\mathrm{fF}/\mu\mathrm{m}^2$. The Josephson junction area of $0.2{\times}0.25\,\mu\mathrm{m}^2$ yields $C_\mathrm{J} = 2.5\,\mathrm{fF}$. From the previous measurements of the non-gradiometric fluxonium atoms we estimate the total atom capacitance to be $C_\mathrm{a} \approx 5.0{-}6.0\,\mathrm{fF}$. The Josephson energy and the atom inductance are chosen in such way that the atom first transition frequency at the $0.5\,\Phi_0$ flux bias is around 1.1 GHz.

In order to achieve the optimal readout signal to noise ratio the dispersive shift of the readout resonator for the first atom transition $\chi_{\mathrm{ge}} = f_{\mathrm{r,e}} - f_{\mathrm{r,g}}$ at $\Phi_0/2$ bias should be equal to the resonator coupling rate κ. The dispersive shift depends on the value of the shared inductance and is calculated by diagonalizing the coupled atom-resonator Hamiltonian. We show that the Hamiltonian of the coupled gradiometric fluxonium can be reduced to the Hamiltonian of the non-gradiometric one with rescaled inductances and suppressed flux sensitivity (see section 2.6).

$C_\mathrm{r} = 20.2\,\mathrm{fF}$	$L_\mathrm{r} = 22.0\,\mathrm{nH}$	$L_\mathrm{s} = 2.0\,\mathrm{nH}$	$C_\mathrm{a} = 5.5\,\mathrm{fF}$	$L_\mathrm{a} = 250\,\mathrm{nH}$	$E_\mathrm{J} = 7.6\,\mathrm{GHz}$

Table 2: **Target circuit parameters for the gradiometric fluxonium coupled to the readout resonator.** C_r and L_r are the capacitance and the inductance of the readout resonator, respectively. L_s is the shared inductance. C_a and L_a are the capacitance and the equivalent atom inductance, respectively. E_J is the Josephson energy.

The Hamiltonian is solved in the bare harmonic oscillator basis, truncating the Hilbert space at 20 levels for the fluxonium and $n = 100$ levels for the resonator. Fig. 33 demonstrates spectrum of the gradiometric fluxonium with target parameters, and the dispersive shift of the resonator as function of the effective magnetic field (panels a and b, respectively).

2.6.1 Flux sensitivity suppression and flux trapping

We couple the gradiometric atom to the readout resonator by sharing part of the inductance in one loop. The coupling perturbs the distribution of electromagnetic fields and screening currents in the fluxonium loops. Therefore, there will be a residual flux sensitivity associated with the asymmetry of coupling. Assuming that the grAl film is homogeneous on the area of the fluxonium loop size ($50\times150\,\mu m^2$) and that the coupling is the only source of asymmetry in the fluxonium circuit, we expect the flux sensitivity to be suppressed by a factor ≈ 200 compared to the regular fluxonium (see section 2.6 for the coupled atom-resonator Hamiltonian).

We extract the flux sensitivity of the gradiometric atom from a single tone spectroscopy of the readout resonator coupled to the atom. The resonator frequency diverges at the points of the avoided crossings with the atomic $|g\rangle-|e\rangle$ transition. We compare the periodicity of the avoided crossings for the non-gradiometric and gradiometric atoms (see Fig. 34). The non-gradiometric atom with a known periodicity of one flux quantum was used to calibrate the applied magnetic field (panel a). The data shows that the flux sensitivity of the gradiometric atom is suppressed by factor of 120, which is in a good agreement with the expected residual sensitivity due to the atom coupling to the readout resonator. For other gradiometric fluxonium atoms we measure flux sensitivity suppression up to 180 times (see Fig. 35). I would like to mention that we can not distinguish contributions from inductance asymmetry and flux gradient in the loops (see eq. 85). The fact that we measure sensitivity suppression close to the expected value indicates a remarkable heterogeneity of the grAl film in the superinductance. The demonstrated suppression is 6−10 times higher than reported value for the (Nb,Ti)N

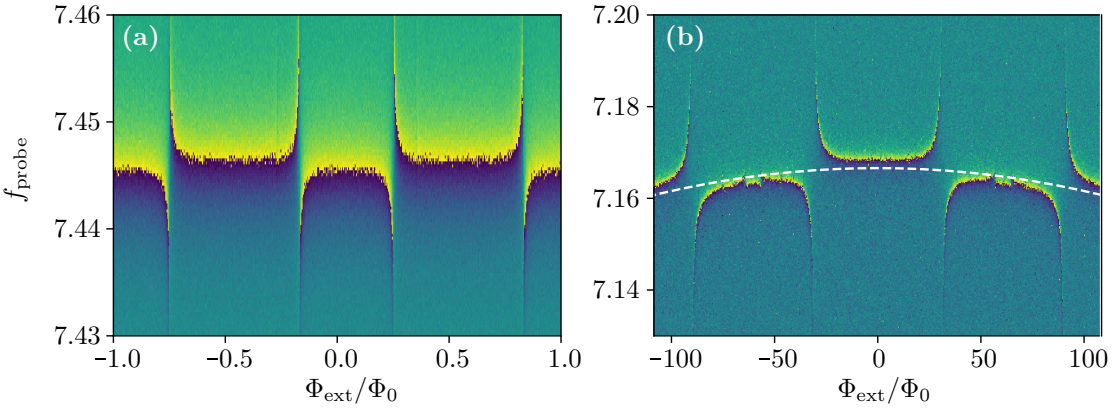

Figure 34: **Single tone spectroscopy of the two readout resonators coupled to the non-gradiometric and gradiometric atoms, respectively.** Both resonators were located on the same chip. The sample was cooled down in the magnetic field corresponding to one flux quantum in the outer loop of the gradiometric fluxonium. Color indicates the phase of the reflected signal. **(a)** Readout resonator coupled to the non-gradiometric fluxonium atom. The resonator frequency shows avoided crossings with the atomic $|g\rangle-|e\rangle$ transition. The avoided crossings are repeated with a period of one flux quanta in the fluxonium loop, which corresponds to the magnetic field of 0.28 µT. **(b)** Readout resonator coupled to the gradiometric fluxonium atom. Φ_{ext} corresponds to the flux threading the outer loop of the gradiometric fluxonium. The flux sensitivity of the gradiometric atom is suppressed by 120 times compared to the non-gradiometric one. The white dashed line is a fit of the readout resonator frequency. The shape of the avoided crossings indicates that the gradiometric fluxonium was pinned at the half flux quanta bias by the trapped flux (minimum of the fluxonium frequency at the zero applied flux).

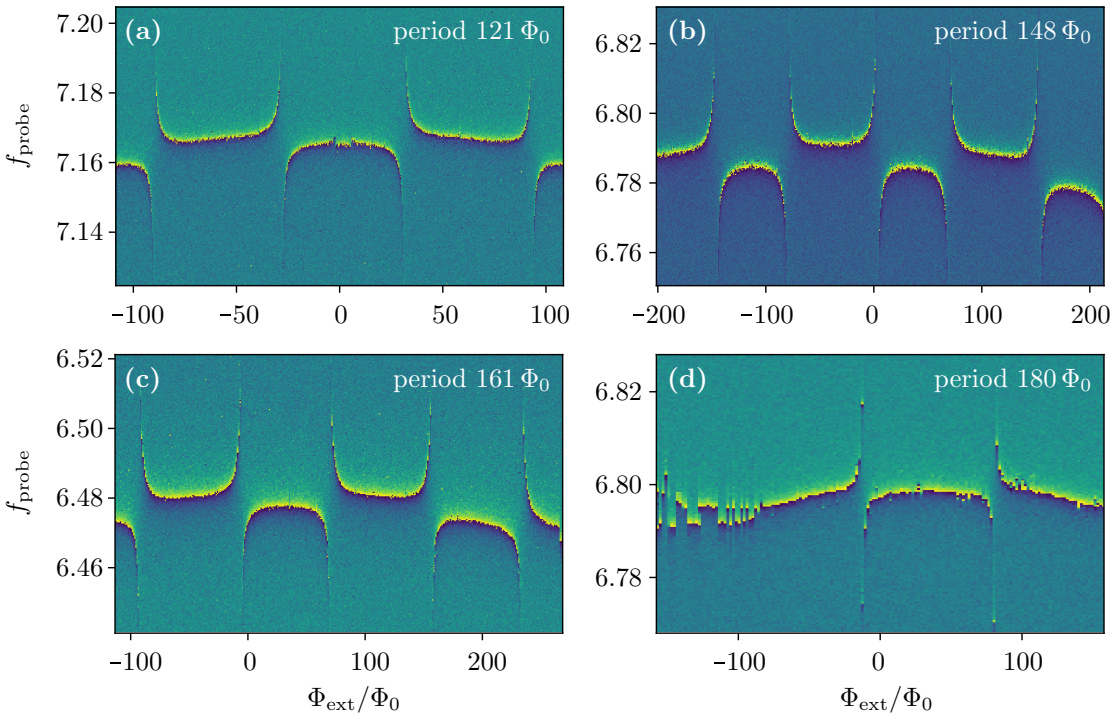

Figure 35: **Single tone spectroscopy of the readout resonators coupled to gradiometric atoms.** Flux sensitivity suppression corresponds to the periodicity of the resonator avoided crossings compared to the periodicity of resonators coupled to non-gradiometric atoms located on the same chip. Labels indicate calculated periodicity. Panel (a) shows gradiometric fluxonium cooled down in zero magnetic field, as $\Phi_{\mathrm{ext}} = 0$ corresponds to maximum of the atom frequency. For atom in panel (d) phase slip events prevent from measuring complete spectrum, therefore several plots were combined to extract periodicity.

gradiometric fluxonium [Pit+20].

For all the gradiometric atoms we observe a decrease of the coupled readout resonator frequency with increasing flux threading the fluxonium loop. Resonators coupled to non-gradiometric atoms do not demonstrate such dependence. We associate the decrease of the resonator frequency with the circulating current generated by the magnetic field in the fluxonium loop. The kinetic inductance dependence on the current can be approximated with $L_{\mathrm{kin}} \approx L_{\mathrm{kin0}}\left(1+I^2/I_{\mathrm{c}}^2\right)$ [Lev+19], where I_{c} is the critical current. The current flowing through the shared inductance changes the total inductance of the resonator. The resonator frequency is therefore

$$f_{\mathrm{r}} = \sqrt{L_{\mathrm{r}}C_{\mathrm{r}}+L_{\mathrm{s}}\left(1+\frac{I^2}{I_{\mathrm{c}}^2}\right)C_{\mathrm{r}}}^{-1} = f_{\mathrm{r0}}\sqrt{1+\frac{L_{\mathrm{s}}}{L_{\mathrm{r}}+L_{\mathrm{s}}}\frac{I^2}{I_{\mathrm{c}}^2}}^{-1}, \tag{92}$$

with $f_{\mathrm{r0}} = \sqrt{(L_{\mathrm{r}}+L_{\mathrm{s}})C_{\mathrm{r}}}^{-1} \approx 7.167\,\mathrm{GHz}$. From the numerical fit of the resonator frequency we obtain the critical current density $j_{\mathrm{c}} \approx 0.8\,\mathrm{mA/\mu m^2}$ which is of the same order as previously reported value for the grAl films [Mal+18].

The gradiometric fluxonium was pinned at the degeneracy point by cooling down in magnetic field of one flux quantum threading the fluxonium outer loop. Fig. 34 b shows the corresponding spectrum of the readout resonator, the shape of the avoided crossings indicates that the atom minimum frequency is at zero of the applied magnetic field. Notice, that for the non-gradiometric atom zero magnetic field corresponds to the maximum of atom frequency (panel a). For comparison, the readout resonator spectroscopy for the gradiometric fluxonium with zero trapped flux is shown in Fig. 35 a.

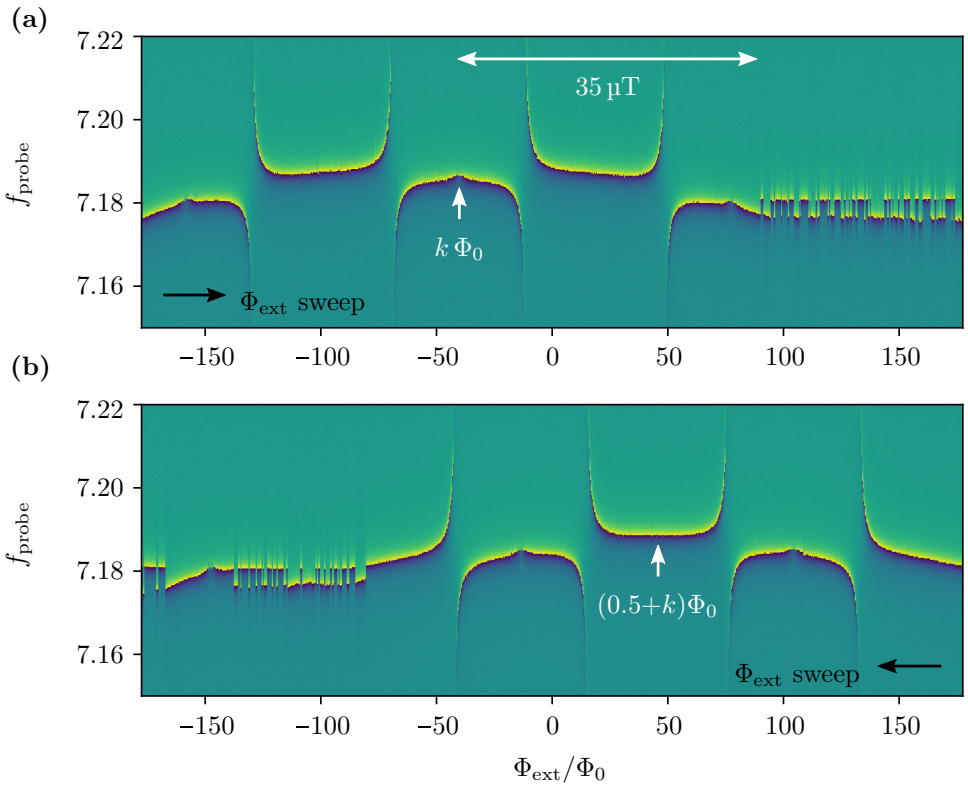

Figure 36: **Current activated trapped flux escape.** Single tone spectroscopy of the readout resonator coupled to the gradiometric fluxonium atom vs applied magnetic field. Resonator is measured in reflection, color indicates the phase of the output signal. Panels a and b correspond to the consecutive sweeps of the magnetic field in opposite directions. White arrows show the flux values at which the circulating current in the fluxonium loop is minimal. Labels indicate the effective fluxonium bias with integer and half-integer flux quanta (panel a and b, correspondingly). Jumps of the resonator frequency observed starting from $\approx 35\,\mu\text{T}$ detuning from the indicated flux biases reflect phase slips in the fluxonium loop.

2.6.2 Trapped flux escape

We observe current-activated trapped flux escape while performing single and two-tone (see section 2.6.2) resonator spectroscopy when the applied magnetic field is detuned by $\approx 35\,\mu\text{T}$ from the field corresponding to the minimal circulating current in the trapping loop (see Fig. 36). This value is one order of magnitude smaller than the reported value for the magnetic field $B_\perp$ at which, presumably, fluxon trapping in the grAl resonators occurs (see Ref. [Bor+20]). In our design the fluxonium trapping loop has sections made out of sandwiched layers of aluminum and grAl, therefore the critical magnetic field should be lower than for pure grAl circuits. At high circulating currents dissipation in the microscopic defects present in the aluminum and grAl films can cause local suppression of superconductivity. A decrease of the tunneling potential for the trapped flux favors phase slips in the grAl loop. The process of phase slip is stochastic, and the number of tunneling flux quanta is uncontrollable.

Surprisingly, we also observe the decay of the trapped flux with time. The trapped flux escapes the grAl loop within a few hours after cooldown even when the applied magnetic field is ramped down to zero. We estimate the expected flux lifetime by modeling the grAl loop with a chain of effective Josephson junctions [Mal+18]. The phase slip rate in the chains is defined with eq. 20, and depends on the Josephson and charging energies of the individual junctions. For grAl films with thickness smaller than the London penetration depth $\lambda_{\text{L}} \geq 0.4\,\mu\text{m}$ the superconducting current density is uniform across the film cross-section. Therefore we can divide the grAl wire into fictitious superconducting sections with length equal to the grain size, and area corresponding to the wire cross-section. Each section plays a role of the Josephson junction electrode, and the parallel plate capacitance C_{J} of the effective junction equals the summed

capacitance of the grains in the cross-section.

For grAl wires with thickness of 50 nm and width 160 nm we calculate the $C_J = 0.4\,\text{fF}$ using the empirical value $\sim 50\,\text{fF}/\mu\text{m}^2$ for capacitance per area [FD87; Gee+89; KH91]. The capacitive energy is then $E_C = e^2/2C_J \approx 48\,\text{GHz}$. We assume that the typical size of aluminum grains in grAl is $\sim 4\,\text{nm}$ and find the number of the effective Josephson junctions in the outer loop $N \approx 75{\times}10^3$. From the total grAl inductance we calculate the linear inductance of the effective junctions $L_{J0} = L_{\text{grAl}}/N$, and the Josephson energy $E_J = (\Phi_0/2\pi)^2/L_{J0} \approx 53\,\text{THz}$. Substitution of these values into eq. 20 gives phase the slip rate $\sim 10^{-22}\,\text{Hz}$, once in hundred trillion years. Since the effective area of the junction electrodes can be larger due to the granular structure of the material, this estimation gives an upper limit for the phase slip rate.

This calculation shows that we can not explain the observed flux decay by tunneling through the Josephson potential, and the origin of the observed phase slips remains unclear. We suspect that strong radiation impacts which generate non-equilibrium quasiparticles can suppress superconductivity in circuits and cause flux decay. To test this hypothesis one can measure correlations between the flux escape events for several fluxonium atoms on the same chip, similar to the experiment on observation of quasiparticle bursts in grAl resonators [Car+21]. The result of such experiment can be of great practical importance since phase slips undermine the stability of the quantum devices and hinder application of the surface error correction codes. Circuits based on the trapped fluxons (e.g. [Pet+18]) might need fast flux injection to correct for the flux escape errors.

Measured spectrum of the gradiometric fluxonium

We perform the two-tone spectroscopy to measure the transition frequencies of the gradiometric fluxonium. Fig. 37 a shows the measured $|g\rangle{-}|e\rangle$ and $|g\rangle{-}|f\rangle$ transition frequencies and the numerical fit of the spectrum. It is important to mention that two tone spectroscopy usually takes a few hours, and we routinely observed trapped flux escapes during the measurement. The fluxonium spectrum shifts uncontrollably along x-axis with each flux escape. Therefore Fig 37 a shows data collected in several measurements, flux shifts between data sets were corrected to plot the combined spectrum. From the numerical fit, we extract the fluxonium circuit parameters $E_J = 5.1\,\text{GHz}$, $C_a = 3.4\,\text{fF}$, and $L_a = 172\,\text{nH}$. The parallel plate capacitance of the Josephson junction with size $0.2{\times}0.2\,\mu\text{m}^2$ contributes $C_J \approx 2.0\,\text{fF}$, the rest of the atom capacitance is given by the connecting leads and the self-capacitance of the loops. Assuming that L_a is dominated by the kinetic inductance, we find the grAl film kinetic inductance per square $L_{\text{kin}} = 0.12\,\text{nH}/\square$, and calculate the film resistivity $\rho \approx 900\,\mu\Omega\,\text{cm}$ (see eq. 16), which is in the vicinity of the superconducting dome maximum [Pra+16; Lev+19].

Fig 37 b demonstrates the calculated spectrum of the coupled atom-resonator Hamiltonian using circuit parameters extracted from single and two-tone spectroscopy of the readout resonator. The value of the shared inductance $L_s = 2.8\,\text{nH}$ is obtained from the fit of the measured dispersive shift $\chi_{ge}(0.5\,\Phi_0) = -7.8\,\text{MHz}$. We find the χ_{ge} by measuring the readout resonator frequency when the atom is in the thermal equilibrium state and by taking the difference with the resonator frequency when the atom is reset to the inverse thermal state by the π-pulse. The thermal atom population can be found from the Boltzmann distribution:

$$\frac{p_e}{p_g} = \exp\left(-\frac{hf_{ge}}{k_B T}\right). \tag{93}$$

For the first atom transition frequency $f_{ge} = 3.84\,\text{GHz}$ the thermal excitation at the fridge temperature 20 mK is negligible ($p_e \sim 0.01\%$) and the measured χ_{ge} can be used without rescale. The dispersive shift is calculated by diagonalizing the coupled atom-resonator Hamiltonian (see section 2.6). The measured dispersive shift is 8 times larger than the target one, which might be due to coupled atom-resonator levels structure, as virtual transitions between higher levels affect the resonator dispersive shift.

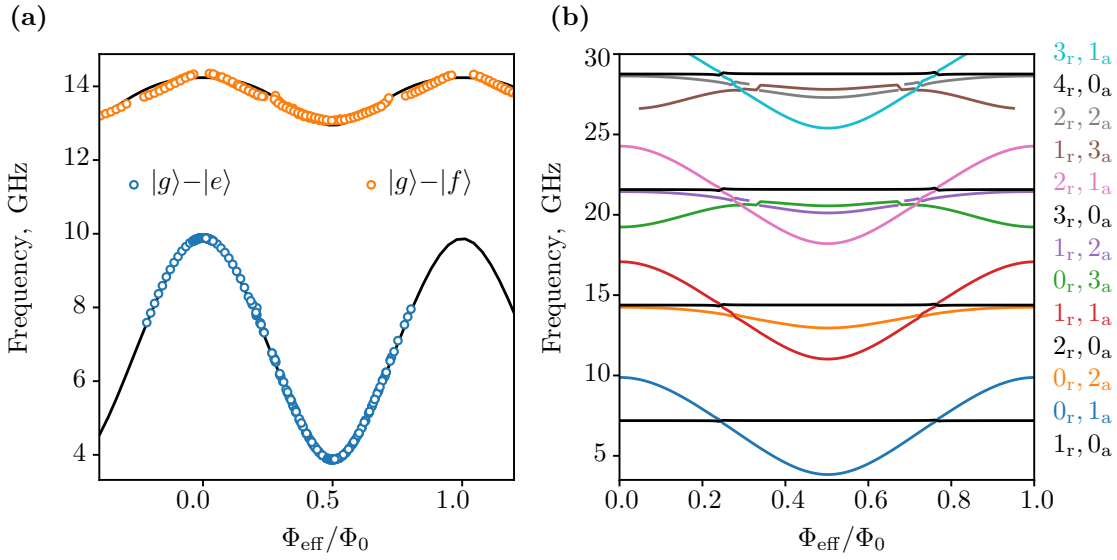

Figure 37: **Gradiometric fluxonium spectrum.** **(a)** Markers indicate $|g\rangle - |e\rangle$ and $|g\rangle - |f\rangle$ transition frequencies extracted from the two-tone spectroscopy. Φ_{eff} corresponds to the effective flux bias of the atom. The black lines show the fit of the spectrum to the energy levels of the uncoupled atom, from which we extract $E_J = 5.1\,\text{GHz}$, $C_a = 3.4\,\text{fF}$, and $L_a = 172\,\text{nH}$. **(b)** The calculated levels of the coupled atom-resonator Hamiltonian. We use the atom circuit parameters extracted from the two-tone spectroscopy and the measured dispersive shift to extract the value of the shared inductance $L_s = 2.8\,\text{nH}$. The resonator inductance $L_r = 21.6\,\text{nH}$ is calculated from the measured resonator frequency $f_{r0} = 7.167\,\text{GHz}$ and the simulated capacitance $C_r = 20.2\,\text{fF}$ using $f_{r0} = \sqrt{(L_r + L_s)C_r}^{-1}$. Interruptions and discontinuity in the calculated spectrum, visible for levels $|0_r, 3_a\rangle$, $|1_r, 2_a\rangle$, $|1_r, 3_a\rangle$, and $|2_r, 2_a\rangle$, correspond to flux values at which the level sorting procedure fails.

2.6.3 Energy relaxation time and coherence

For the gradiometric atom initialized at the degeneracy point by cooling down in a static magnetic field of one flux quantum in the outer loop, we measure the energy relaxation time T_1, the Ramsey coherence time T_2^* [Ram50], and the Hahn-echo coherence time T_2 [Hah50]. For the free decay T_1 experiment we apply a π-pulse of 30 ns duration calibrated by measuring Rabi oscillations between atom $|g\rangle$ and $|e\rangle$ states. The atom excited state decays during a variable time delay, and the resulting atom population is detected with a 800 ns readout pulse. At the degeneracy point, $T_1 \approx 11.7\,\mu\text{s}$ (see Fig. 38 a). This value is twenty times smaller than the Purcell relaxation time calculated numerically for the measured resonator coupling to the environment $\kappa = 3.0\,\text{MHz}$ using eq. 82. We intended to measure T_1 as function of the applied field around the degeneracy point, but measurement was interrupted by the trapped flux escape. The histogram of collected T_1 measured in the $[-0.2\,\Phi_0, -0\,\Phi_0]$ flux interval is shown in Fig. 38 b. T_1 fluctuates within 9% around the average value of 12.7 µs.

Fig. 39 a shows Ramsey coherence time measured at the degeneracy point (markers). The coherence time is extracted from a fit to the data with an exponentially damped cosine function. Coherence time can be improved by almost an order of magnitude by filtering out slow flux noise in the Hahn-echo experiment (see Fig. 39 b). The pulse sequence is similar to the Ramsey experiment (see Fig.25), but with one π pulse inserted in the middle between the two $\pi/2$ pulses. It results in cancelling slow phase accumulation by the atom state during free evolution. We also measure Ramsey T_2^* as function of the applied magnetic field in the interval $\pm 0.8\,\Phi_0$ around the atom degeneracy point (see Fig. 39 c). It corresponds to $\pm 0.7\%$ detuning relative to the total $120\,\Phi_0$ flux periodicity of the atom. Therefore, the parabolic dependence of the atom frequency is visible (orange markers).

The atom coherence time does not improve in the vicinity of the degeneracy point, as was observed in the single-loop fluxonium in even smaller flux interval ($\pm 0.05\%$ of atom periodicity)

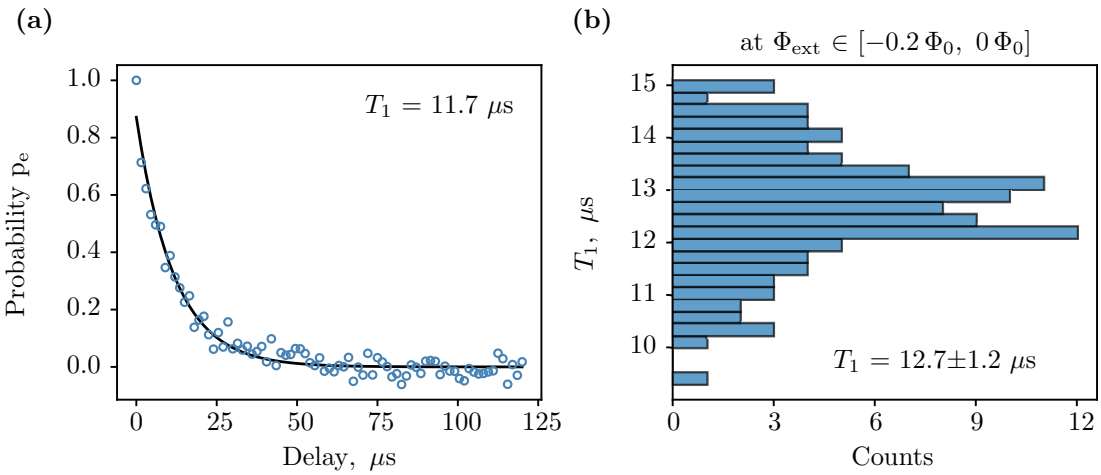

Figure 38: **Atom energy relaxation time.** **(a)** T_1 measured at the gradiometric atom degeneracy point (markers). The black line is an exponential fit. **(b)** A histogram of the energy relaxation times measured at the applied magnetic fields in the interval $[-0.2\,\Phi_0, -0\,\Phi_0]$ around the degeneracy point.

[Grü+19]. For non-gradiometric atom with comparable dispersive shift and located on the same chip we measure Ramsey coherence $T_2^* = 0.6{-}1.8\,\mu s$, and Hanh-echo $T_2^* \approx 2.5\,\mu s$. This fact in combination with T_2 enhancement in Hahn echo experiment indicates that the coherence of both fluxonium atoms is probably limited by local low frequency flux noise, which origin is still unclear. We expect that coherence time should increase for more compact atoms with smaller loops. Additionally, the dispersive shift has to be decreased to reduce the photon shot noise.

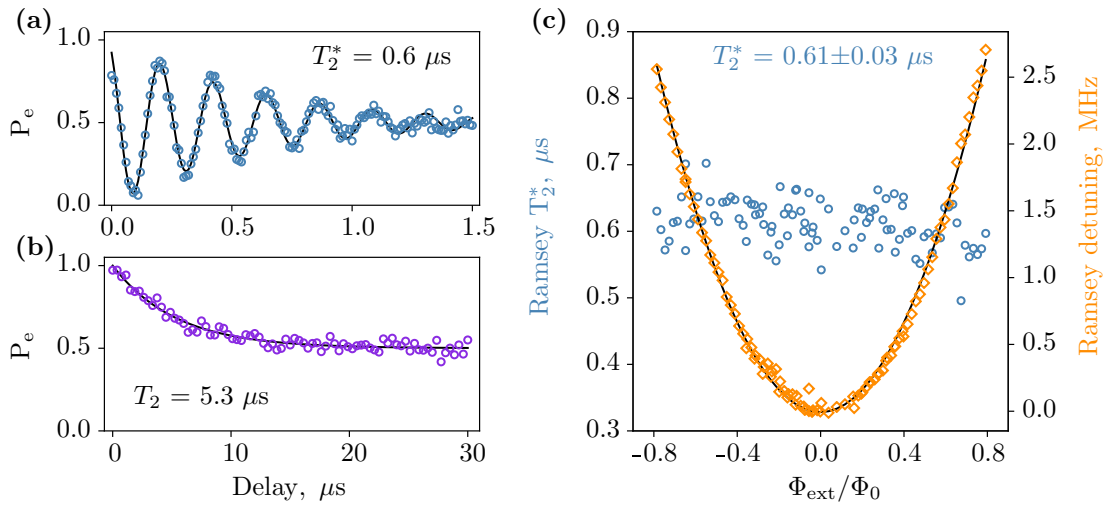

Figure 39: **Gradiometric atom coherence.** **(a)** Ramsey coherence time T_2^* measured at the gradiometric atom degeneracy point (markers). The black line is a fit with exponentially damped cosine function. **(b)** Hahn-echo coherence time. **(c)** Ramsey T_2^* measured as function of the applied magnetic field (blue markers). Orange markers show the change of the fluxonium frequency $f_{ge}(\Phi_{ext}) - f_{ge}(0.5\Phi_0)$, the black line is a parabolic fit.

3 Longitudinal interaction

The longitudinal readout relies on the coupling of the qubit's σ_z degree of freedom to the resonator's transversal degree of freedom

$$H_{\mathrm{int}} = g_{zx}\sigma_z \left(a^\dagger + a\right), \tag{94}$$

where the subscript zx denotes that coupling is longitudinal in respect to the qubit, and transverse in respect to the readout resonator. The longitudinal interaction Hamiltonian commutes with the qubit observable, and is purely QND in contrast to the dispersive Hamiltonian. Hence, there is there is no Purcell enhancement of the qubit relaxation rate and during the interaction the qubit and the resonator states get entangled without inducing qubit transitions.

The qubit can be seen as an effective force acting on the readout resonator. During the ring up the coherent resonator pointer states corresponding to the qubit's $|0\rangle$ and $|1\rangle$ states follow the imaginary axis in the phase space in the rotating frame. Therefore, the signal to noise ratio grows faster at the short integration times compared to the dispersive measurement [DBB15]

$$\mathrm{SNR}_{zx} \propto \mathrm{SNR}_{xx}/\kappa\tau_{\mathrm{m}}, \tag{95}$$

for $\kappa\tau_{\mathrm{m}} \ll 1$. The qubit-state dependent displacement of the resonator field between the pointer states is $\pm g_{zx}/(\omega_{\mathrm{r}} + i\kappa/2)$ (see Ref. [DBB15]), which is typically too small to resolve the qubit states if $\omega_{\mathrm{r}} \gg g_{zx}, \kappa$. The displacement can be enhanced by modulating the coupling strength at the readout resonator frequency $g_{zx}(t) = \bar{g}_{zx} + \tilde{g}_{zx}\cos(\omega_{\mathrm{r}} t)$ as was proposed in Ref. [DBB15]. The resulting displacement becomes orders of magnitude larger $\pm\tilde{g}_{zx}/i\kappa$. The qubit state can be detected by measuring the resonator quadrature response with homodyne or heterodyne measurement schemes.

The total qubit-resonator Hamiltonian can be diagonalized exactly via Lang-Firsov unitary transformation $U = \exp\{-(g_{zx}/\omega_{\mathrm{r}})\sigma_z \left(a^\dagger + a\right)\}$ yielding [BTN15]

$$H' = \omega_{\mathrm{r}} a^\dagger a + \frac{\omega_{01}}{2}\sigma_z - \frac{g^2}{\omega_{\mathrm{r}}}\mathbb{1}. \tag{96}$$

From this equation follows that the resonator and qubit frequencies are not affected by the interaction, and the only effect of coupling is the rescale of the zero point fluctuations. This implies that the longitudinal interaction is QND irrespective of the detuning between the qubit and the resonator, and both the coupling strength and the readout power can be large without degrading the QNDness. This fact allows to construct scalable quantum architectures without residual couplings [BTN15; RD16a]. It was shown that in a particular grid of qubits coupled longitudinally to resonators the coupling can be strictly confined to nearest and next-nearest resonators. The grid Hamiltonian has no dispersive shifts and residual qubit-qubit couplings. Additionally, all qubits can have the same frequency, which solves the multiplexing problem for large-scale quantum circuits. Dispersive coupling can also be used to realize the resonator-mediated interaction between qubits [Maj+07]. However, neglected terms in the expansion of the dispersive coupling lead to residual direct qubit-qubit interactions. The frequency of each qubit depends on the state of the other one, which leads to a constant accumulation of phase during free evolution [BTN15]. In addition, the speed of the two-qubit gates is limited by the coupling strength which has to be smaller than the detuning between resonator and qubit frequencies.

The longitudinal coupling schemes were already proposed for transmons and gradiometric flux qubits [Ker13; BTN15; DBB15]. They rely on symmetries to cancel spurious transverse couplings which sets high requirements to fabrication techniques. Here we present our unpublished results on the way towards implementation of the transmon qubit with tunable transverse and longitudinal coupling following the proposal of S. Richer *et. al* [RD16a; Ric+17].

3.1 Inductively shunted transmon qubit

The equivalent circuit diagram of the proposed inductively shunted transmon that is coupled to an embedded harmonic mode is depicted in Fig. 40 a. The detailed analysis of the circuit and its extension to scalable architecture can be found in [Ric+17; Ric18]. The qubit (shown in blue) consists of a single Josephson junction with energy E_{Jq} shunted by a capacitance C_{q}. The resonator (black) is built in a shape of two branches. Each branch contains a capacitance C, a linear inductance L, and a Josephson junction array connected in parallel. The qubit junction and inductances form a closed loop, providing the inductive shunt which protects the qubit from charge noise. The resonator branch design is further modified by adding another inductance as shown in Fig. 40 b. This allows to find the circuit parameters with desired balance between the resonator and qubit anharmonicities and the coupling terms.

In the symmetric case when the capacitances and inductances in the two branches are equal, the transverse capacitive and inductive couplings cancel out. The qubit and resonator modes are coupled only via the Josephson junction arrays. The transverse coupling is zero if the Josephson energies E_{J1} and E_{J2} in the two branches are equal, therefore a few percent asymmetry between the junctions is introduced to keep transverse coupling. With the number k of junctions in the array the coupling strength can be varied. Increasing k results in suppression of the resonator nonlinearity and the higher order coupling terms.

The circuit can be biased by the external magnetic field (red labels). The flux enclosed in the coupling loops formed by the junction array and branch inductance Φ_{x} is used to tune between pure longitudinal and pure transverse coupling. Flux in the big loop Φ_{xb} causes slow variation of the coupling terms and can be used to enhance the coupling and qubit anharmonicity at $\Phi_{\mathrm{xb}} = \Phi_0/2$ bias. The improved version of the resonator branch design is shown in Fig. 40 b. Adding an inductance L_{a} in series with both the junction array and inductance L allows to simultaneously increase the qubit anharmonicity and g_{zx} coupling, and suppress the resonator's anharmonicity.

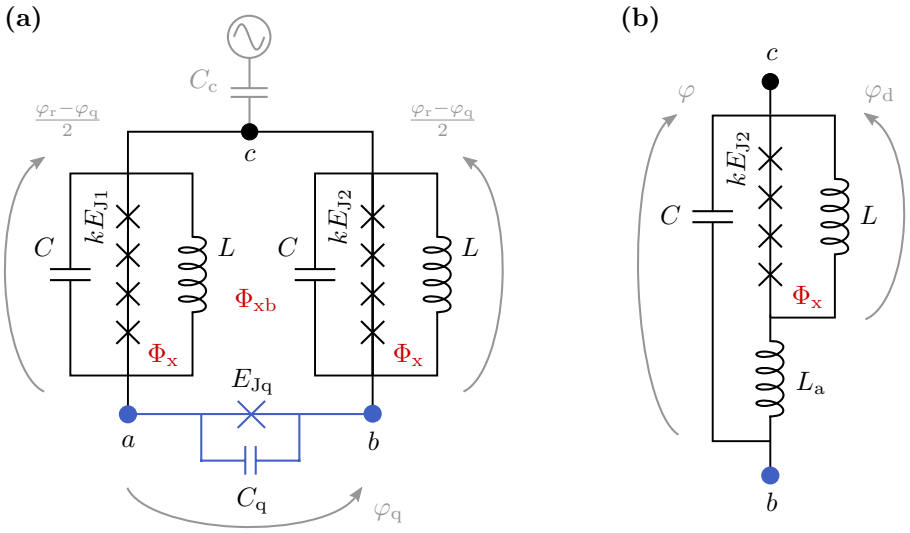

Figure 40: **Inductively shunted transmon qubit. (a)** The basic circuit schematic. Transmon qubit and an embedded resonator are shown in blue and black, respectively. The resonator mode couples to the external electric field via the coupling capacitance C_{c}. The resonator has two branches, each consisting of a linear inductance L, the capacitance C and the Josephson junction array connected in parallel. The Josephson energy for the left and the right branches is E_{J1} and E_{J2}, respectively. The applied magnetic field creates flux Φ_{xb} in the big loop, and the fluxes Φ_{x} in the coupling loops (red labels). **(b)** The improved branch design. The inductance L_{a} is added in series to the junction array and inductance L to increase the longitudinal coupling strength. The phase across the junction array φ_{d} has no internal dynamics and therefore can be expressed via the phase φ across the branch.

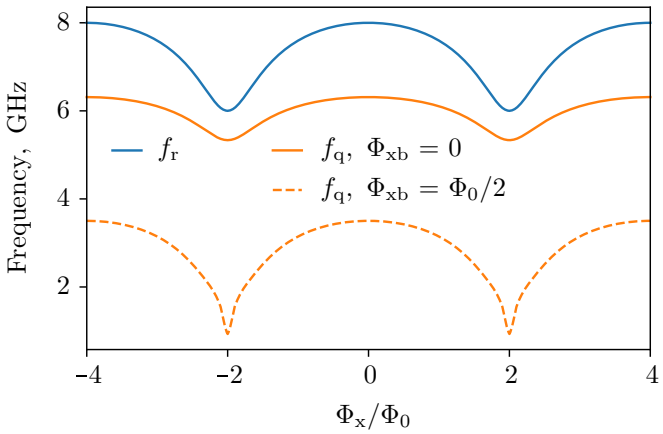

Figure 41: **Spectrum of tunable transmon and embedded resonator mode vs. Φ_x.** The circuit parameters are listed in Table 3. Resonator frequency is shown in blue. Orange lines correspond to the qubit frequency for $\Phi_{xb} = 0$ (solid) and $\Phi_{xb} = \Phi_0/2$ (dashed), respectively. Resonator frequency does not depend on Φ_{xb}.

From the circuit diagram we can derive the analytical expressions for the coupling terms, resonator and qubit frequencies and anharmonicities. The circuit has two independent degrees of freedom φ_q and φ_r, introduced as shown in Fig. 40 a (grey arrows). The circuit kinetic energy is

$$T = \left(\frac{\Phi_0}{2\pi}\right)^2 \left(\frac{2C_q+C}{4}\dot{\varphi}_q^2+\frac{C}{4}\dot{\varphi}_r^2\right) \tag{97}$$

while the potential energy is

$$\begin{aligned} U = &\left(\frac{\Phi_0}{2\pi}\right)^2 \frac{1}{4L}(\varphi_q^2+\varphi_r^2)-E_{Jq}\cos(\varphi_q+\varphi_{xb}) \\ &-kE_{J1}\cos\left(\frac{\varphi_r+\varphi_q}{2k}+\frac{\varphi_x}{k}\right)-kE_{J2}\cos\left(\frac{\varphi_r-\varphi_q}{2k}+\frac{\varphi_x}{k}\right) \end{aligned} \tag{98}$$

Trigonometric expansion and a series approximation of the potential energy up to second order in both φ_q and φ_r leads to four coupling terms

$$\begin{aligned} \hbar g_{xx}\sigma_x\left(a^\dagger+a\right) &= \frac{E_{J\Delta}}{4k}\varphi_q\varphi_r\cos\left(\frac{\varphi_x}{k}\right), \\ \hbar g_{zx}\sigma_z\left(a^\dagger+a\right) &= -\frac{E_{J\Sigma}}{16k^2}\varphi_q^2\varphi_r\sin\left(\frac{\varphi_x}{k}\right), \\ \hbar g_{xz}\sigma_x\left(a^\dagger+a\right)^2 &= -\frac{E_{J\Delta}}{16k^2}\varphi_q\varphi_r^2\sin\left(\frac{\varphi_x}{k}\right), \\ \hbar g_{zz}\sigma_z\left(a^\dagger+a\right)^2 &= -\frac{E_{J\Sigma}}{64k^3}\varphi_q^2\varphi_r^2\cos\left(\frac{\varphi_x}{k}\right), \end{aligned} \tag{99}$$

where $E_{J\Delta} = E_{J1}-E_{J2}$, and $E_{J\Sigma} = E_{J1}+E_{J2}$. The first two terms are the desirable g_{xx} dispersive, and g_{zx} longitudinal couplings which have out of phase modulation with the external magnetic field. This allows to achieve pure transverse and longitudinal coupling by proper flux bias. The last two terms correspond to the unwanted g_{xz} and g_{zz} couplings which have to be suppressed. Notice that the coupling terms transverse with respect to the qubit are proportional to $E_{J\Delta}$ while longitudinal ones are proportional to $E_{J\Sigma}$. The equations also show suppression of the higher order coupling terms with number of junctions, k.

The circuit with additional inductance has another phase variable φ_d (see Fig. 40 b) which can be eliminated using equations of motion. However, there is no analytical solution for φ_d, and calculations are done numerically. The resonator frequency and anharmonicity as functions of the external magnetic field are obtained by a series expansion of the circuit Hamiltonian around $\varphi_r = 0$ for fixed $\varphi_q = 0$. A similar strategy is applied for the qubit. The calculated

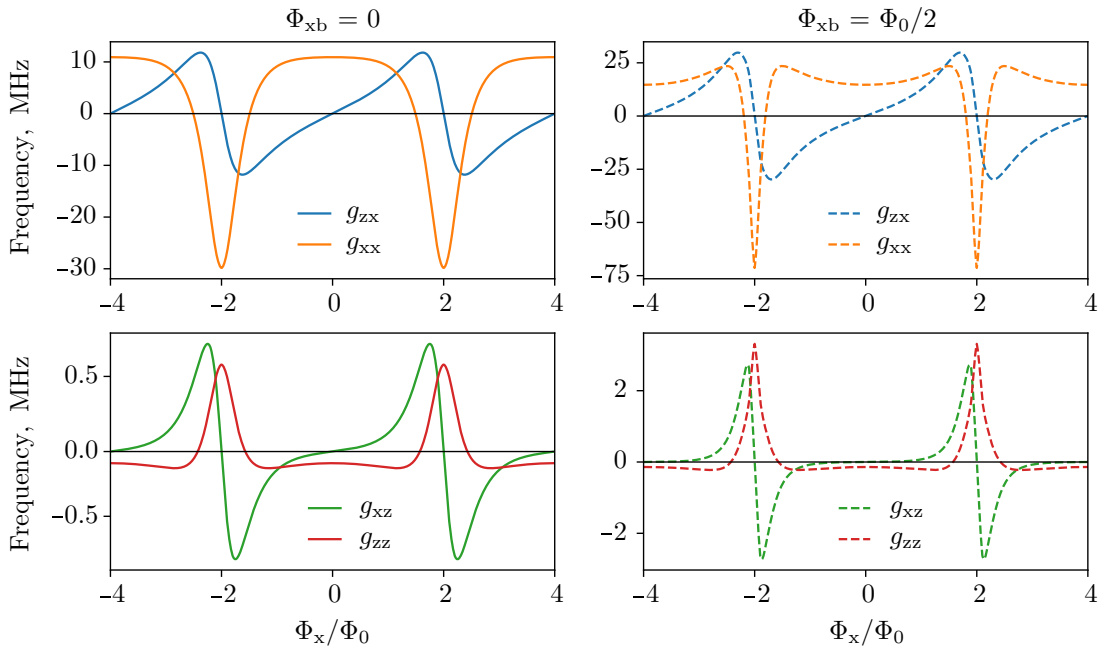

Figure 42: **Coupling terms vs. Φ_x.** The top panels show the desired coupling terms g_{zx} (blue) and g_{xx} (orange). The bottom panels show the unwanted g_{xz} (green) and g_{zz} (red). Solid and dashed lines correspond to $\Phi_{xb} = 0$ and $\Phi_{xb} = \Phi_0/2$, respectively.

spectrum of the resonator and qubit for the circuit with additional inductance is shown in Fig. 41. The circuit parameters are listed in Table 3. The number of Josephson junctions per coupling array is $k = 4$. At zero magnetic flux the resonator frequency is $f_r = 8.0\,\text{GHz}$. Flux in the coupling loops Φ_x causes modulation of the resonator and qubit frequencies with period $k\Phi_0$. The circuit parameters are selected such that the resonator frequency lies in the pass band of the 3D waveguide (from 6.0 GHz to 8.1 GHz) which is used as a controlled microwave environment for the circuit. The qubit frequency can also be tuned by magnetic flux in the big loop Φ_{xb} while the resonator is insensitive to Φ_{xb}. Orange solid and dashed lines depict qubit frequency at $\Phi_{xb} = 0$ and $\Phi_{xb} = \Phi_0/2$, correspondingly. In our design Φ_x and Φ_{xb} are not controlled independently, therefore tuning Φ_x within few flux quanta corresponds to a slow variation of Φ_{xb}. However, we can neglect this variation for the large loop area ratio and treat Φ_{xb} as fixed parameter.

Fig. 42 demonstrates the calculated coupling terms as functions of Φ_x. The top and bottom panels show the desired (g_{xx} and g_{zx}) and unwanted (g_{xz} and g_{zz}) coupling terms, respectively. At the flux bias points corresponding to pure transverse and longitudinal coupling the unwanted coupling terms are suppressed to 5−7% of g_{xx} and g_{zx}. The solid and dashed lines correspond to $\Phi_{xb} = 0$ and $\Phi_{xb} = \Phi_0/2$, respectively. Biasing the circuit at $\Phi_{xb} = \Phi_0/2$ allows to increase the coupling strength. Notice that the coupling terms are not sinusoidal functions of Φ_x as expected from the analytical expressions in eq. 99, due to the effect of the additional inductance. Nevertheless, zeros of transverse couplings are close to maxima of longitudinal ones (in absolute value), and vice versa. Crucially, in order to reach pure longitudinal coupling regime one has to bias the coupling loop with more than one flux quantum. It is possible only if phase slips in the junction arrays are suppressed. We require the ratio between Josephson energy and charging energy of the individual junctions in the array $E_j/E_c \geq 150$. The expected phase slip rate calculated using eq. 20 for four junctions in the array is $\sim 0.6\,\text{mHz}$.

The calculated relative anharmonicities $\alpha_r = (E_{12} - E_{01})/E_{01}$ of the resonator and qubit are

$E_{Jq} = 7.5\,\text{GHz}$	$E_{J1} = 75\,\text{GHz}$	$E_{J2} = 0.95\ E_{J1}$	$k = 4$
$C = 68.7\,\text{fF}$	$C_q = 50\,\text{fF}$	$L = 4\,\text{nH}$	$L_a = 3\,\text{nH}$

Table 3: **Tunable transmon circuit parameters.**

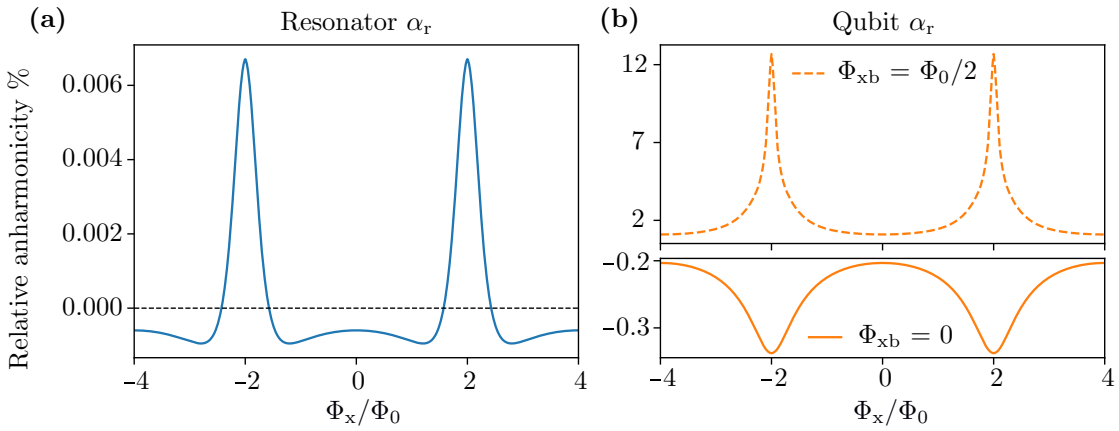

Figure 43: **Relative anharmonicity of resonator and qubit vs. Φ_x.** The resonator anharmonicity (blue) vanishes in points with pure longitudinal coupling, and does not depend on Φ_{xb}. The qubit anharmonicity can be increased by more than an order of magnitude by tuning from $\Phi_{xb} = 0$ to $\Phi_{xb} = \Phi_0/2$.

shown in Fig. 43. The resonator anharmonicity is cancelled for values of Φ_x at which the transverse coupling terms vanish. This directly reflects the absence of dispersive shift in circuits with pure longitudinal coupling. Qubit anharmonicity at $\Phi_{xb} = 0$ (solid orange line) is close to the typical transmon value $\alpha_r \approx -E_c/E_{01}$, while it can be increased up to 13% at $\Phi_{xb} = \Phi_0/2$ (dashed orange line).

3.2 Circuit implementation

Fig. 44 demonstrates the tunable transmon circuit implementation. We adapt the circuit for a 3D waveguide architecture (see section 5.2). The superconducting structure is located in the center of a $10\times15\,\mathrm{mm}^2$ sapphire chip. Three large aluminum pads shown in green form the coplanar capacitances of resonator and qubit. The pads geometry and dimensions define the coupling of the resonator and qubit modes to the electromagnetic field inside the waveguide. The pads are labeled according to the nodes in the circuit schematics (Fig. 40 a). We make the resonator inductances L and L_a out of grAl stripes. Using grAl with high kinetic inductance per square $L_{kin} = 0.17\,\mathrm{nH}/\square$ allows to build compact loops for magnetic flux bias with ratio $\Phi_{xb}/\Phi_x \approx 50$. The array Josephson junctions should have large area to prevent phase slips. For $E_j/E_c = 150$ the charging energy $E_c = 0.48\,\mathrm{GHz}$ corresponds to a parallel plate capacitance of $\approx 40\,\mathrm{fF}$. The required junction area $0.2\times4\,\mu\mathrm{m}^2$ can be achieved with overlap geometry (Fig. 44 d).

We find the optimal circuit geometry for our target circuit parameters and coupling rates of the resonator and qubit modes by finite element simulation of the electromagnetic field inside the waveguide (see sections 5.2 and 5.3 for details). Superconducting aluminum films are modeled as perfect conductors, while Josephson junctions and grAl are modeled as lumped elements with fixed linear inductance. Fig. 45 shows the calculated distribution of the electric field magnitude $|\vec{E}|$ at the surface of the sapphire chip for the resonator and qubit eigenmodes (panel a and b, respectively). Labels indicate charge polarity. Notice that the charge distribution for the resonator mode is symmetrical about the central axis. The simulated resonator and qubit coupling quality factors are 8.7×10^3 and 7.3×10^8, respectively.

The circuit is fabricated in three lithography steps. First, we make aluminum capacitance pads, the qubit junction, and the first electrodes of array junctions with e-beam lithography (green layer in Fig. 44). In this way the sapphire surface under large elements and junctions is contaminated least of all. Prior to aluminum deposition the surface is cleaned with oxygen plasma to remove resist residues and organic contamination. The qubit junction with area $0.2\times0.2\,\mu\mathrm{m}^2$ is fabricated using shadow evaporation technique with first and second electrodes evaporated at the angle of $\pm30°$ from the plane's normal. Shadow evaporation in areas of

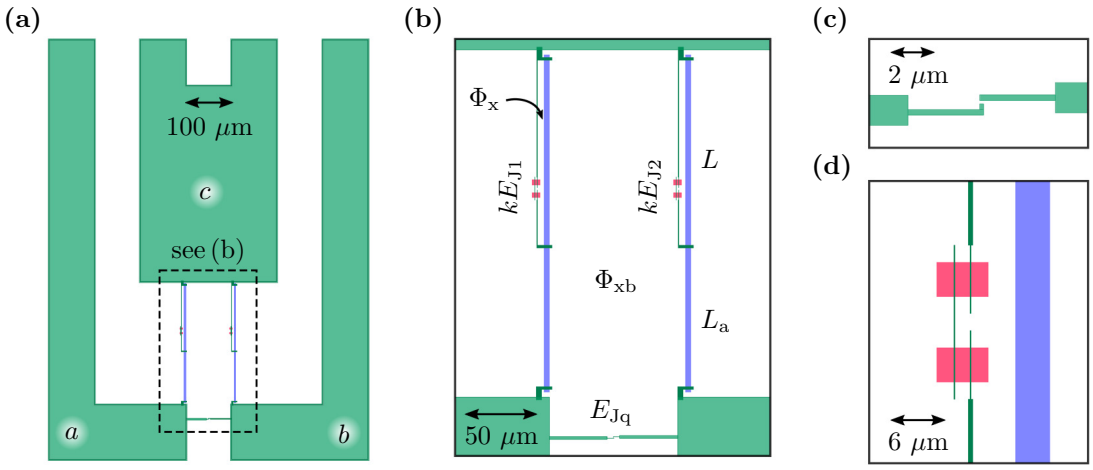

Figure 44: **Tunable transmon circuit implementation.** **(a)** Fabrication mask for the circuit. Green color corresponds to the e-beam lithography layer. The three large pads play role of resonator and qubit capacitances, the corresponding nodes (a, b, c) are labeled according to the circuit schematics (see Fig. 40 a). Blue and pink structures are made with optical lithography in separate vacuum cycles. **(b)** Zoom into central part showing large loop biased by Φ_{xb}. The loop area is $100\times300\,\mu\mathrm{m}^2$. Inductances L and L_{a} shown in blue are made out of grAl. Pink rectangles correspond to the top electrodes of the array Josephson junctions (overlap junction design). The qubit junction is made with shadow evaporation technique [Nie+74]. Capacitor pads and qubit junction are evaporated in the same vacuum cycle. **(c, d)** Zoom into qubit junction (with area of $0.2\times0.2\,\mu\mathrm{m}^2$) and coupling junctions (with area of $0.2\times4\,\mu\mathrm{m}^2$), respectively. The array junctions in the left branch have slightly smaller area to introduce asymmetry $E_{J2} = 0.95\,E_{J1}$.

large pads results in stray Josephson junctions, which internal dynamics can be neglected due to high self-resonance frequency. In a second and third steps we deposit grAl stripes (blue layer in Fig. 44) and top electrodes of the array junctions (pink layer in Fig. 44) using optical lithography. In-between the separate vacuum cycles of the deposition, the metal surface builds an insulating native oxide which has to be removed to ensure coherent galvanic contact between the metal layers. We remove oxide in areas of contact by argon ion milling [Grü+17]. After

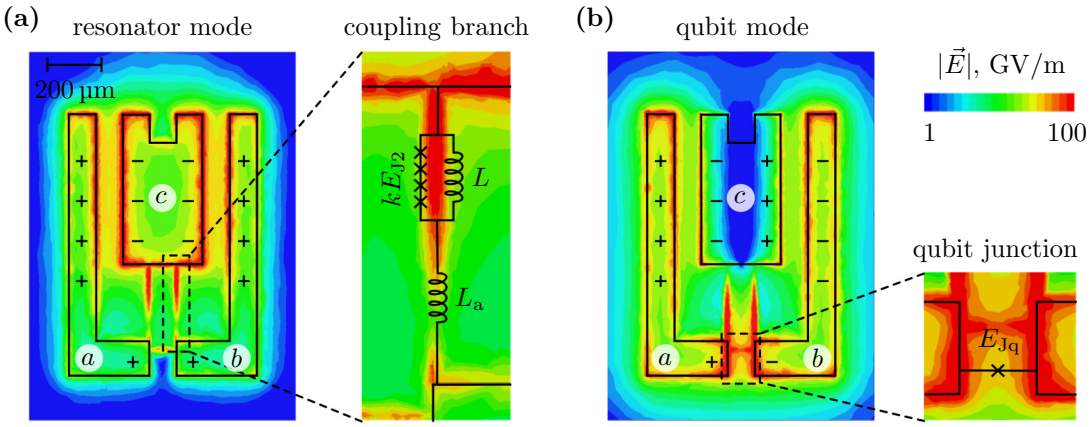

Figure 45: **Finite element simulation of resonator and qubit modes**. The circuit is placed inside a 3D copper waveguide (see sections 5.2), thereby coupling to the electromagnetic field excited in the waveguide via the dipole moment of the capacitor pads. **(a)** Resonator mode. Color code corresponds to the magnitude of the calculated electric field. Labels indicate charge polarity of the capacitor pads. **(b)** Qubit mode. For resonator and qubit modes at frequencies of 8.0 GHz and 6.3 GHz we extract the coupling quality factors of 8.7×10^3 and 7.3×10^8, respectively.

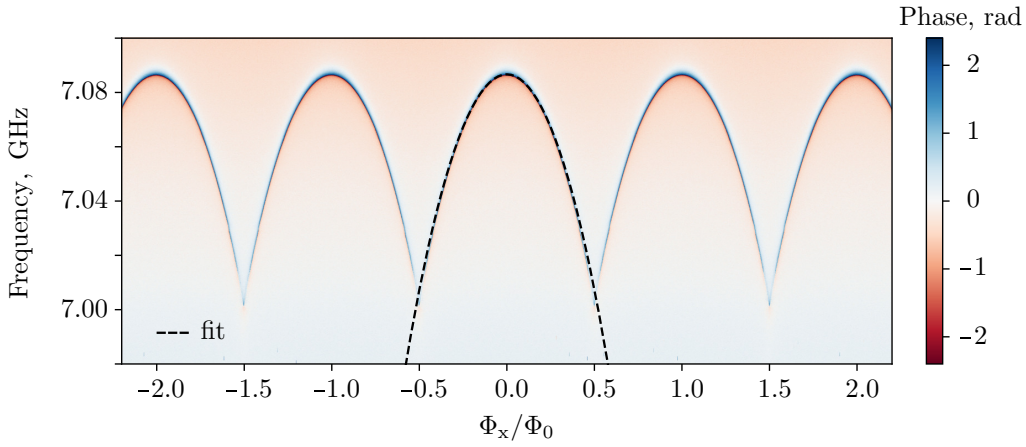

Figure 46: **Resonator spectroscopy** The color plot demonstrates measured resonator response as a function of external magnetic field Φ_x and probe frequency. Color indicates phase of the output signal. Black dashed line corresponds to a fit of the data. From the fit we extract the circuit parameters $L = 4.9\,\text{nH}$, $L_a = 3.7\,\text{nH}$, $E_{J1} = 46\,\text{GHz}$, $C = 68.7\,\text{fF}$, $C_q = 50\,\text{fF}$. The resonator frequency shows a periodicity with one flux quantum in the coupling loop.

milling, the contact surface is oxidized with controlled oxygen partial pressure to achieve the desired Josephson energy. Details of the fabrication process can be found in section 5.1.

3.3 Resonator spectroscopy

For several fabricated resonators we measure the resonance frequency as a function of the external magnetic field through the small loops. An example of a resonator spectroscopy is shown in Fig. 46. Unfortunately, the phase slip rate for all the measured resonators is higher than expected and resonators show a single flux quantum periodicity in Φ_x. However, to achieve pure longitudinal coupling we have to bias small loops with $\Phi_x \approx 1.5\,\Phi_0$, which corresponds to a metastable state of the junction array. One way to suppress phase slips is to increase the junction area, but it was not possible in the current geometry due to fabrication constraints. As an alternative solution, we propose to enclose the junction arrays by grAl loops, similar to the gradiometric fluxonium design. We still need flux sensitivity for the tunable transmon, therefore loops can be made asymmetric to create a field gradient.

In theory, the phase slip rate in a grAl loop is expected to be orders of magnitude smaller than in a junction array. However, this solution brings back the problem of flux escape observed in the gradiometric fluxonium (see section 2.6.2). Future investigation of phase slips in grAl loops or even a completely different choice of high kinetic inductance material is required to accomplish the proposed longitudinal coupling scheme.

4 Conclusions and outlook

This thesis is dedicated to quantum non demolition (QND) readout of superconducting artificial atoms and their coupling to the environmental electromagnetic fields. In the first chapter we introduce the concept of QND readout and discuss the role of interactions between quantum system and measurement apparatus and the environment. We consider QND interaction schemes of artificial atoms and readout resonators proposed in the framework of circuit quantum electrodynamics theory (cQED). We show how to construct the main building blocks used in cQED, namely quantum oscillators and artificial atoms. We use the example of two state-of-the-art superconducting artificial atoms, transmon and fluxonium, to demonstrate how circuits can be protected from decoherence caused by charge noise. We show the atoms spectrum and discuss their physical implementation.

We use granular aluminum (grAl), a material with high kinetic inductance to construct circuits presented in this thesis. We briefly outline the material properties associated with its internal structure: dependence of the superconducting gap on the room temperature resistivity, its kinetic inductance, nonlinearity, and main sources of decoherence. We show that granular aluminum can be used as high impedance environment for superconducting circuits, which suppresses charge fluctuations and shunts charge offsets. We provide the linearized model of grAl inductors based on their equivalent representation as a chain of Josephson junctions and compare superinductances made out of grAl and Josephson junction chains. The key difference between the two superinductors implementations are the nonlinearity and plasma frequency. We show that depending on the circuit geometry grAl can be designed with orders of magnitude smaller nonlinearity, and its plasma frequency is few times larger than that of Josephson junction chain with same linear inductance.

In the second chapter we address the dispersive interaction, which is the most commonly used scheme for QND readout of superconducting qubits. We show the theoretical model for the readout signal to noise ratio, and the way to increase measurement QNDness by using high power readout. However, typically, increasing readout power leads to measurement induced transitions between levels of superconducting atoms, and high power readout loses its advantage. In contrast to many superconducting atoms, our fluxonium with tunable spectrum built with granular aluminum superinductance has remarkable resilience of transition rates to number of photons in the readout resonator $\bar{n}$. We demonstrate high fidelity atom readout and state preparation without parametric amplifier at power corresponding to hundreds of circulating photons. We quantify the QNDness of the high power dispersive readout by measuring atom transition rates as function of $\bar{n}$, and by fidelity of the atom active state preparation. We perform numerical simulations of the coupled atom-resonator state evolution during the measurement to find the source of residual non-QNDness. The simulations reveal that atom local decay acting on the hybridized atom-resonator levels results in atom transitions to the second excited level. Our measurements suggest that suppressed nonlinearity of the resonator and atom inductances and coupling inductance plays an important role in achieving QND high power readout. Our results imply that future efforts should be focused on further improvement of qubits lifetime and suppression of nonlinearity-induced multimode mixing in the atom-resonator Hamiltonian.

We demonstrate the ability to design interaction of the artificial atoms with the external electromagnetic field by building gradiometric fluxonium atom. The gradiometric atoms made with grAl superinductances show suppression of sensitivity to applied magnetic field up to 180 times, as was predicted by theoretical calculations. The atoms can be biased at the degeneracy point by cooling down in the external magnetic field, which might be used for fluxon-based simulations and storage of quantum information. We find that coherence of grAl fluxoniums with two loops is most probably limited by local flux noise. Contrary to our expectations, we observe trapped flux escape out of the superconducting rings every hour or so, exceeding the expected escape probability by several orders of magnitude. The stability of circulating currents in superconducting rings is a fundamental issue and might be related to the internal structure of grAl. The next steps would be to measure correlations between flux escapes for several atoms on the same chip to exclude environmental sources of phase slips. Last but not least, replacing pure aluminum by grAl should make gradiometric fluxonium compatible with hybrid circuits and extend their range of applications.

Finally, in the third chapter we turn to implementation of purely QND readout scheme based on longitudinal interaction of the transmon artificial atom and the readout resonator. The circuit design was proposed in Ref. [**Richer2016longitudinal**], and it offers tunability between pure longitudinal and pure transverse coupling with the applied magnetic field. We design and build the proof of principle device, which also turned out to suffer from phase slips in the coupling Josephson junction arrays. Biasing coupling arrays at points of pure longitudinal coupling was therefore impossible without further suppression of phase slips. Since we successfully demonstrated the ability to tune the gradiometric fluxonium atom to highly metastable state, we propose a similar design to protect the coupling junction arrays by enclosing them in grAl loop. However, prior to building the next generation of devices, the problem of flux escapes in grAl superconducting loops has to be solved.

In conclusion, our work sheds new light on the problem of QND readout of superconducting atoms. We demonstrate that high power dispersive QND readout is possible, and make a hypothesis explaining the observed grAl fluxonium resilience to readout power by suppressed nonlinearity of the interaction term in comparison to other fluxonium implementations. Our experience shows that building longitudinal coupling schemes which require nonlinear coupling regime is a sophisticated problem. It remains practically unfeasible with current fabrication technologies due to unexpected phase slips in grAl superconducting rings. Phase slips are a roadblock on the way to implementation of stable fluxon-based superconducting circuits, and we need comprehensive study of material properties and environmental effects to mitigate them.

5 Methods

5.1 Fabrication

Here I present the main fabrication techniques used to produce our samples. The following section outlines the fabrication process, including preparation of wafers, resist coating, lithography, plasma cleaning, metal deposition, and resist lift-off. In section 5.1.4 I present details of Josephson junction fabrication, and section 5.1.4 is devoted to fabrication of granular Aluminum films. Fabrication was done in Nanostructure Service Laboratory (NSL) of the Karlsruhe Institute of Technology.

5.1.1 Substrates preparation

All the samples presented in this thesis were made on double-side polished 330 µm thick C-plane sapphire wafers. Fabrication process starts with cleaning wafers in Piranha solution (3 parts of 96% H_2SO_4 to 1 part of 35% H_2O_2) for 10 minutes. Piranha is an aggressive oxidizer and removes organic residues, metallic and carbon contaminants.

5.1.2 Lithography

We cover wafers with optical or electron-sensitive resist films in order to pattern masks for metal deposition. We use electron beam lithography for high resolution structures with dimensions $\geq 200\,\text{nm}$, and optical lithography for structures with dimensions $\geq 4\,\mu\text{m}$. Resist films are deposited in spincoater and baked on the hot plate to solidify the film. The film thickness depends on the resist viscosity, spin speed, and acceleration during speed ramp up.

Electron beam lithography

We use electron beam lithography to pattern evaporation masks for tunnel Josephson junctions and other structures, which can be deposited in the same vacuum cycle of a shadow evaporator. We cover sapphire wafers with copolymer EL-13/PMMA A4 resist bilayer, spinning and baking

Resist spincoating (bottom layer copolymer EL-13, top layer PMMA A4)

spin acceleration	1000 rpm/s
spin speed (rpm)	2000 rpm
spin time	100 seconds

Hot plate baking

hot plate temperature	200°C
baking time	5 minutes

E-beam exposure

accelerating voltage and base dose	50 kV, 500 µC/cm^2
e-beam current	10 nA (low resolution) and 2 nA (high resolution)

Resist development

developer	IPA/H_2O (3/1) at 6°C
development time	1.5 minutes
stopbath	ddH_2O

Table 4: **Fabrication process with electron beam resist.** E-beam exposure doses were varied depending on the pattern geometry, correction factors are listed in the main text.

parameters are the same for both resists (see Table 4). The resulting resist thickness is 700−750 nm for copolymer EL-13, and 300−350 nm for PMMA A4. Sapphire is dielectric material and it can accumulate charge during electron beam exposure. Charges at the surface of the wafer deflect back-scattered and secondary electrons, which leads to pattern distortion and degrades lithography resolution. Therefore, we sputter a $\sim 10\,\mathrm{nm}$ layer of gold on top of PMMA A4 resist to avoid charging effects.

Patterns were exposed using vector JEOL JBX-5500 writer with 50 kV accelerating voltage. Structures with size $\geq 2\,\mu\mathrm{m}$ were exposed at beam current of 10 nA, while smaller structures were exposed at 2 nA. The base dose is $500\,\mu\mathrm{C/cm^2}$. We use built-in proximity correction algorithms for large structures with size $\geq 2\,\mu\mathrm{m}$, and manual dose correction factors for grAl wires and Josephson junction electrodes ($2.6\times500\,\mu\mathrm{C/cm^2}$ and $3.3\times500\,\mu\mathrm{C/cm^2}$, respectively). Junction undercuts were written with 0.35−0.67 dose correction factors.

Before resist development we remove gold layer by immersing wafers in 15% Lugol solution for 5 seconds and rinse wafers by double distilled water (ddH_2O). Patterns are developed in IPA/H_2O (3/1) solution which dissolves exposed resist. Dissolution rate is higher for copolymer EL-13 compared to PMMA A4. Therefore, top resist layer typically forms high resolution mask, and bottom layer serves for undercut (see Fig. 48). Development is stopped in ddH_2O.

Optical lithography

Optical lithography was done using SUSS MA6 mask aligner with XeHg 500 W lamp which has wavelength of 365 nm. Usually positive photoresists (exposed areas are dissolved by the developer) form overcut sidewall profile, as shown Fig. 47. This is due to attenuation of light during propagation in the resist. Top and bottom resist layers see different exposure doses, and bottom layers have smaller dissolution rate. Metal evaporated on the top of the resist mask

AZ 5214E resist spincoating

spin acceleration	7500 rpm/s
spin speed (rpm)	6000 rpm
spin time	60 seconds
reflow	30 seconds

Hot plate baking

hot plate temperature	110°C
baking time	50 seconds

UV hard contact exposure

dose	$13\,\mathrm{mW/cm^2}$
exposure time	2 seconds

Reversal baking

hot plate temperature	120°C
baking time	90 seconds

Flood exposure

dose	$13\,\mathrm{mW/cm^2}$
exposure time	30 seconds

Resist development

developer	AZ developer/H_2O (1/1)
development time	30 seconds
stopbath	ddH_2O

Table 5: **Fabrication process with photoresist.**

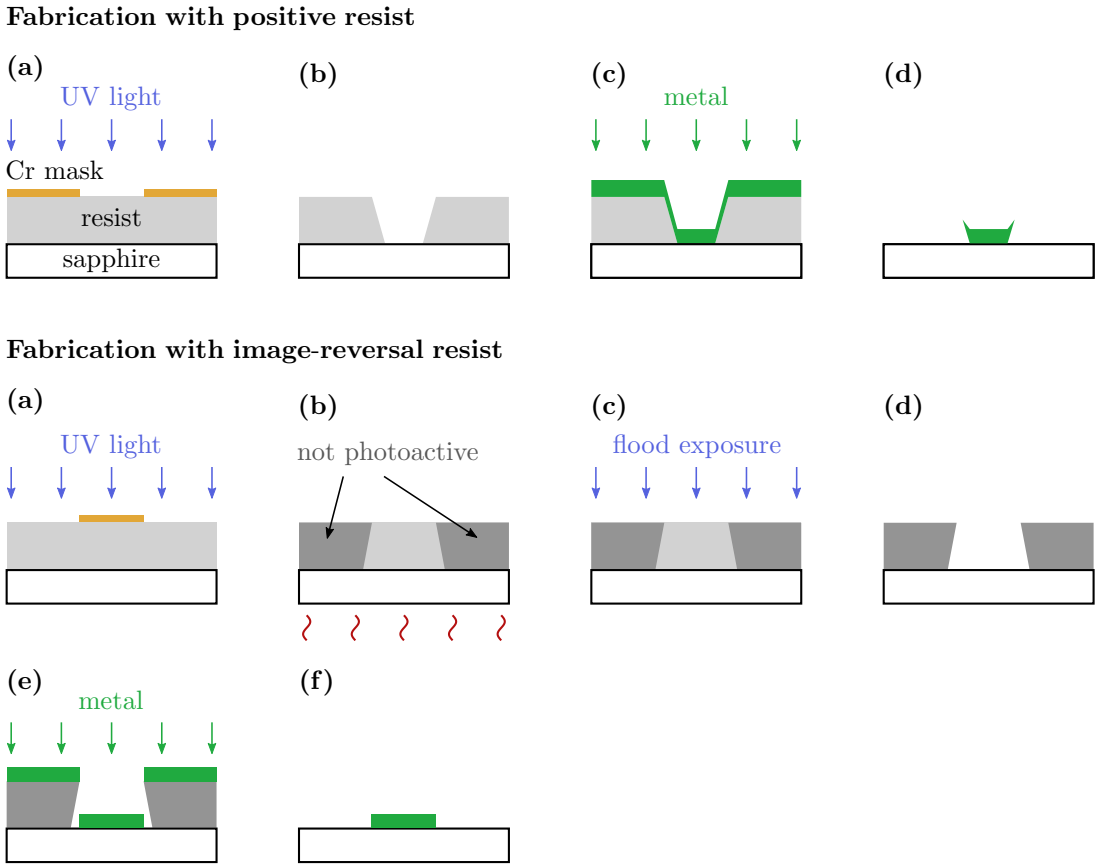

Figure 47: **Fabrication with photoresist.** Fabrication with positive resist results in overcut sidewall profile. **(a)** Exposure of positive photoresist. Chromium mask is shown in yellow. **(b)** Resist wall profile after development. **(c)** Metal evaporation (green). **(d)** After liftoff metal film has fences along the edges. Fabrication with image-reversal resist yields undercut sidewall profile. **(a)** Exposure with inverted mask. **(b)** Reversal baking. **(c)** Flood exposure. **(d)** Resist wall profile after development. **(e)** Metal evaporation (green). **(f)** Metal film after liftoff.

with overcut sidewalls is forms continuous film. During liftoff process resist is dissolved. Metal film is torn apart, parts deposited onto the resist surface are removed, but liftoff leaves residual fences along the edges of the film deposited onto the wafer. Since electric field is strongest near sharp edges due to concentration of charges, defects located in the fences might be a source of additional dissipation in superconducting circuits.

To cut down the fences we seek negative resist wall profile (undercut). We use AZ 5214E photoresist suitable for image reversal process (see Fig. 47). Image reversal makes exposed areas insoluble in developer. First, resist is exposed through the mask using hard contact photolithography. We use inverted chromium mask on soda substrate. Areas covered with chromium correspond to the metal structures which should be patterned on the wafer. The reversal baking renders exposed areas not photoactive. The following flood exposure (without a mask) makes all other areas soluble in the developer. As a result, resist mask for evaporation has undercut wall profile. Evaporated metal film has discontinuity at the edges of the resist, which results in smooth edges of the metal film after liftoff. Fabrication parameters for image reversal process are listed in Table 5.

5.1.3 Plasma cleaning

We perform a plasma cleaning step prior to metal deposition in order to remove residues left after the resist development. Plasma cleaning is made in the load lock chamber of a Plassys MEB 550S shadow evaporator using built-in Kaufman ion source. We use descum process if metal is evaporated onto bare surface of wafers (without any metal layers deposited before).

Descum cleaning

gas flow	Ar (5 sccm), O_2 (10 sccm)
discharge voltage	40 V
ion gun beam voltage	200 V
ion beam current	10 mA
accelerating voltage	120 V
etching time	2 minutes

Argon ion beam milling

gas flow	Ar (4 sccm), O_2 (0 sccm)
discharge voltage	40 V
ion gun beam voltage	400 V
ion beam current	15 mA
accelerating voltage	90 V
etching time	2 minutes

Table 6: **Plasma cleaning.**

Plasma in the descum process has high oxygen content and removes resist residues without substantial damage of the wafer surface. A different process is required if metal is evaporated on top of another metallic layer covered with oxide. We remove oxide with Argon ion beam milling process developed for coherent galvanic contacts between aluminum layers [Grü+17]. The plasma cleaning parameters are listed in Table 6.

5.1.4 Metal deposition

We use Plassys MEB 550S electron beam shadow evaporator for deposition of aluminum and granular aluminum films. After plasma cleaning, we pump the load lock chamber until pressure of $\lesssim 5{\times}10^{-5}$ mbar with built-in turbo pump. Residual gases are absorbed during Titanium evaporation, and load lock pressure drops to $\approx 1{\times}10^{-5}$ mbar. Aluminum is evaporated at the rate of 1 nm/s onto sapphire wafers kept at the room temperature.

Josephson junctions

Josephson junctions are typically made out of two overlapping aluminum electrodes. An insulating barrier between them is formed by oxidizing surface of the first electrode. The junction normal state resistance depends on the oxygen partial pressure and oxidation time. Ambegaokar-Baratoff relation shows that the junction critical current at zero temperature is related to the superconducting energy gap Δ, and the normal-state junction resistance [AB63]:

$$I_c = \pi\Delta/(2eR_n). \tag{100}$$

$Al/AlO_x/Al$ junctions have barrier approximately 1 nm thick, and the geometric parallel plate shunting capacitance of $\sim 50{-}200\,\mathrm{fF}/\mu\mathrm{m}^2$ [FD87; Gee+89; KH91].

We use Niemeyer-Dolan double angle evaporation technique [Nie+74] to pattern tunnel junctions with dimensions $\lesssim 250{\times}250\,\mathrm{nm}^2$. Fig. 48 a shows an e-beam lithography design of the junction. Corresponding bilayer resist mask after development and metal deposition is shown in Fig. 48 b. We evaporate first and second junction electrodes at the angle of $\pm 30°$, respectively. For the sample with gradiometric fluxonium (see section 2.6) we oxidize the first electrode in the static regime at fixed pressure of 30 mbar for 340 seconds. Thickness of the first and second aluminum electrodes is 20 nm and 30 nm, respectively. We make the second electrode thicker to avoid film interruptions at the edges of the contact.

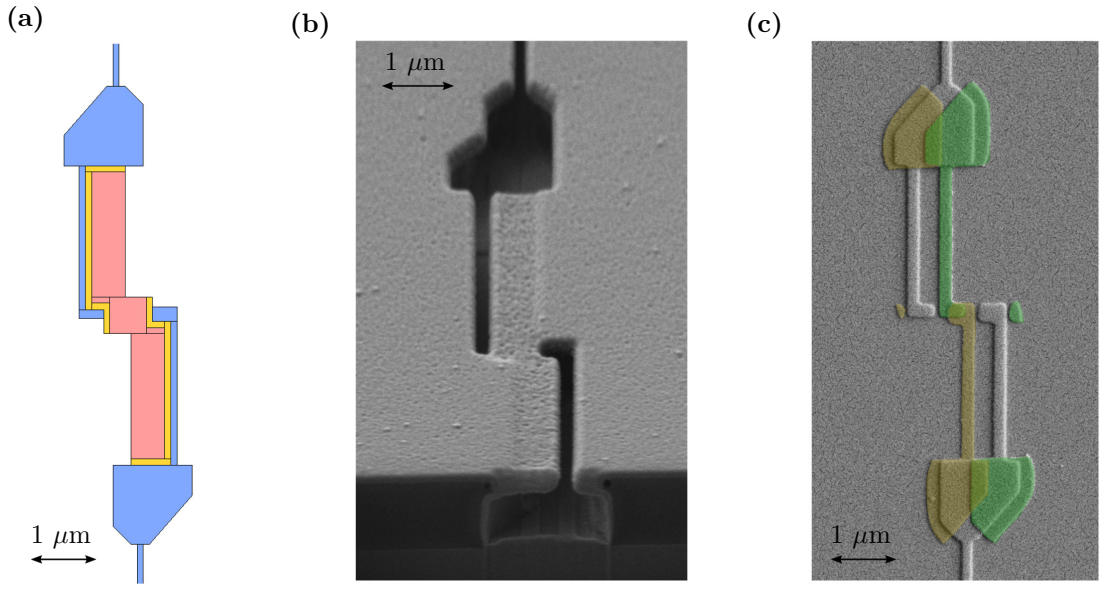

Figure 48: **Niemeyer-Dolan evaporation of the Josephson junctions.** **(a)** E-beam lithography design of the Josephson junction used for the gradiometric fluxonium atom (see section 2.6). Blue patterns correspond to openings in the top resist layer, while orange (fringe) and pink (undercut) patterns indicate areas where the bottom resist layer is additionally removed. **(b)** Focused ion beam image of the junction area after resist development and metal deposition. Resist is cut perpendicular to the second electrode, and undercut in the bottom resist is visible. **(c)** Scanning electron microscope image of the junction. First and second electrodes evaporated at ±30° are shown in yellow and green, respectively. Josephson junction has area of 207×227 nm^2. Uncolored patterns correspond to grAl film deposited at zero angle.

Josephson junctions with larger dimensions were made using overlap design. We evaporate first electrodes using electron beam lithography. After resist lift off, me make optical lithography to pattern the second electrode. Lithography mask for the Josephson junctions used in the longitudinally coupled transmon circuit (see section 3.2) is shown in Fig. 49 a. We have to evaporate the two electrodes in separate vacuum cycles. The first electrode is exposed to atmosphere, and its surface is covered with native oxide layer with uncontrollable parameters. Prior to the second electrode evaporation, we remove native oxide with Argon milling, and

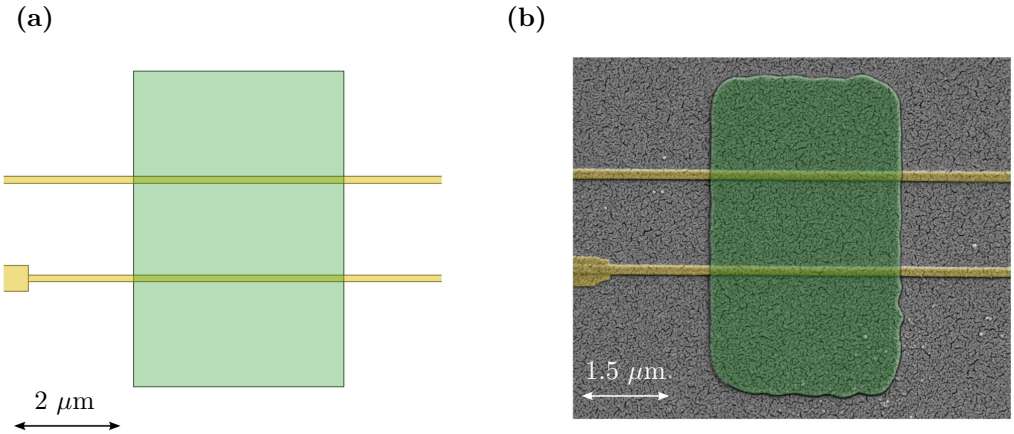

Figure 49: **Overlap Josephson junctions.** **(a)** Lithography mask for the Josephson junctions in the junction arrays of the longitudinally coupled transmon circuit (see section 3.2). Yellow and green color indicate first (e-beam lithography) and second (optical lithography) electrodes. **(b)** The scanning electron microscope image of the junction. The junction has area of 0.17× 3.67 μm^2.

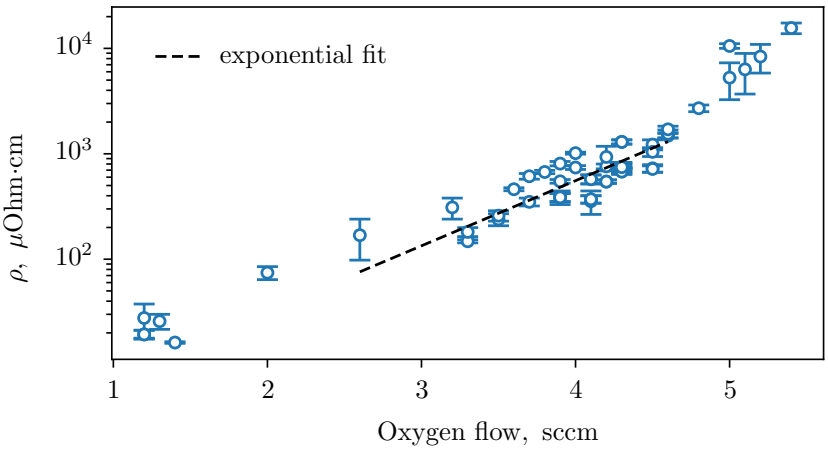

Figure 50: **Granular aluminum resistivity as function of oxygen flow.** Aluminum is evaporated at the rate of 1 nm/s in oxygen atmosphere. Markers show measured average resistivity for each wafer, while error bars indicate spread of resistivity due to observed gradient. Dashed line is an exponential fit.

oxidize the contact area of the first electrode at pressure of 10 mbar for 250 seconds.

Granular aluminum deposition

Typically, we deposit granular aluminum in the last step of fabrication. Areas of contact with previously evaporated aluminum are cleaned with Argon ion milling. Granular aluminum is obtained by evaporating aluminum in oxygen atmosphere. GrAl kinetic inductance depends on the normal state resistance of the films (see eq. 16). We control grAl resistance by oxygen flow rate during evaporation in dynamic oxidation regime. In this regime gas is continuously injected and pumped out of the load lock chamber, ratio between gas flow and pumping rates defines its partial pressure. Oxygen flow rate of 4−5 sccm corresponds to partial pressure of $5{-}7{\times}10^{-5}$ mbar. Due to positions of the gas valve and the pump in the chamber oxygen is not distributed uniformly, and we observe gradient of grAl resistivity across the sapphire wafer. Fig. 50 demonstrates a calibration curve for grAl resistivity depending on the oxygen flow rate for aluminum evaporated at the rate of 1 nm/s. Dashed line is an exponential fit. Notice, that we can not fit all the data with single exponential.

5.1.5 Resist lift-off

After metal evaporation we remove the resist and metal deposited onto its surface in lift-off process. We immerse wafers into N-Ethyl-2-pyrrolidone (NEP) kept at 90°C for one hour. Resist residues are then removed in the ultrasonic bath. NEP is rinsed by acetone, isopropanol, and double distilled water.

5.2 Waveguide sample holder

We use 3D copper waveguides as a controlled microwave environment for our superconducting circuits [Zoe+17; Kou+18a]. Waveguide is equipped with a rectangular superconducting coil used to bias circuits with magnetic field. Fig. 51 shows rectangular waveguide attached to the copper post, the superconducting coil, and the magnetic shield. The waveguide inner volume dimensions 42.7×25.8×12.9 mm define a TE_{10} mode passband from 6.4 GHz to 8.1 GHz. A sapphire chip is fixed inside the waveguide at a quarter wavelength distance from the waveguide lid, at the antinode of the electric field. We operate fluxonium atoms at frequencies below the waveguide cutoff, which helps to mitigate the atom radiative losses due to reduced density of environmental modes. Readout resonators typically have frequencies within the waveguide passband.

Waveguide has two microwave ports connected to coaxial 50 Ω cables. The first port at the back of the waveguide has impedance matching cylinder, and is used to drive readout resonators. Two screws inserted in the bottom of the waveguide provide fine tuning of impedance matching and the waveguide bandwidth. We can not drive fluxonium atoms via the same port, because electromagnetic field is strongly attenuated at frequencies below waveguide cutoff. Therefore, we use the second microwave port located close to the chip. This port consists of a central pin of the coaxial line with removed isolation, and is not impedance matched.

We use cryogenic vacuum grease to fix sapphire chip inside the waveguide. The grease solidifies at cryogenic temperatures, and provides thermalization of the chip. The waveguide lid is closed tightly with four brass screws. We lay thin indium seal between waveguide and the lid to ensure galvanic contact between them. Copper is not a superconducting material, therefore it does not shield circuits from environmental electromagnetic fields. Therefore we place the waveguide inside copper-aluminum shield, also thermalized to a mixing chamber plate of the cryogenic refrigerator.

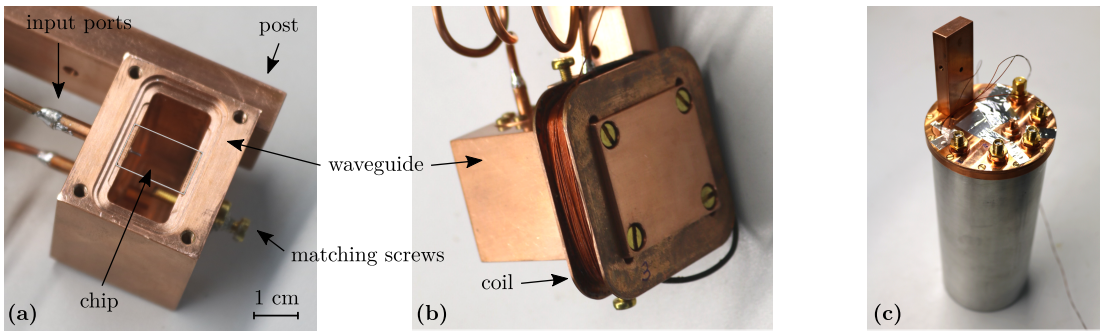

Figure 51: **3D waveguide sample holder and the magnetic shield. (a)** Copper waveguide without lid. A 10×15 mm^2 sapphire chip with superconducting circuits is fixed at the location of maximal electric field $|\vec{E}|$ of the propagating TE_{10} mode at frequency of 7 GHz. The waveguide has two microwave input ports. The first port located further from the chip is impedance matched with 50 Ω coaxial line, and is used to drive readout resonators and measure their response in reflection. The impedance matching can be tuned with two brass screws inserted into the waveguide [Poz11]. The second input port located close to the chip is not impedance matched. It is used to drive fluxonium atoms at frequencies below waveguide cutoff. The waveguide is attached to a copper rod which thermalizes the circuits to a mixing chamber plate of the cryogenic refrigerator. **(b)** Waveguide with closed lid and a superconducting coil, which generates magnetic field perpendicular to the plane of sapphire chip. **(c)** The waveguide is placed inside cylindrical shield made of two layers: copper (inner) and aluminum (outer). The copper is used for thermalization, while superconducting aluminum damps the environmental magnetic fields. The shield is closed with a copper cap equipped with SMA coaxial feedthroughs.

5.3 HFSS finite element simulations

We perform finite element simulations of the superconducting circuits to optimize their geometry and find their coupling to electromagnetic field inside the waveguide. We use Ansys HFSS solver with eigenmode analysis to find resonance frequencies and coupling quality factors based on the geometry, materials, and boundaries defined for the model. Fig. 52 a shows the HFSS waveguide model. The waveguide, impedance matched microwave port, tuning screws, and the sapphire chip are modelled as 3D objects. The sapphire chip has relative permittivity $\epsilon_r = 10$, and relative permeability $\mu_r = 1$. The superconducting circuit is represented by a 2D sheet on the surface of the chip. This approach is valid since thickness of the superconducting film (20−100 nm) is much smaller than other dimensions in the model.

We assign a 50 Ω impedance boundary to the plane of the input port, and perfect conducting boundary to waveguide copper body and parts of the superconducting circuit made out of aluminum. Granular aluminum wires are modelled as lumped RLC elements with inductance equal to the target kinetic inductance, and zero resistance and capacitance.

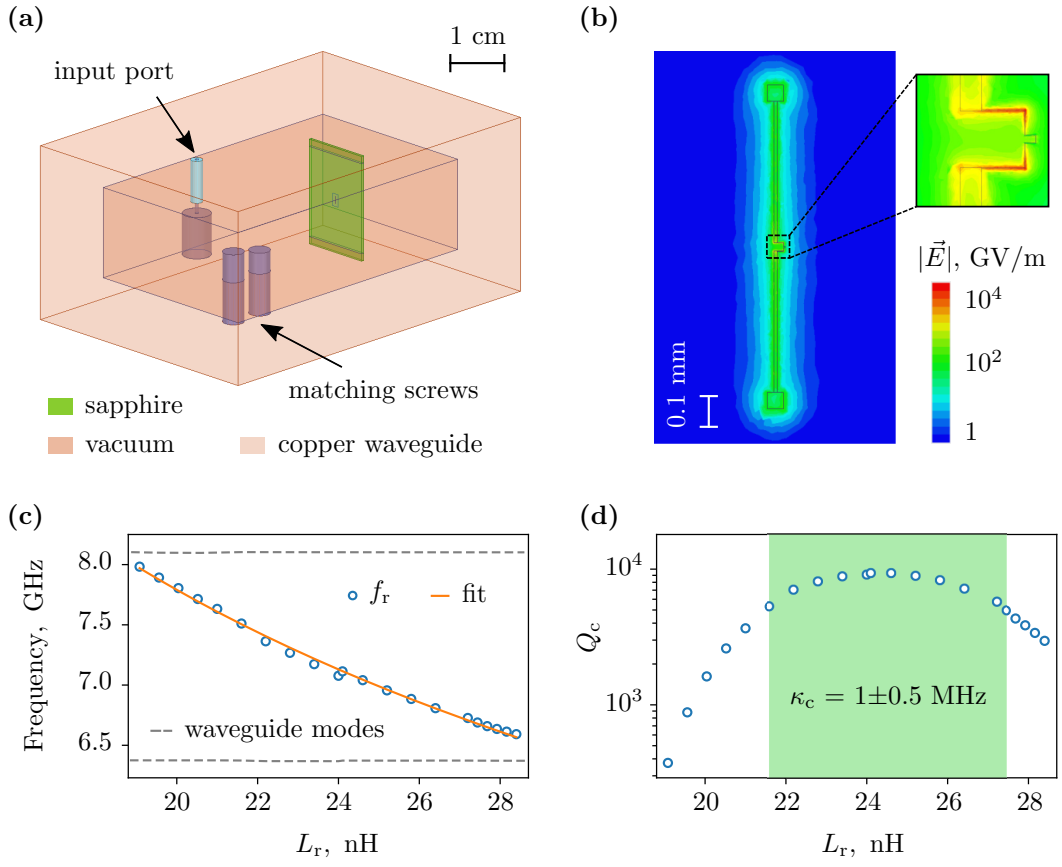

Figure 52: **HFSS finite element simulation of the electromagnetic fields in the waveguide sample holder. (a)** Waveguide model. Green color indicates sapphire chip. A superconducting dipole antenna resonator is located in the middle of the chip at the antinode of the electric field. **(b)** Simulated distribution of the electric field at the plane of the antenna resonator. **(c, d)** Simulated resonator frequency (left panel) and the coupling quality factor (right panel) as functions of the resonator inductance L_r. Blue markers show the calculated values. We fit the resonance frequency with $f_r = (2\pi\sqrt{(L_{kin}+L_g)C_r})^{-1}$ to extract the resonator capacitance $C_r = 20.2$ fF and the geometric inductance $L_g = 0.6$ nH. The grey dashed lines show the waveguide eigenmodes at 6.4 GHz and 8.1 GHz. Hybridization of resonator with waveguide modes increases its coupling rate. The green shaded interval in panel d indicates region where the coupling rate $\kappa_c/2\pi = f_r/Q_c = 1\pm0.5$ MHz.

Fig. 52 b shows the distribution of the electric field on the surface of the sapphire chip around the dipole antenna resonator. The field is calculated at the resonator frequency for the total stored energy of 1 J. Resonator dipole moment is aligned with electric field of propagating waveguide TE_{10} mode. We aim at the resonator frequency within the waveguide passband and its coupling rate $\kappa_c/2\pi = 1\,\mathrm{MHz}$. We sweep the kinetic inductance of grAl wires to extract the capacitance and geometric inductance of the resonator (see Fig. 52 c). Resonator coupling strength depends on the dipole length, position of the resonator on the chip, and its hybridization with waveguide modes. Calculated coupling quality factors for fixed dipole length of 1 mm and central position of the resonator are shown in Fig. 52 d.

5.4 Measurements

We use interferometric time domain measurement setup with custom designed FPGA-based platform [Geb+20] for readout and control of superconducting qubits. The setup schematic is shown in Fig. 53. The platform has sampling rate of 500 MSPS, and it generates waveforms modulated at frequency of $f_{IF} = 62.5\,\mathrm{MHz}$ for readout, and $f_{IF} = 80\,\mathrm{MHz}$ for qubit manipulation. The manipulation IF tone is mixed with a continuous wave carrier signal using the internal I/Q modulator of the signal generator. The sideband products suppression measured at the input of the cryostat is at least 19 dB. The resulting pulse at the qubit first transition frequency f_{ge} is attenuated by 60 dB inside the cryostat and fed into the qubit manipulation port of the sample waveguide.

We use single a sideband mixer to upconvert the readout IF tone to the resonator frequency f_r. The readout tone is split in two parts after the mixer. The first part, called *reference* is

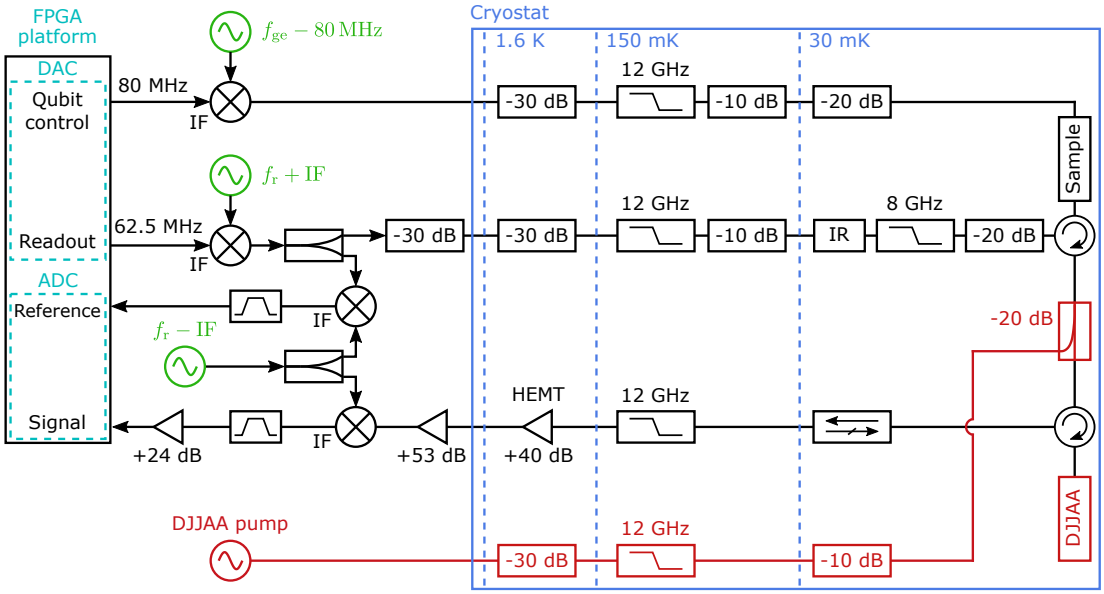

Figure 53: **Interferometric time-domain measurement setup**. The custom designed FPGA-based platform [Geb+20] is used to generate waveforms for the readout and fluxonium control pulses, with IF frequencies of 62.5 MHz and 80 MHz, respectively. The IF waveforms modulate the carrier signals from microwave generators (shown in green). The readout line is divided in two parts. The first part of the readout tone is directly downconverted and digitized, and is used as reference at the analog-to-digital converter (ADC) input of the FPGA. The second part of the readout tone is sent through the cryostat, where the signal interacts with the sample. The reflected signal is amplified by a cascade of cryogenic and room temperature amplifiers, downconverted, and digitized at the second port of the ADC. The digitized *signal* and *reference* waveforms are interfered on board, and I and Q components of the readout signal can be calculated in real time. The parametric amplifier (DJJAA) [Win+20a] was used only at low readout power.

downconverted and fed into analog-to-digital converter (ADC) of the FPGA platform. The second part is sent into cryostat, where it is attenuated by total amount of 90 dB and filtered by commercial low-pass and home made infrared filters in order to reduce thermal noise. Signal reflected from the sample is directed by circulator to the output line. The output line is equipped with the DJJAA [Win+20a] parametric amplifier connected to the signal line via a commercial directional coupler. The coupler also provides 20 dB attenuation for noise emitted back from the HEMT amplifier. The DJJAA is activated by pump tone, and acts as a perfect reflector if not pumped. The signal is further amplified by a commercial HEMT amplifier and downconverted to IF frequency. Both signal and reference are filtered with commercial band pass (55−67 MHz) filters before input of the FPGA ADC.

The signal and reference are interfered on board to extract the quadratures of the readout signal. Signal traveling through the cryostat acquires delay of ≈ 80 ns. The leading edges of the signal and reference pulses are first aligned using calibrated delay of the reference. The I component is obtained by sample-wise multiplication of signal and reference, while Q component is obtained by multiplication of signal and quarter-period shifted reference. The measurement result is thus insensitive to phase noise introduced before the splitters. The qubit state can be evaluated form IQ values on the fly with latency of 428 ns, allowing closed-loop feedback operations.

5.4.1 Resonator circle-fit

We use single tone spectroscopy to measure resonators frequency f_r, coupling Q_c, and internal Q_i quality factors. For resonator measured in reflection the complex reflection coefficient is [Kaj94]

$$S_{11} = \frac{(\omega_\mathrm{d}-\omega_\mathrm{r})^2+(\kappa_\mathrm{i}^2-\kappa_\mathrm{c}^2)/4+i\kappa_\mathrm{c}(\omega_\mathrm{d}-\omega_\mathrm{r})}{(\omega_\mathrm{d}-\omega_\mathrm{r})^2+(\kappa_\mathrm{i}^2+\kappa_\mathrm{c}^2)/4}, \tag{101}$$

where ω_d and ω_r are the drive and resonance frequencies, κ_i and κ_c are the internal and coupling resonator loss rates. Fig. 54 shows the measured response of the readout resonator coupled to a fluxonium atom with tunable Josephson energy (see section 2.5). Fluxonium atom was biased at zero magnetic field, where it is decoupled from the resonator. The readout power corresponds to $\bar{n} \approx 3$. The reflection coefficient traces a circle in the real-imaginary plane. We use the circle fitting routine developed by [Pro+15] to extract the resonator frequency $f_\mathrm{r} \approx 7.244$ GHz, and quality factors $Q_\mathrm{c} = 6.1{\times}10^3$, and $Q_\mathrm{i} = 4.9{\times}10^5$.

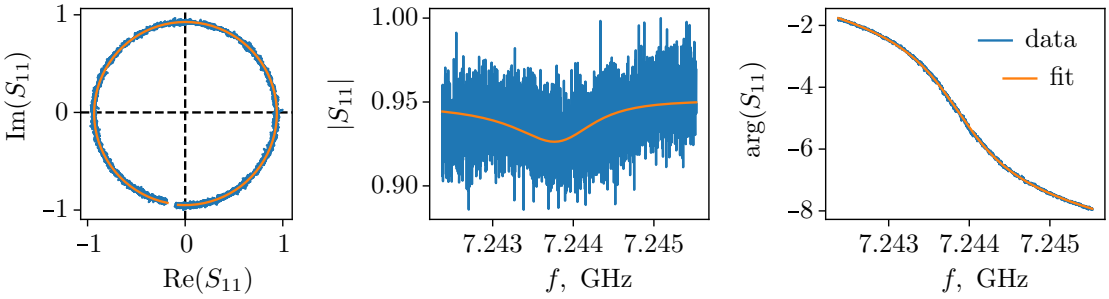

Figure 54: **Single tone spectroscopy of the readout resonator**. Blue and orange line indicate measured data and a result of the circle fit, respectively.

Bibliography

[AB63] Vinay Ambegaokar and Alexis Baratoff. "Tunneling Between Superconductors". In: *Phys. Rev. Lett.* 10 (11 June 1963), pp. 486–489. DOI: 10.1103/PhysRevLett.10.486.

[ACC66] B. Abeles, Roger W. Cohen, and G. W. Cullen. "Enhancement of Superconductivity in Metal Films". In: *Phys. Rev. Lett.* 17 (12 Sept. 1966), pp. 632–634. DOI: 10.1103/PhysRevLett.17.632.

[AW12] Alán Aspuru-Guzik and Philip Walther. "Photonic quantum simulators". In: *Nature Physics* 8.4 (Apr. 2012), pp. 285–291. ISSN: 1745-2481. DOI: 10.1038/nphys2253.

[Bar+14] R. Barends et al. "Superconducting quantum circuits at the surface code threshold for fault tolerance". In: *Nature* 508.7497 (Apr. 2014), pp. 500–503. ISSN: 1476-4687. DOI: 10.1038/nature13171.

[Bau+16] A. Baust et al. "Ultrastrong coupling in two-resonator circuit QED". In: *Phys. Rev. B* 93 (21 June 2016), p. 214501. DOI: 10.1103/PhysRevB.93.214501.

[BCS57] J. Bardeen, L. N. Cooper, and J. R. Schrieffer. "Theory of Superconductivity". In: *Phys. Rev.* 108 (5 Dec. 1957), pp. 1175–1204. DOI: 10.1103/PhysRev.108.1175.

[Bel+12] M. T. Bell et al. "Quantum Superinductor with Tunable Nonlinearity". In: *Phys. Rev. Lett.* 109 (13 Sept. 2012), p. 137003. DOI: 10.1103/PhysRevLett.109.137003.

[BEL00] Guido Burkard, Hans-Andreas Engel, and Daniel Loss. "Spintronics and Quantum Dots for Quantum Computing and Quantum Communication". In: *Fortschritte der Physik* 48.9-11 (2000), pp. 965–986. DOI: https://doi.org/10.1002/1521-3978(200009)48:9/11<965::AID-PROP965>3.0.CO;2-V.

[Ber+10] N. Bergeal et al. "Phase-preserving amplification near the quantum limit with a Josephson ring modulator". In: *Nature* 465.7294 (May 2010), pp. 64–68. ISSN: 1476-4687. DOI: 10.1038/nature09035.

[BGB08] M. Boissonneault, J. M. Gambetta, and A. Blais. "Nonlinear dispersive regime of cavity QED: The dressed dephasing model". In: *Phys. Rev. A* 77 (6 June 2008), 060305(R). DOI: 10.1103/PhysRevA.77.060305.

[BGB09] M. Boissonneault, J. M. Gambetta, and A. Blais. "Dispersive regime of circuit QED: Photon-dependent qubit dephasing and relaxation rates". In: *Phys. Rev. A* 79 (1 Jan. 2009), p. 013819. DOI: 10.1103/PhysRevA.79.013819.

[BK96] V. B. Braginsky and F. Ya. Khalili. "Quantum nondemolition measurements: the route from toys to tools". In: *Rev. Mod. Phys.* 68 (1 Jan. 1996), pp. 1–11. DOI: 10.1103/RevModPhys.68.1.

[Bla+04] A. Blais et al. "Cavity quantum electrodynamics for superconducting electrical circuits: An architecture for quantum computation". In: *Phys. Rev. A* 69 (6 June 2004), p. 062320. DOI: 10.1103/PhysRevA.69.062320.

[Bla+20] A. Blais et al. "Circuit Quantum Electrodynamics". In: *arXiv preprint arXiv:2005.12667* (2020). URL: https://arxiv.org/abs/2005.12667.

[BLZ01] Paul Bunyk, Konstantin Likharev, and Dmitry Zinoviev. "RSFQ technology: Physics and devices". In: *International Journal of High Speed Electronics and Systems* 11 (Mar. 2001). DOI: 10.1142/S012915640100085X.

[BN09] Iulia Buluta and Franco Nori. "Quantum Simulators". In: *Science* 326.5949 (2009), pp. 108–111. ISSN: 00368075, 10959203. URL: http://www.jstor.org/stable/40328587.

[BO96] Mark F. Bocko and Roberto Onofrio. "On the measurement of a weak classical force coupled to a harmonic oscillator: experimental progress". In: *Rev. Mod. Phys.* 68 (3 July 1996), pp. 755–799. DOI: 10.1103/RevModPhys.68.755.

[Boc+14] C. Bockstiegel et al. "Development of a Broadband NbTiN Traveling Wave Parametric Amplifier for MKID Readout". In: *Journal of Low Temperature Physics* 176.3 (Aug. 2014), pp. 476–482. ISSN: 1573-7357. DOI: 10.1007/s10909-013-1042-z.

[Bor+20] K. Borisov et al. "Superconducting granular aluminum resonators resilient to magnetic fields up to 1 Tesla". In: *Applied Physics Letters* 117.12 (2020), p. 120502. DOI: 10.1063/5.0018012.

[BTN15] P.-M. Billangeon, J. S. Tsai, and Y. Nakamura. "Circuit-QED-based scalable architectures for quantum information processing with superconducting qubits". In: *Phys. Rev. B* 91 (9 Mar. 2015), p. 094517. DOI: 10.1103/PhysRevB.91.094517.

[Buc+01] Ben C. Buchler et al. "Squeezing more from a quantum nondemolition measurement". In: *Phys. Rev. A* 65 (1 Dec. 2001), p. 011803. DOI: 10.1103/PhysRevA.65.011803.

[Bul+18] C. C. Bultink et al. "General method for extracting the quantum efficiency of dispersive qubit readout in circuit QED". In: *Applied Physics Letters* 112.9 (2018), p. 092601. DOI: 10.1063/1.5015954.

[BVT80] Vladimir B. Braginsky, Yuri I. Vorontsov, and Kip S. Thorne. "Quantum Nondemolition Measurements". In: *Science* 209.4456 (1980), pp. 547–557. DOI: 10.1126/science.209.4456.547.

[Car+21] L. Cardani et al. "Reducing the impact of radioactivity on quantum circuits in a deep-underground facility". In: *Nature Communications* 12.1 (May 2021), p. 2733. ISSN: 2041-1723. DOI: 10.1038/s41467-021-23032-z.

[Cas+08] M. A. Castellanos-Beltran et al. "Amplification and squeezing of quantum noise with a tunable Josephson metamaterial". In: *Nature Physics* 4.12 (Dec. 2008), pp. 929–931. DOI: 10.1038/nphys1090.

[Cat+11] G. Catelani et al. "Quasiparticle Relaxation of Superconducting Qubits in the Presence of Flux". In: *Phys. Rev. Lett.* 106 (7 Feb. 2011), p. 077002. DOI: 10.1103/PhysRevLett.106.077002.

[Cav+80] Carlton M. Caves et al. "On the measurement of a weak classical force coupled to a quantum-mechanical oscillator. I. Issues of principle". In: *Rev. Mod. Phys.* 52 (2 Apr. 1980), pp. 341–392. DOI: 10.1103/RevModPhys.52.341.

[Cav82] Carlton M. Caves. "Quantum limits on noise in linear amplifiers". In: *Phys. Rev. D* 26 (8 Oct. 1982), pp. 1817–1839. DOI: 10.1103/PhysRevD.26.1817.

[Cle+10] A. A. Clerk et al. "Introduction to quantum noise, measurement, and amplification". In: *Rev. Mod. Phys.* 82 (2 Apr. 2010), pp. 1155–1208. DOI: 10.1103/RevModPhys.82.1155.

[CW08] John Clarke and Frank K. Wilhelm. "Superconducting quantum bits". In: *Nature* 453.7198 (June 2008), pp. 1031–1042. ISSN: 1476-4687. DOI: 10.1038/nature07128.

[Das+20] R. Dassonneville et al. "Fast High-Fidelity Quantum Nondemolition Qubit Readout via a Nonperturbative Cross-Kerr Coupling". In: *Phys. Rev. X* 10 (1 Feb. 2020), p. 011045. DOI: 10.1103/PhysRevX.10.011045.

[Day+03] Peter K. Day et al. "A broadband superconducting detector suitable for use in large arrays". In: *Nature* 425.6960 (Oct. 2003), pp. 817–821. ISSN: 1476-4687. DOI: 10.1038/nature02037.

[DBB15] Nicolas Didier, Jérôme Bourassa, and Alexandre Blais. "Fast Quantum Nondemolition Readout by Parametric Modulation of Longitudinal Qubit-Oscillator Interaction". In: *Phys. Rev. Lett.* 115 (20 Nov. 2015), p. 203601. DOI: 10.1103/PhysRevLett.115.203601.

[DCM92] J. Dalibard, Y. Castin, and K. Mølmer. "Wave-function approach to dissipative processes in quantum optics". In: *Phys. Rev. Lett.* 68 (5 Feb. 1992), pp. 580–583. DOI: 10.1103/PhysRevLett.68.580.

[Deu+73] G. Deutscher et al. "Transition to zero dimensionality in granular aluminum superconducting films". In: *Journal of Low Temperature Physics* 10.1 (Jan. 1973), pp. 231–243. ISSN: 1573-7357. DOI: 10.1007/BF00655256.

[Dev97] M. H. Devoret. *Quantum Fluctuations in Electrical Circuits*. S. Reynaud, E. Giacobino, and J. Zinn-Justin, Quantum fluctuations conference; Les Houches (France), 1997. ISBN: 0-444-82593-2.

[DG81] R. C. Dynes and J. P. Garno. "Metal-Insulator Transition in Granular Aluminum". In: *Phys. Rev. Lett.* 46 (2 Jan. 1981), pp. 137–140. DOI: 10.1103/PhysRevLett.46.137.

[DiV95] David P. DiVincenzo. "Quantum Computation". In: *Science* 270.5234 (1995), pp. 255–261. DOI: 10.1126/science.270.5234.255.

[DM04] Michel H. Devoret and John M. Martinis. "Implementing Qubits with Superconducting Integrated Circuits". In: *Quantum Information Processing* 3.1 (Oct. 2004), pp. 163–203. ISSN: 1573-1332. DOI: 10.1007/s11128-004-3101-5.

[DRC17] C. L. Degen, F. Reinhard, and P. Cappellaro. “Quantum sensing”. In: *Rev. Mod. Phys.* 89 (3 July 2017), p. 035002. DOI: 10.1103/RevModPhys.89.035002.

[DS13] M. H. Devoret and R. J. Schoelkopf. “Superconducting Circuits for Quantum Information: An Outlook”. In: *Science* 339.6124 (2013), pp. 1169–1174. DOI: 10.1126/science.1231930.

[Dut+07] M. V. Gurudev Dutt et al. “Quantum Register Based on Individual Electronic and Nuclear Spin Qubits in Diamond”. In: *Science* 316.5829 (2007), pp. 1312–1316. DOI: 10.1126/science.1139831.

[DZR92] R. Dum, P. Zoller, and H. Ritsch. “Monte Carlo simulation of the atomic master equation for spontaneous emission”. In: *Phys. Rev. A* 45 (7 Apr. 1992), pp. 4879–4887. DOI: 10.1103/PhysRevA.45.4879.

[EJ96] Artur Ekert and Richard Jozsa. “Quantum computation and Shor’s factoring algorithm”. In: *Rev. Mod. Phys.* 68 (3 July 1996), pp. 733–753. DOI: 10.1103/RevModPhys.68.733. URL: https://link.aps.org/doi/10.1103/RevModPhys.68.733.

[EW14] C. Eichler and A. Wallraff. “Controlling the dynamic range of a Josephson parametric amplifier”. In: *EPJ Quantum Technology* 1.1 (2014), p. 2. ISSN: 2196-0763. DOI: 10.1140/epjqt2.

[FD87] T. A. Fulton and G. J. Dolan. “Observation of single-electron charging effects in small tunnel junctions”. In: *Phys. Rev. Lett.* 59 (1 July 1987), pp. 109–112. DOI: 10.1103/PhysRevLett.59.109.

[Fow+12] Austin G. Fowler et al. “Surface codes: Towards practical large-scale quantum computation”. In: *Phys. Rev. A* 86 (3 Sept. 2012), p. 032324. DOI: 10.1103/PhysRevA.86.032324.

[FSG09] Austin G. Fowler, Ashley M. Stephens, and Peter Groszkowski. “High-threshold universal quantum computation on the surface code”. In: *Phys. Rev. A* 80 (5 Nov. 2009), p. 052312. DOI: 10.1103/PhysRevA.80.052312.

[Gam+06] Jay Gambetta et al. “Qubit-photon interactions in a cavity: Measurement-induced dephasing and number splitting”. In: *Phys. Rev. A* 74 (4 Oct. 2006), p. 042318. DOI: 10.1103/PhysRevA.74.042318.

[GAN14] I. M. Georgescu, S. Ashhab, and Franco Nori. “Quantum simulation”. In: *Rev. Mod. Phys.* 86 (1 Mar. 2014), pp. 153–185. DOI: 10.1103/RevModPhys.86.153.

[Geb+20] R. Gebauer et al. “State preparation of a fluxonium qubit with feedback from a custom FPGA-based platform”. In: *AIP Conference Proceedings* 2241.1 (2020), p. 020015. DOI: 10.1063/5.0011721.

[Gee+89] L. J. Geerligs et al. “Charging effects and quantum coherence in regular Josephson junction arrays”. In: *Phys. Rev. Lett.* 63 (3 July 1989), pp. 326–329. DOI: 10.1103/PhysRevLett.63.326.

[GLM04] Vittorio Giovannetti, Seth Lloyd, and Lorenzo Maccone. “Quantum-Enhanced Measurements: Beating the Standard Quantum Limit”. In: *Science* 306.5700 (2004), pp. 1330–1336. DOI: 10.1126/science.1104149.

[GLP98] Philippe Grangier, Juan Ariel Levenson, and Jean-Philippe Poizat. “Quantum non-demolition measurements in optics”. In: *Nature* 396.6711 (Dec. 1998), pp. 537–542. DOI: 10.1038/25059.

[Grü+17] Lukas Grünhaupt et al. “An argon ion beam milling process for native AlOx layers enabling coherent superconducting contacts”. In: *Applied Physics Letters* 111.7 (2017), p. 072601. DOI: 10.1063/1.4990491.

[Grü+18] Lukas Grünhaupt et al. “Loss Mechanisms and Quasiparticle Dynamics in Superconducting Microwave Resonators Made of Thin-Film Granular Aluminum”. In: *Phys. Rev. Lett.* 121 (11 Sept. 2018), p. 117001. DOI: 10.1103/PhysRevLett.121.117001.

[Grü+19] Lukas Grünhaupt et al. “Granular aluminium as a superconducting material for high-impedance quantum circuits”. In: *Nature Materials* 18.8 (2019), pp. 816–819. ISSN: 1476-4660. DOI: 10.1038/s41563-019-0350-3.

[Grü19] L. Grünhaupt. *Granular Aluminum Superinductors. Dissertation.* Karlsruhe Institute of Technology, Karlsruhe, 2019. ISBN: 978-3-7315-0956-1.

[GT07] Nicolas Gisin and Rob Thew. “Quantum communication”. In: *Nature Photonics* 1.3 (Mar. 2007), pp. 165–171. ISSN: 1749-4893. DOI: 10.1038/nphoton.2007.22.

[Gus+21] Daria Gusenkova et al. “Quantum Nondemolition Dispersive Readout of a Superconducting Artificial Atom Using Large Photon Numbers”. In: *Phys. Rev. Applied* 15 (6 June 2021), p. 064030. DOI: 10.1103/PhysRevApplied.15.064030.

[Gye+21] András Gyenis et al. “Experimental Realization of a Protected Superconducting Circuit Derived from the 0–π Qubit”. In: *PRX Quantum* 2 (1 Mar. 2021), p. 010339. DOI: 10.1103/PRXQuantum.2.010339.

[Hah50] E. L. Hahn. “Spin Echoes”. In: *Phys. Rev.* 80 (4 Nov. 1950), pp. 580–594. DOI: 10.1103/PhysRev.80.580.

[Hat+13] M. Hatridge et al. “Quantum back-action of an individual variable-strength measurement”. In: *Science* 339.6116 (2013), pp. 178–181. DOI: 10.1126/science.1226897.

[Hay+20] M. Hays et al. “Continuous monitoring of a trapped superconducting spin”. In: *Nature Physics* 16.11 (Nov. 2020), pp. 1103–1107. ISSN: 1745-2481. DOI: 10.1038/s41567-020-0952-3.

[Haz+19] T. M. Hazard et al. “Nanowire Superinductance Fluxonium Qubit”. In: *Phys. Rev. Lett.* 122 (1 Jan. 2019), p. 010504. DOI: 10.1103/PhysRevLett.122.010504.

[Hen+19] Fabio Henriques et al. “Phonon traps reduce the quasiparticle density in superconducting circuits”. In: *Applied Physics Letters* 115.21 (2019), p. 212601. DOI: 10.1063/1.5124967.

[Her+10] J. B. Hertzberg et al. “Back-action-evading measurements of nanomechanical motion”. In: *Nature Physics* 6.3 (Mar. 2010), pp. 213–217. ISSN: 1745-2481. DOI: 10.1038/nphys1479.

[Hou+08] A. A. Houck et al. “Controlling the Spontaneous Emission of a Superconducting Transmon Qubit”. In: *Phys. Rev. Lett.* 101 (8 Aug. 2008), p. 080502. DOI: 10.1103/PhysRevLett.101.080502.

[HR06] Serge Haroche and J-M Raimond. *Exploring the quantum: atoms, cavities, and photons*. Oxford university press, 2006.

[HRB08] H. Häffner, C.F. Roos, and R. Blatt. “Quantum computing with trapped ions”. In: *Physics Reports* 469.4 (2008), pp. 155–203. ISSN: 0370-1573. DOI: https://doi.org/10.1016/j.physrep.2008.09.003.

[HTK12] Andrew A. Houck, Hakan E. Türeci, and Jens Koch. “On-chip quantum simulation with superconducting circuits”. In: *Nature Physics* 8.4 (Apr. 2012), pp. 292–299. ISSN: 1745-2481. DOI: 10.1038/nphys2251.

[Iof+02] L. B. Ioffe et al. “Topologically protected quantum bits using Josephson junction arrays”. In: *Nature* 415.6871 (Jan. 2002), pp. 503–506. ISSN: 1476-4687. DOI: 10.1038/415503a.

[Ivr+14] Yachin Ivry et al. “Universal scaling of the critical temperature for thin films near the superconducting-to-insulating transition”. In: *Phys. Rev. B* 90 (21 Dec. 2014), p. 214515. DOI: 10.1103/PhysRevB.90.214515.

[Jac14] Kurt Jacobs. “Quantum Measurement Theory and its Applications”. In: *Cambridge University Press* (2014). URL: https://doi.org/10.1017/CBO9781139179027.

[Jan+15] C Janvier et al. “Coherent manipulation of Andreev states in superconducting atomic contacts”. In: *Science* 349.6253 (2015), pp. 1199–1202. DOI: 10.1126/science.aab2179.

[Joh+12] J. E. Johnson et al. “Heralded State Preparation in a Superconducting Qubit”. In: *Phys. Rev. Lett.* 109 (5 Aug. 2012), p. 050506. DOI: 10.1103/PhysRevLett.109.050506.

[Jül19] Jülich Supercomputing Centre. “JUWELS: Modular Tier-0/1 Supercomputer at the Jülich Supercomputing Centre”. In: *Journal of large-scale research facilities* 5 (2019), A135. DOI: 10.17815/jlsrf-5-171.

[Kaj94] D. Kajfez. “Linear fractional curve fitting for measurement of high Q factors”. In: *IEEE Transactions on Microwave Theory and Techniques* 42.7 (1994), pp. 1149–1153. DOI: 10.1109/22.299749.

[Kar+19] K. Karatsu et al. “Mitigation of cosmic ray effect on microwave kinetic inductance detector arrays”. In: *Applied Physics Letters* 114.3 (2019), p. 032601. DOI: 10.1063/1.5052419.

[Ker13] Andrew J Kerman. "Quantum information processing using quasiclassical electromagnetic interactions between qubits and electrical resonators". In: *New Journal of Physics* 15.12 (2013), p. 123011. DOI: 10.1088/1367-2630/15/12/123011.

[KH91] L. S. Kuzmin and D. B. Haviland. "Observation of the Bloch oscillations in an ultrasmall Josephson junction". In: *Phys. Rev. Lett.* 67 (20 Nov. 1991), pp. 2890–2893. DOI: 10.1103/PhysRevLett.67.2890.

[Koc+07] Jens Koch et al. "Charge-insensitive qubit design derived from the Cooper pair box". In: *Phys. Rev. A* 76 (4 Oct. 2007), p. 042319. DOI: 10.1103/PhysRevA.76.042319.

[Kou+18a] A. Kou et al. "Simultaneous Monitoring of Fluxonium Qubits in a Waveguide". In: *Phys. Rev. Applied* 9 (6 June 2018), p. 064022. DOI: 10.1103/PhysRevApplied.9.064022.

[Kou+18b] M. Kounalakis et al. "Tuneable hopping and nonlinear cross-Kerr interactions in a high-coherence superconducting circuit". In: *npj Quantum Information* 4.1 (Aug. 2018), p. 38. ISSN: 2056-6387. DOI: 10.1038/s41534-018-0088-9.

[Les+19] Raphaël Lescanne et al. "Escape of a Driven Quantum Josephson Circuit into Unconfined States". In: *Phys. Rev. Applied* 11 (1 Jan. 2019), p. 014030. DOI: 10.1103/PhysRevApplied.11.014030.

[Lev+14] E. M. Levenson-Falk et al. "Single-Quasiparticle Trapping in Aluminum Nanobridge Josephson Junctions". In: *Phys. Rev. Lett.* 112 (4 Jan. 2014), p. 047002. DOI: 10.1103/PhysRevLett.112.047002.

[Lev+19] F. Levy-Bertrand et al. "Electrodynamics of granular aluminum from superconductor to insulator: Observation of collective superconducting modes". In: *Phys. Rev. B* 99 (9 Mar. 2019), p. 094506. DOI: 10.1103/PhysRevB.99.094506.

[Liu+14] Yanbing Liu et al. "High fidelity readout of a transmon qubit using a superconducting low-inductance undulatory galvanometer microwave amplifier". In: *New Journal of Physics* 16.11 (Nov. 2014), p. 113008. DOI: 10.1088/1367-2630/16/11/113008.

[Lon+07] Gui-lu Long et al. "Quantum secure direct communication and deterministic secure quantum communication". In: *Frontiers of Physics in China* 2.3 (July 2007), pp. 251–272. ISSN: 1673-3606. DOI: 10.1007/s11467-007-0050-3.

[LS91] K.K. Likharev and V.K. Semenov. "RSFQ logic/memory family: a new Josephson-junction technology for sub-terahertz-clock-frequency digital systems". In: *IEEE Transactions on Applied Superconductivity* 1.1 (1991), pp. 3–28. DOI: 10.1109/77.80745.

[LSY89] A. La Porta, R. E. Slusher, and B. Yurke. "Back-Action Evading Measurements of an Optical Field Using Parametric Down Conversion". In: *Phys. Rev. Lett.* 62 (1 Jan. 1989), pp. 28–31. DOI: 10.1103/PhysRevLett.62.28.

[Maj+07] J. Majer et al. "Coupling superconducting qubits via a cavity bus". In: *Nature* 449.7161 (Sept. 2007), pp. 443–447. ISSN: 1476-4687. DOI: 10.1038/nature06184.

[Mal+09] François Mallet et al. "Single-shot qubit readout in circuit quantum electrodynamics". In: *Nature Physics* 5.11 (Nov. 2009), pp. 791–795. ISSN: 1745-2481. DOI: 10.1038/nphys1400.

[Mal+18] N. Maleeva et al. "Circuit quantum electrodynamics of granular aluminum resonators". In: *Nature Communications* 9.1 (Sept. 2018), p. 3889. DOI: 10.1038/s41467-018-06386-9.

[Man+09] V. E. Manucharyan et al. "Fluxonium: Single cooper-pair circuit free of charge offsets". In: *Science* 326.5949 (2009), pp. 113–116. DOI: 10.1126/science.1175552.

[Mar21] John M. Martinis. *Saving superconducting quantum processors from qubit decay and correlated errors generated by gamma and cosmic rays.* 2021. arXiv: 2012.06137 [quant-ph].

[Mas+12] N. A. Masluk et al. "Microwave Characterization of Josephson Junction Arrays: Implementing a Low Loss Superinductance". In: *Phys. Rev. Lett.* 109 (13 Sept. 2012), p. 137002. DOI: 10.1103/PhysRevLett.109.137002.

[MB58] D. C. Mattis and J. Bardeen. "Theory of the Anomalous Skin Effect in Normal and Superconducting Metals". In: *Phys. Rev.* 111 (2 July 1958), pp. 412–417. DOI: 10.1103/PhysRev.111.412.

[Min+19] Z. K. Minev et al. “To catch and reverse a quantum jump mid-flight”. In: *Nature* 570.7760 (June 2019), pp. 200–204. ISSN: 1476-4687. DOI: 10.1038/s41586-019-1287-z.

[MLG02] K. A. Matveev, A. I. Larkin, and L. I. Glazman. “Persistent Current in Superconducting Nanorings”. In: *Phys. Rev. Lett.* 89 (9 Aug. 2002), p. 096802. DOI: 10.1103/PhysRevLett.89.096802.

[MPT20] M. Malekakhlagh, A. Petrescu, and H. E. Türeci. “Lifetime renormalization of weakly anharmonic superconducting qubits. I. Role of number nonconserving terms”. In: *Phys. Rev. B* 101 (13 Apr. 2020), p. 134509. DOI: 10.1103/PhysRevB.101.134509.

[NC10] Michael A. Nielsen and Isaac L. Chuang. *Quantum Computation and Quantum Information: 10th Anniversary Edition*. Cambridge University Press, 2010. DOI: 10.1017/CBO9780511976667.

[Nie+74] Jürgen Niemeyer et al. “EINE EINFACHE METHODE ZUR HERSTELLUNG KLEINSTER JOSEPHSON-ELEMENTE.” In: (1974).

[Noa+13] Y. Noat et al. “Unconventional superconductivity in ultrathin superconducting NbN films studied by scanning tunneling spectroscopy”. In: *Phys. Rev. B* 88 (1 July 2013), p. 014503. DOI: 10.1103/PhysRevB.88.014503.

[NPT99] Y. Nakamura, Yu. A. Pashkin, and J. S. Tsai. “Coherent control of macroscopic quantum states in a single-Cooper-pair box”. In: *Nature* 398.6730 (Apr. 1999), pp. 786–788. ISSN: 1476-4687. DOI: 10.1038/19718.

[Ofe+16] Nissim Ofek et al. “Extending the lifetime of a quantum bit with error correction in superconducting circuits”. In: *Nature* 536.7617 (Aug. 2016), pp. 441–445. ISSN: 1476-4687. DOI: 10.1038/nature18949.

[Per+20] M. Peruzzo et al. “Surpassing the Resistance Quantum with a Geometric Superinductor”. In: *Phys. Rev. Applied* 14 (4 Oct. 2020), p. 044055. DOI: 10.1103/PhysRevApplied.14.044055.

[Pet+18] Alexandru Petrescu et al. “Fluxon-based quantum simulation in circuit QED”. In: *Phys. Rev. B* 98 (17 Nov. 2018), p. 174505. DOI: 10.1103/PhysRevB.98.174505.

[Pic+08] T. Picot et al. “Role of relaxation in the quantum measurement of a superconducting qubit using a nonlinear oscillator”. In: *Phys. Rev. B* 78 (13 Oct. 2008), p. 132508. DOI: 10.1103/PhysRevB.78.132508.

[Pit+20] Marta Pita-Vidal et al. “Gate-Tunable Field-Compatible Fluxonium”. In: *Phys. Rev. Applied* 14 (6 Dec. 2020), p. 064038. DOI: 10.1103/PhysRevApplied.14.064038.

[PMT20] A. Petrescu, M. Malekakhlagh, and H. E. Türeci. “Lifetime renormalization of driven weakly anharmonic superconducting qubits. II. The readout problem”. In: *Phys. Rev. B* 101 (13 Apr. 2020), p. 134510. DOI: 10.1103/PhysRevB.101.134510.

[Pop+10] I. M. Pop et al. “Measurement of the effect of quantum phase slips in a Josephson junction chain”. In: *Nature Physics* 6.8 (Aug. 2010), pp. 589–592. ISSN: 1745-2481. DOI: 10.1038/nphys1697.

[Pop+14] Ioan M. Pop et al. “Coherent suppression of electromagnetic dissipation due to superconducting quasiparticles”. In: *Nature* 508.7496 (Apr. 2014), pp. 369–372. ISSN: 1476-4687. DOI: 10.1038/nature13017.

[Poz11] David M Pozar. *Microwave engineering*. John Wiley & Sons, 2011, p. 311. ISBN: 978-0-470-63155-3.

[Pra+16] Uwe S. Pracht et al. “Enhanced Cooper pairing versus suppressed phase coherence shaping the superconducting dome in coupled aluminum nanograins”. In: *Phys. Rev. B* 93 (10 Mar. 2016), p. 100503. DOI: 10.1103/PhysRevB.93.100503.

[Pro+15] S. Probst et al. “Efficient and robust analysis of complex scattering data under noise in microwave resonators”. In: *Review of Scientific Instruments* 86.2 (2015), p. 024706. DOI: 10.1063/1.4907935.

[Pur46] E. M. Purcell. “Spontaneous emission probabilities at radio frequencies”. In: *Phys. Rev.* 69 (11-12 June 1946), pp. 674–674. DOI: 10.1103/PhysRev.69.674.2.

[Ram50] Norman F. Ramsey. “A Molecular Beam Resonance Method with Separated Oscillating Fields”. In: *Phys. Rev.* 78 (6 June 1950), pp. 695–699. DOI: 10.1103/PhysRev.78.695.

[RBH01a] J. M. Raimond, M. Brune, and S. Haroche. "Manipulating quantum entanglement with atoms and photons in a cavity". In: *Rev. Mod. Phys.* 73 (3 Aug. 2001), pp. 565–582. DOI: 10.1103/RevModPhys.73.565. URL: https://link.aps.org/doi/10.1103/RevModPhys.73.565.

[RBH01b] J. M. Raimond, M. Brune, and S. Haroche. "Manipulating quantum entanglement with atoms and photons in a cavity". In: *Rev. Mod. Phys.* 73 (3 Aug. 2001), pp. 565–582. DOI: 10.1103/RevModPhys.73.565.

[RD16a] Susanne Richer and David DiVincenzo. "Circuit design implementing longitudinal coupling: A scalable scheme for superconducting qubits". In: *Phys. Rev. B* 93 (13 Apr. 2016), p. 134501. DOI: 10.1103/PhysRevB.93.134501.

[RD16b] Ananda Roy and Michel Devoret. "Introduction to parametric amplification of quantum signals with Josephson circuits". In: *Comptes Rendus Physique* 17.7 (2016). Quantum microwaves / Micro-ondes quantiques, pp. 740–755. ISSN: 1631-0705. DOI: https://doi.org/10.1016/j.crhy.2016.07.012.

[RD21] Roman-Pascal Riwar and David P. DiVincenzo. *Circuit quantization with time-dependent magnetic fields for realistic geometries*. 2021. arXiv: 2103.03577 [cond-mat.mes-hall].

[Ric+17] Susanne Richer et al. "Inductively shunted transmon qubit with tunable transverse and longitudinal coupling". In: *Phys. Rev. B* 96 (17 Nov. 2017), p. 174520. DOI: 10.1103/PhysRevB.96.174520.

[Ric18] Susanne Richer. *Design of an inductively shunted transmon qubit with tunable transverse and longitudinal coupling. Dissertation*. RWTH Aachen University, 2018. DOI: 10.18154/RWTH-2018-223773.

[Roc+92] J. F. Roch et al. "Quantum non-demolition measurements in optics: a review and some recent experimental results". In: *Applied Physics B* 55.3 (Sept. 1992), pp. 291–297. ISSN: 1432-0649. DOI: 10.1007/BF00325017.

[Roc+97] J.-F. Roch et al. "Quantum Nondemolition Measurements using Cold Trapped Atoms". In: *Phys. Rev. Lett.* 78 (4 Jan. 1997), pp. 634–637. DOI: 10.1103/PhysRevLett.78.634.

[RPH13] G. Rastelli, I. M. Pop, and F. W. J. Hekking. "Quantum phase slips in Josephson junction rings". In: *Phys. Rev. B* 87 (17 May 2013), p. 174513. DOI: 10.1103/PhysRevB.87.174513.

[Sam+16] N. Samkharadze et al. "High-Kinetic-Inductance Superconducting Nanowire Resonators for Circuit QED in a Magnetic Field". In: *Phys. Rev. Applied* 5 (4 Apr. 2016), p. 044004. DOI: 10.1103/PhysRevApplied.5.044004.

[San+16] D. Sank et al. "Measurement-Induced State Transitions in a Superconducting Qubit: Beyond the Rotating Wave Approximation". In: *Phys. Rev. Lett.* 117 (19 Nov. 2016), p. 190503. DOI: 10.1103/PhysRevLett.117.190503.

[Sch+13] M J Schwarz et al. "Gradiometric flux qubits with a tunable gap". In: *New Journal of Physics* 15.4 (Apr. 2013), p. 045001. DOI: 10.1088/1367-2630/15/4/045001.

[Sli+12] D. H. Slichter et al. "Measurement-Induced Qubit State Mixing in Circuit QED from Up-Converted Dephasing Noise". In: *Phys. Rev. Lett.* 109 (15 Oct. 2012), p. 153601. DOI: 10.1103/PhysRevLett.109.153601.

[Sli+16] D H Slichter et al. "Quantum Zeno effect in the strong measurement regime of circuit quantum electrodynamics". In: *New Journal of Physics* 18.5 (May 2016), p. 053031. DOI: 10.1088/1367-2630/18/5/053031.

[Smi+16] W. C. Smith et al. "Quantization of inductively shunted superconducting circuits". In: *Phys. Rev. B* 94 (14 Oct. 2016), p. 144507. DOI: 10.1103/PhysRevB.94.144507.

[Smi+20] W. C. Smith et al. "Superconducting circuit protected by two-Cooper-pair tunneling". In: *npj Quantum Information* 6.1 (Jan. 2020), p. 8. ISSN: 2056-6387. DOI: 10.1038/s41534-019-0231-2.

[Som+21] Aaron Somoroff et al. *Millisecond coherence in a superconducting qubit*. 2021. arXiv: 2103.08578 [quant-ph].

[SWM10] M. Saffman, T. G. Walker, and K. Mølmer. "Quantum information with Rydberg atoms". In: *Rev. Mod. Phys.* 82 (3 Aug. 2010), pp. 2313–2363. DOI: 10.1103/RevModPhys.82.2313.

[Tak+21] I. Takmakov et al. “Minimizing the Discrimination Time for Quantum States of an Artificial Atom”. In: *Phys. Rev. Applied* 15 (6 June 2021), p. 064029. DOI: 10.1103/PhysRevApplied.15.064029.

[Ter15] Barbara M. Terhal. “Quantum error correction for quantum memories”. In: *Rev. Mod. Phys.* 87 (2 Apr. 2015), pp. 307–346. DOI: 10.1103/RevModPhys.87.307.

[Tin04] Michael Tinkham. *Introduction to superconductivity*. Courier Corporation, 2004, pp. 98, 123–125, 127–130.

[Tou+19] S. Touzard et al. “Gated Conditional Displacement Readout of Superconducting Qubits”. In: *Phys. Rev. Lett.* 122 (8 Feb. 2019), p. 080502. DOI: 10.1103/PhysRevLett.122.080502.

[Tra12] Andreas Trabesinger. “Quantum simulation”. In: *Nature Physics* 8.4 (Apr. 2012), pp. 263–263. ISSN: 1745-2481. DOI: 10.1038/nphys2258.

[Val+19] Francesco Valenti et al. “Interplay Between Kinetic Inductance, Nonlinearity, and Quasiparticle Dynamics in Granular Aluminum Microwave Kinetic Inductance Detectors”. In: *Phys. Rev. Applied* 11 (5 May 2019), p. 054087. DOI: 10.1103/PhysRevApplied.11.054087.

[Vis+11] P. J. de Visser et al. “Number Fluctuations of Sparse Quasiparticles in a Superconductor”. In: *Phys. Rev. Lett.* 106 (16 Apr. 2011), p. 167004. DOI: 10.1103/PhysRevLett.106.167004.

[Vis+16] M. R. Vissers et al. “Low-noise kinetic inductance traveling-wave amplifier using three-wave mixing”. In: *Applied Physics Letters* 108.1 (2016), p. 012601. DOI: 10.1063/1.4937922.

[Voo+14] U. Vool et al. “Non-Poissonian Quantum Jumps of a Fluxonium Qubit due to Quasiparticle Excitations”. In: *Phys. Rev. Lett.* 113 (24 Dec. 2014), p. 247001. DOI: 10.1103/PhysRevLett.113.247001.

[Voo+18] U. Vool et al. “Driving Forbidden Transitions in the Fluxonium Artificial Atom”. In: *Phys. Rev. Applied* 9 (5 May 2018), p. 054046. DOI: 10.1103/PhysRevApplied.9.054046.

[VSS11] R. Vijay, D. H. Slichter, and I. Siddiqi. “Observation of Quantum Jumps in a Superconducting Artificial Atom”. In: *Phys. Rev. Lett.* 106 (11 Mar. 2011), p. 110502. DOI: 10.1103/PhysRevLett.106.110502.

[Wal+04] A. Wallraff et al. “Strong coupling of a single photon to a superconducting qubit using circuit quantum electrodynamics”. In: *Nature* 431.7005 (2004), pp. 162–167. URL: https://doi.org/10.1038/nature02851.

[Wal+17] T. Walter et al. “Rapid High-Fidelity Single-Shot Dispersive Readout of Superconducting Qubits”. In: *Phys. Rev. Applied* 7 (5 May 2017), p. 054020. DOI: 10.1103/PhysRevApplied.7.054020.

[Wan+14] C. Wang et al. “Measurement and control of quasiparticle dynamics in a superconducting qubit”. In: *Nature Communications* 5.1 (Dec. 2014), p. 5836. ISSN: 2041-1723. DOI: 10.1038/ncomms6836.

[Web68] J. Weber. “Gravitational-Wave-Detector Events”. In: *Phys. Rev. Lett.* 20 (23 June 1968), pp. 1307–1308. DOI: 10.1103/PhysRevLett.20.1307.

[Wei+15] T. Weißl et al. “Kerr coefficients of plasma resonances in Josephson junction chains”. In: *Phys. Rev. B* 92 (10 Sept. 2015), p. 104508. DOI: 10.1103/PhysRevB.92.104508.

[Wen17] G Wendin. “Quantum information processing with superconducting circuits: a review”. In: *Reports on Progress in Physics* 80.10 (Sept. 2017), p. 106001. DOI: 10.1088/1361-6633/aa7e1a.

[Whi+15] T. C. White et al. “Traveling wave parametric amplifier with Josephson junctions using minimal resonator phase matching”. In: *Applied Physics Letters* 106.24 (June 2015), p. 242601. ISSN: 0003-6951. DOI: 10.1063/1.4922348.

[Wil+21] C. D. Wilen et al. “Correlated charge noise and relaxation errors in superconducting qubits”. In: *Nature* 594.7863 (June 2021), pp. 369–373. ISSN: 1476-4687. DOI: 10.1038/s41586-021-03557-5.

[Win+20a] P. Winkel et al. “Nondegenerate Parametric Amplifiers Based on Dispersion-Engineered Josephson-Junction Arrays”. In: *Phys. Rev. Applied* 13 (2 Feb. 2020), p. 024015. DOI: 10.1103/PhysRevApplied.13.024015.

[Win+20b] Patrick Winkel et al. “Implementation of a Transmon Qubit Using Superconducting Granular Aluminum”. In: *Phys. Rev. X* 10 (3 Aug. 2020), p. 031032. DOI: 10.1103/PhysRevX.10.031032.

[Xia+13] Ze-Liang Xiang et al. “Hybrid quantum circuits: Superconducting circuits interacting with other quantum systems”. In: *Rev. Mod. Phys.* 85 (2 Apr. 2013), pp. 623–653. DOI: 10.1103/RevModPhys.85.623.

[Yao+12] N. Y. Yao et al. “Scalable architecture for a room temperature solid-state quantum information processor”. In: *Nature Communications* 3.1 (Apr. 2012), p. 800. ISSN: 2041-1723. DOI: 10.1038/ncomms1788.

[YD84] Bernard Yurke and John S. Denker. “Quantum network theory”. In: *Phys. Rev. A* 29 (3 Mar. 1984), pp. 1419–1437. DOI: 10.1103/PhysRevA.29.1419.

[Yos+17] F. Yoshihara et al. “Superconducting qubit–oscillator circuit beyond the ultrastrong-coupling regime”. In: *Nature Physics* 13.1 (Jan. 2017), pp. 44–47. ISSN: 1745-2481. DOI: 10.1038/nphys3906.

[YSK19] Xinyuan You, J. A. Sauls, and Jens Koch. “Circuit quantization in the presence of time-dependent external flux”. In: *Phys. Rev. B* 99 (17 May 2019), p. 174512. DOI: 10.1103/PhysRevB.99.174512.

[Zoe+17] D. Zoepfl et al. “Characterization of low loss microstrip resonators as a building block for circuit QED in a 3D waveguide”. In: *AIP Advances* 7.8 (2017), p. 085118. DOI: 10.1063/1.4992070.

List of publications

1. Reducing the impact of radioactivity on quantum circuits in a deep-underground facility. L. Cardani, F. Valenti, N. Casali, G. Catelani, T. Charpentier, M. Clemenza, I. Colantoni, A. Cruciani, G. D'Imperio, L. Gironi, L. Grünhaupt, D. Gusenkova, F. Henriques, M. Lagoin, M. Martinez, G. Pettinari, C. Rusconi, O. Sander, C. Tomei, A. V. Ustinov, M. Weber, W. Wernsdorfer, M. Vignati, S. Pirro & I. M. Pop. In: *Nature Communications 12.1 (May 2021), p. 2733.*

2. Minimizing the discrimination time for quantum states of an artificial atom. I. Takmakov, P. Winkel, F. Foroughi, L. Planat, D. Gusenkova, M. Spiecker, D. Rieger, L. Grünhaupt, A. V. Ustinov, W. Wernsdorfer, I. M. Pop, and N. Roch. In: *Phys. Rev. Applied 15 (6 June 2021), p. 064029.*

3. Quantum non-demolition dispersive readout of a superconducting artificial atom using large photon numbers. D. Gusenkova, M. Spiecker, R. Gebauer, M. Willsch, D. Willsch, F. Valenti, N. Karcher, L. Grünhaupt, I. Takmakov, P. Winkel, D. Rieger, A. V. Ustinov, N. Roch, W. Wernsdorfer, K. Michielsen, O. Sander, and I. M. Pop. In: *Phys. Rev. Applied 15 (6 June 2021), p. 064030.*

4. Superconducting granular aluminum resonators resilient to magnetic fields up to 1 Tesla. K. Borisov, D. Rieger, P. Winkel, F. Henriques, F. Valenti, A. Ionita, M. Wessbecher, M. Spiecker, D. Gusenkova, I. M. Pop, and W. Wernsdorfer. In: *Applied Physics Letters 117.12 (2020), p. 120502.*

5. State preparation of a fluxonium qubit with feedback from a custom FPGA-based platform. R. Gebauer, N. Karcher, D. Gusenkova, M. Spiecker, L. Grünhaupt, I. Takmakov, P. Winkel, L. Planat, N. Roch, W. Wernsdorfer, A. V. Ustinov, M. Weber, M. Weides, I. M. Pop, and O. Sander. In: *AIP Conference Proceedings 2241.1 (2020), p. 020015.*

6. Phonon traps reduce the quasiparticle density in superconducting circuit. F. Henriques, F. Valenti, T. Charpentier, T. Charpentier, M. Lagoin, C. Gouriou, M. Martínez, L. Cardani, M. Vignati, L. Grünhaupt, D. Gusenkova, J. Ferrero, S. T. Skacel, W. Wernsdorfer, A. V. Ustinov, G. Catelani, O. Sander, and Ioan M. Pop. In: *Applied Physics Letters 115.21 (2019), p. 212601.*

7. Granular aluminium as a superconducting material for high-impedance quantum circuits. L. Grünhaupt and M. Spiecker, D. Gusenkova, N. Maleeva, S. T. Skacel, I. Takmakov, F. Valenti, P. Winkel, H. Rotzinger, W. Wernsdorfer, A. V. Ustinov & I. M. Pop. In: *Nature Materials 18.8 (2019), pp. 816–819.*

8. An argon ion beam milling process for native AlOx layers enabling coherent superconducting contacts. L. Grünhaupt and U. von Lüpke, D. Gusenkova, S. T. Skacel, N. Maleeva, S. Schlör, A. Bilmes, H. Rotzinger, A. V. Ustinov, M. Weides, and I. M. Pop. In: *Applied Physics Letters 111.7 (2017), p. 072601.*

Acknowledgements

First of all, I am grateful to Evgenii Glushkov for introducing me to the field of superconducting quantum circuits. Your enthusiasm and positive mindset are inspiring. I am thankful to Prof. Alexey Ustinov for the support during my Master studies and for organizing my internship in the group of Ioan Pop which was a first step towards my PhD work in KIT. Special thanks goes to my PhD supervisor Ioan Pop for his guidance and advice, and for giving an example of scientific intuition which made my PhD an exciting journey. I appreciate the discussions we had about science and life, and the words of encouragement which you always had for me.

I thank the BFQ group for a great company. First, I am thankful to Sebastian Skacel for teaching me the fabrication secrets. I thank Natasha Maleeva and Lukas Grünhaupt for warm support, Patrick Winkel for the pranks and jokes which brightened up my life. I thank Martin Spiecker for being an inspiring and talented person, and for all the scientific disputes which made me wonder if you can be wrong at least once. I thank Francesco Valenti for always cheering me up when times were tough. I thank Patrick Paluch for sharing late working evenings and for being a companion in the crazy parties. I thank Dennis Rieger and Simon Günzler for discussions and for an example of great tandem. I thank Ivan Takmakov for accompanying the Magpie fridge cooldowns. I also thank all people who took part in proofreading this dissertation.

I am grateful to all my collaborators, Richard Gebauer, group of Gerhard Kirchmair, Martin Rymarz, Dennis Willsch and Madita Willsch for exchange of knowledge.

I thank all the Fluxon group members, Alex, Jochen, Hannes, Nico, Tim, Yannick, and Sasha Lukashenko. I thank the Nanospin group members for an example of great working community, and their leader Prof. Wolfgang Wernsdorfer for all the practical tricks and attitude to work he taught me. My special thanks goes to Julian for being a great human and friend.

I thank Julia Zotova for a great friendship, and I thank my family and Leonid for supporting me and for giving me strength. I am lucky to have you by my side.